POLITECNICO DI MILANO

DIPARTIMENTO DI SCIENZE E TECNOLOGIE AEROSPAZIALI

DOCTORAL PROGRAMME IN AEROSPACE ENGINEERING

XXVIII CYCLE

Aeroservoelasticity of SMART Rotors

Doctoral Dissertation of:
Claudio BRILLANTE

Supervisor:
Prof. Paolo MANTEGAZZA

Tutor:
Prof. Giuseppe QUARANTA

The Chair of the Doctoral Program:
Prof. Luigi VIGEVANO

February 22, 2016

Contents

List of Figures

List of Tables

Acknowledgments

I wish to thank my supervisor Professor Mantegazza, an inspiring guide during all this study, and Professor Morandini for beeing by my side form the beginning of the work.

Ich möchte mich auch bei dem Deutschen Zentrum für Luft- und Raumfahrt für die Hilfsbereitschaft, die Gastfreundschaft und die wunderschöne Erfahrung bedanken. Ich danke meinem Freund und Kollegen Philip, der dieses Erlebnis unvergesslich gemacht hat.

Un ringraziamento speciale va anche alla mia Mamma e alla mia famiglia che, pur da lontano, mi sono sempre vicini e sostengono ogni mia scelta.

Grazie Carolina per credere sempre in me. Con la tua dolcezza, il tuo essere solare e la tua determinazione hai saputo trasformare anche le difficoltà di questo percorso in momenti piacevoli e continui a motivarmi ogni giorno.

Abstract

Helicopters experience a severe level of vibrations on the main rotor due to the asymmetrical airflow in forward flight. These vibratory loads are transmitted to the fuselage and degrade the flight comfort, while causing structural components wear. Therefore the objective of this research is the study and design of actively controlled systems that are able to suppress these loads, with the aim to set the basis for further investigations about the presented topics.

Due to the necessity of reproducing the complex behavior of the rotor with a sufficient level of accuracy in forward flight, before designing control systems, the first part of the thesis focuses on the development of a computationally efficient aeroservoelastic rotor simulation toolbox. The flexible multibody approach, together with a here developed semi analytical method for the sectional properties computation of a generic anisotropic beam including possible piezoelectric and piezomagnetic actuators, is exploited for the structural modeling and then coupled to three different aerodynamic models of increasing accuracy. Starting form the simple aerodynamics integrated in the multibody software, more sophisticated models, which are based on the hybrid approach, are developed by exploiting both the full potential analysis and the free wake geometry. The closed loop simulations are hence carried out within the Simulink environment. The first rotor analysis are aimed at validating the proposed code with experimental data and similar methods available in the literature.

The thesis focuses on actively twisted blades having distributed piezoelectric actuators along the blade span and the second part of this work compares three advanced active control algorithms in order to assess their advantages and limitations. At first, linearized model-based periodic controllers are designed on the multibody model and then their robustness is verified on the more accurate aerodynamic models. The second approach is a nonlinear adaptive recurrent neural network control and it does not require the knowledge of a numeric rotor model. After that, the classical adaptive higher harmonic control is enhanced to properly take into account actuator saturations. These controllers show satisfactory results and they are all computationally efficient, thus having real time capabilities.

Having analyzed different active control strategies, the third part of this thesis studies other actuation mechanisms to perform individual blade control. Using the higher harmonic control, the active twist solution is compared to the active trailing edge flaps approach, which has shown to be much more effective for vibrations reduction than the actively twist blades, at least for the considered trim configuration and with the current position of the piezoelectric actuators.

The last chapter shows an experimental activity performed at the German Aerospace Center. Individual blade control is here achieved through actuators in the non rotating frame by using the multiple swashplate system. Blade tracking control is then successfully performed in order to suppress vibratory loads in hover due to the blades dissimilarity.

Sommario

Gli elicotteri sono soggetti a grandi vibrazioni sul rotore principale a causa del flusso d'aria asimmetrico in volo avanzato. Questi carichi vibratori sono trasmessi alla fusoliera e degradano il comfort del volo deteriorando i componenti strutturali. Pertanto, lo scopo di questa ricerca è lo studio e la progettazione di sistemi di controllo attivo che sono in grado di sopprimere questi carichi, con l'obiettivo di gettare le basi per ulteriori approfondimenti sugli argomenti presentati.

A causa della necessità di riprodurre con un buon livello di fedeltà il complesso comportamento del rotore in volo in avanti, prima di progettare sistemi di controllo, la prima parte della tesi si concentra sullo sviluppo di uno strumento per la simulazione aeroservoelastica di rotori, che sia computazionalmente efficiente. L'approccio multicorpo con l' aggiunta di componenti flessibili, insieme ad un metodo semi analitico, qui sviluppato, per il calcolo delle proprietà sezionali di una generica trave anisotropa con possibili attuatori piezoelettrici e piezomagnetici, viene sfruttato per la modellazione strutturale e poi accoppiato a tre diversi modelli aerodinamici sempre più accurati. A partire dalla semplice aerodinamica integrata nel codice multicorpo, modelli più sofisticati, che si basano su un approccio ibrido, sono stati sviluppati sfruttando sia il potenziale completo sia il calcolo della scia libera. Le simulazioni ad anello chiuso sono quindi svolte all'interno dell'ambiente Simulink. Le prime analisi del rotore sono finalizzate a convalidare il codice proposto con i dati sperimentali e con metodi simili disponibili in letteratura.

La tesi si concentra sullo svergolamento attivo delle pale attraverso attuatori piezoelettrici distribuiti lungo l' apertura e la seconda parte di questo lavoro mette a confronto tre algoritmi di controllo attivo avanzati al fine di valutare i loro vantaggi e limiti. In primo luogo vengono progettati controllori linearizzati periodici, che richiedono la conoscenza di un modello numerico del sistema da controllare, sul modello multicorpo e la loro robustezza viene convalidata usando un modello aerodinamico più accurato. Il secondo approccio non richiede la conoscenza del modello del rotore ed è un controllo non lineare adattativo basato sulle reti neurali ricorrenti. Infine, il controllo classico ad armoniche successive, nella sua versione adattiva, è stato migliorato per tenere adeguatamente in conto di eventuali saturazioni degli attuatori. Questi controllori mostrano risultati soddisfacenti e sono tutti computazionalmente efficienti, avendo così capacità di operare in tempo reale.

Dopo aver analizzato diverse strategie di controllo attivo, la terza parte di questa tesi studia altri meccanismi di attuazione per effettuare un controllo individuale delle pale. Utilizzando il controllo ad armoniche successive, la soluzione dello svergolamento attivo delle pale viene confrontata con la pala avente una superficie aerodinamica mobile al bordo di uscita, la quale dimostra di essere molto più efficace nel ridurre le vibrazioni dello svergolamento attivo, almeno per la condizione di volo considerata e con la presente posizione degli attuatori piezoelettrici.

L'ultimo capitolo mostra un'attività sperimentale svolta presso il German Aerospace Center. Il

comando individuale delle pale viene qui realizzato tramite attuatori nel sistema non rotante utilizzando il doppio piatto oscillante. Viene quindi eseguito un controllo individuale sul passo collettivo delle pale al fine di sopprimere i carichi vibratori in hover, causati dal fatto che nella realtà le pale non sono perfettamente identiche.

Introduction

Helicopters are flying machines that have an indispensable role in aviation. The advantage of using rotating wings to provide lift and propulsion give them the possibility to fly at zero or low air-speeds and to move in almost any direction, because they are able to hover and to take off and land vertically, thus operating in situations where conventional fixed-wing aircraft are not suitable. These unique capabilities makes the helicopter the best candidate to perform a huge number of operations both civil and military, such as: rescue missions, police surveillance, oil rig servicing, transport of humans and goods etc., and its employment has grown in recent years, thanks also to the technological progress. Therefore the increasing demand from the industries and hence the huge number of people involved during the operating life of a rotary-wing aircraft leads to the need of producing more and more efficient and safe helicopter.

The conventional helicopter architecture is composed by a main rotor mounted on the fuselage, which has the function of providing the required lift and control forces, and a tail rotor, which generates lateral forces to counteract the rotation of the fuselage that naturally opposes the rotation of the main rotor. Rotating blades allow a large variety of operating conditions, but the fact of having rotating parts at high angular speed increases design difficulties and makes helicopters sophisticated machines, working in a complicated aerodynamic environment as it is well explained in [1]. While in hover, due to the absence of the advance velocity, each blade experiences the same distribution of incident airflow, which is linear and proportional to the blade radius and the blade rotation, in forward flight the aircraft speed is added to that of the rotor rotation and the aerodynamic loads of the blade become a function of the azimuth angle, leading to an asymmetrical loading of the rotor disk. For the advancing blade the relative velocity of the wind is higher, because the free stream velocity is summed to the one caused by the rotation and the blade tips experience more serious compressibility effects up to the transonic regime where shock waves may happen. On the other side, the advance velocity is subtracted to the retreating blade one and reverse flow conditions occur near the blade root for elevated forward speed, letting the blade sections operate in stall and thus causing high levels of drag. The wake released by a helicopter rotor is much more intricate than that released by a fixed wing. Each blade releases a wake and because of the rotation its geometry is quite complex and dominated by strong tip vortices that interact with the blades giving birth to the so called blade vortex interaction (BVI) phenomenon, very important for the blade loading. Moreover the rotor wake impacts with the fuselage and other non-rotating parts and it is an additional source of excitation for these components.

The connection of the blades to the rotor hub has to expect three hinges at the blade root to ensure the correct load handling and the transmission of control forces to govern the flight dynamics of the helicopter. The pitch hinge is necessary to change the blade pitch and then to modify the blade angle of attack to control the desired lift over the rotor revolution. Two other hinges, the flap and the lead-lag

one, are required to take care of velocity asymmetry in forward flight by changing the local angle of attack through the flap motion and to alleviate the high moment at the blade root due to the Coriolis forces, respectively. This solution can be achieved either through mechanical hinges or through the proper design of a flexbeam at the blade root with predefined flexibilities at concentrated points to allow the blade root deflections; the rotor with flexible hinges are called hingeless, when only the pitch hinge is mechanical or bearingless when all the hinges are designed within the flexbeam. The typical design of rotor blades produces aerodynamic bodies with very large radius with respect to the chord, ensuring hover efficiency, hence they are slender bodies and very flexible. Due to their high flexibility, the blades could not be used to sustain high loads in static applications, but the rotational speed of the rotor has a stiffening effect on the blades through centrifugal loads, providing to the blades the required stiffness to sustain the whole helicopter. As it can be understood from the complex motion of the blades, inertial loads play an important role in the blade dynamics and if their effects are not considered appropriately during the design phase the coupling of the inertial and Coriolis forces with the dynamic motion of the blades can destabilize the rotor system. Moreover, in contrast to the fixed-wing vehicles, the blades are usually built using composite layers for the external surface, foams, honeycomb structures and other to fill the inner cavities, leading to an anisotropic section with strong elastic couplings.

The combination of the unsteady aerodynamic loads and the asymmetrical disk loading in forward flight with the blade motion and the large structural deformations leads to great oscillatory loads that are transmitted to the fuselage causing high levels of vibrations and noise that limit the helicopter applicability. The main sources of rotorcraft vibrations are the main and the tail rotor, the gearbox, the engine and the fuselage. However more that 90% *of the vibratory loads are generated by the main rotor, which is therefore the subject to be studied to reduce these effects. Due to the alternate loading of the rotor blades over the rotor revolution in forward flight, the aerodynamic loads excite multiple frequencies of the rotor angular speed* Ω*. As discussed before, the returning wake and the impact of the released blade vortices on the other blades contributes to increase the periodic excitation. If considering the blades identical, it can be demonstrated through a Fourier analysis and the summation of the loads generated by all rotating blades that not all frequencies are transmitted to the fuselage, i.e. to the non rotating system, but they depend on the number of blades N mounted on the rotor hub [2]. In particular for the vertical force and the torque of the hub only the steady and the multiples of the* N/rev *harmonics of the blade root force and moment are not filtered by the hub. On the other hand, the multiples of the* N/rev *harmonics of the in plane forces and moments of the hub, with respect to the rotor disk, are generated by the multiples of the* $(N-1)/rev$ *and the* $(N+1)/rev$ *of the blade loads and moments.*

The low frequency content of the rotor helicopter excitations are referred as vibrations, while the higher one is responsible for the noise. While helicopter noise has a strong impact in what concern the inner and outer environment of the fuselage and is mainly related to the passage of the vehicle near inhabited areas, structural vibrations cause passenger and crew discomfort and fatigue problems that affect the reliability and the operating life of the whole machine. They also reduce weapon effectiveness and makes it difficult to read the navigation instruments. It is interesting to emphasize that the overall vibrations of an helicopter can be up to ten times higher than that of a conventional fixed-wing aircraft [3]. Moreover, the reduction of vibrations can significantly improve the reliability and strongly reduce maintenance costs [4]. That explains why a huge interest in alleviating these problems has involved aeronautical researchers.

Having explained the main features and problems of helicopter rotors, one can immediately understand that the complex blade motion, the nonlinear effects, together with the unsteady and periodic aerodynamic loads represent a challenge to the vibration analysis and reduction, since it requires a demanding multidisciplinary analysis of the aerodynamics, structural dynamics and possible active control techniques. Therefore, in order to properly assess the vibration suppression problem and come up with a feasible and safe solution, coupled aeroservoelastic designs and simulations are needed based on reduced order mathematical models that are accurate enough to reproduce the main characteristics of the rotor to ensure a robust vibration alleviation method, without losing computational efficiency, which is a fundamental requisite since the design is an iterative process, which requires a huge number of simulations.

Whenever an active control solution is chosen to alleviate the vibratory loads, the traditional approaches have often used oversimplified mathematical models to approximate the aerodynamics and the structure dynamics of the blades, to easily handle the controller design through coupled closed loop simulations. Without talking about the more recent computational fluid dynamics (CFD), which is too time consuming and it is not suitable for the preliminary design phase, since very time consuming simulations are required to simulate a few rotor revolutions with a good level of accuracy, well established models, adequate to approximate the rotor blades aerodynamics can be found in the literature. The basic approach, which exploits the blade element method (BEM) by dividing the blade into several strips, is derived from the classical unsteady aerodynamic airfoil theory through the Theodorsen function using either the indicial function representation [1, 5] or finite states approximations [6, 7, 8]. A more sophisticated blade aerodynamics can be derived by a rational function approximation of the two-dimensional unsteady CFD analysis of the airfoil motion [9, 10]. Moreover in most cases the wake geometry is usually not reproduced and the induced velocity is modeled through simplified mathematical models [1, 2, 11, 12, 13]. For controller design purposes it is preferred to perform the aeroservoelastic coupled closed loop simulation after reducing these aerodynamic models to linear and quasi-steady ones, in which only the periodic velocity terms are retained [14, 15, 16, 13].

Similar considerations arise from the literature for the structural modeling of the blades. Due to their slenderness they can be approximated as equivalent beams, which are preferred over the computationally demanding three-dimensional finite elements method (FEM). The most common method used to model the elastic torsion and the bending structural deformations of the blade is the Euler-Bernoulli beam. The derivation of the dynamic equation of motion of the blade is usually performed after the one dimensional finite element discretization of the blade through the Hamilton's principle [16]. Another common method to discretize the beam problem is the computation of the mode shapes of the rotating beam [17, 13].

Although the classical modeling approach presented before has been widely used in the literature to perform helicopter vibration analysis and to study active control systems in the preliminary design phase, the comparison with experimental data shows that such simplified models and quasi-steady aerodynamic assumptions fail to predict the blade loads, especially when active actuators in the rotating systems, such as actively controlled flaps, are employed to modify the aerodynamic forces [18, 19].

The general description of a helicopter's main problems, such as vibrations and noise, presented in this section, and a brief overview of the classical simulation methods that are used for vibration analysis and control purposes, summarizes the main issues that the researchers in this field have to face and overcome. In order to increase the reliability of the active control strategies, which seem

to be the most effective way to reduce rotorcraft vibrations, and to increase the chance that active controls for vibrations alleviation will be implemented in true flying helicopters, the research has to investigate for possible more accurate design and simulation methods, computational efficient and without oversimplifying the problem, as well as the applicability and adaptability of the several control theories to the smart structures that are being implemented to design technologically advanced rotor blades [20].

Methods for Vibration Reduction

The problem of vibrations reduction of helicopters has been analyzed with different methods. The earliest approach to alleviate vibratory loads involved the usage of passive absorbers. They are usually composed by a single degree of freedom system with a mass and a spring, properly tuned to notch the desired harmonics [21, 22]. A review of passive vibration reduction methods can be found in [23]. The main drawbacks of such devices are that they can be designed and tuned mostly for a specific condition and add an undesirable weight. In [24] the blade pitch link is replaced by a spring/damper element to develop a passive vibration reduction device. Another passive approach involves optimization techniques to design advanced blade geometries and to modify their elastic and mass properties, so to minimize the aeroelastic response and hence reducing the oscillatory loads [25, 26]. Thanks to the use of composite materials, the shape of the blades can be easily altered and there is a large set of available design variables, such as the ply angle and thickness or mass balance position, which can be exploited within an optimization study.

While passive approaches and the structural optimization, are very useful for developing an aeroelastically efficient helicopter, active control techniques act directly on the source of vibrations by appropriately modifying the aerodynamic loads and can be the most effective way to alleviate vibrations. The first actuator that has been exploited to directly actuate the blades is the already available swashplate. This solution is well known in the literature as the higher harmonic control (HHC) method [27, 28]. By moving the swashplate at harmonics higher than the rotor frequency, it is possible to change the blade pitch to modify the aerodynamic loads and achieve the desired objective. Even if this approach does not require modifications of the blades and of the rotor hub, it requires a significant actuation power and it is not able to control the blades independently when the rotor has more than three blades.

For these reasons the study of active controls has evolved into the individual blade control (IBC) approach, in which each blade can be controlled independently and a set of different and more efficient actuators are exploited and investigated. The possibility of using an on-blade actuator to reduce vibration and noise was also supported by the advent of smart materials, which are light weight and require a smaller actuation power. A review of active control methods can be found in [29, 30, 31]. In this section the most used approaches for vibratory loads reduction using IBC actuators are briefly described.

- ***Active pitch links***
  A first individual blade control strategy does not require any modification of the blades and the IBC actuation capabilities are achieved by acting on the pitch links. The main idea is to design an active pitch link able to modify its stiffness and damping properties during the rotor revolution in order to mitigate the loads that are transmitted to the hub [32]. For example,

inside the pitch link, two springs have the ends attached to the opposite walls and can slide one with respect to another. An external input is applied through a piezoelectric stack that provides a friction forces that induces the contact between the two springs, thus varying adaptively the overall stiffness and damping properties in real time, leading to vibrations and noise reduction potentials.

- ***Actively twisted blades***
  Thanks to the smart structures development and to the improvement of piezoelectric actuators with Macro-Fiber Composite (MFC) piezoelectric patches, which are able to maximize the actuation capability by exploiting the primary direction of the material polarization, it is possible to control the blade twist in an efficient manner with a moderate actuation power. To produce this actuation mechanism, piezoelectric actuators are then distributed along the blade span and embedded within the composite layers of the outer surface of the blade so to generate a twisting torque. Since these actuators are on the rotating system, the control voltage computed to change the aerodynamic loads is provided by means of high voltage slip rings. This solution has been widely investigated in recent years for vibration control purposes [33, 34], and experimental tests carried out at NASA [35] and DLR [36, 37] proved the feasibility of such a control method. An example of the capabilities of the actively twisted blades to alleviate rotor vibrations is presented in [38]. By using an appropriate control of the twist these smart blades can be also used to reduce the noise generated by the blade vortex interaction, as shown in [39]. Despite the results shown in the literature seem to be very promising for the future of the rotary-wing aircraft, the high level of technology required to design the blades represents the limit of such a solution. In fact apart from production costs that are much higher than that of a conventional blade, a deeper study on composite materials as well as on fatigue problems mitigation has to be done before implementing this approach in conventional helicopters.

- ***Active trailing edge flaps***
  Being inspired by what is already implemented on fixed-wing aircraft, active trailing edge flaps have seen a growing interest for rotorcraft applications as well. They are used to actively modify the blade aerodynamic loads and most of the studies focus on the ability to reduce helicopter vibrations [40, 41, 42, 43]. The aerodynamic loads are modified by the flap motion, which can affect the blade bending during the rotation. Since the harmonic aerodynamic loads are multiples of the rotating rotor frequency, the active flaps have to be actuated at similar frequencies, therefore a piezoelectric actuator, which has a high bandwidth, is usually preferred over an electric motor. Apart form the size of the trailing edge flaps, another important design parameter that influences the performance is the position of the flaps along the blade span. This solution is very effective in reducing vibratory loads, even with small flap deflections. When a greater control authority is demanded, as in the recent works aimed at removing the swashplate and to perform primary rotor control by using trailing edge flaps, the deflection is limited by high friction forces that arise because of the high angular speed and of centrifugal forces [44, 45, 46]. The application of multiple flaps on the blades has been investigated and it is shown that they can achieve a better vibration reduction than a single one [43, 47]. The study of the active trailing edge flap capabilities is not only limited to vibration alleviation applications, but they can also be employed to enhance rotor power performance [48] and to reduce the noise by acting on the blade vortex interaction [49].

- ***Gurney flaps***
  An actuation mechanism similar to the trailing edge flap is the gurney flap. It is a small trailing edge tab positioned at 90 degrees with respect to the chord of the airfoil. This device induces a low pressure zone on the suction side and helps the boundary layer flow stay attached all the way to the trailing edge of the airfoil. As shown in several aerodynamic studies, this effect is very interesting because it increases the lift over a large range of angles of attack without significantly increasing the drag [50, 51, 52, 53, 54]. Therefore this solution has been investigated for rotorcraft performance enhancement, especially in hover and in light stall conditions to increase the flight envelope of the helicopter. Due to their capabilities to modify both the lift of the blade and its mechanical behavior, they have been also investigated to reduce vibrations and noise [55, 56, 57]. By increasing its length, the gurney flap shows an increase in the drag and pitching moments that outweigh the benefits, therefore its length is usually limited to the 2% of the airfoil chord.

- ***Morphing blades***
  Another method, which is gaining a significant attention in recent years is the active modification of the blade aerodynamic loads through a morphing technology. The basic idea behind this concept is to mimic flying animals that are able to adapt the wings by modifying their shape to the situations they encounter during the flight without using moving parts such as flaps. For rotorcraft applications several methods have been studied to actively modify the shape of the airfoil of a rotor blade to increase performance while maintaining stability and control. The first approach is the design of an airfoil with a variable droop leading edge [58, 59]. By actively inducing the downward motion of the airfoil nose, it is possible to increase the lift. As a consequence of this nose motion, the airfoil experiences a reduction of the maximum lift, the drag and the pitching moment. Although this solution could be employed to reduce helicopter vibrations, because it suppresses the dynamic stall in the retreating blade, the decrease in the maximum lift, due to the leading edge deployment, leads to a reduction of the helicopter maximum speed. The second attempt to modify the airfoil shape is the variable camber technique. The variation of the airfoil camber has the same effect as a gurney flap increasing the lift, while maintaining the same chord length. Therefore this approach could be used to reduce rotor vibrations and to expand the flight envelope [60, 61, 62]. To realize this active camber actuation, a compliant mechanism composed by piezoelectric bars with variable length. Recent developments show the application of chiral structures to this end [63]. To increase the lift of an airfoil another parameter that can be actively modified is the length of the chord. Therefore a trailing edge extension mechanism is shown in [64]. By doing so, the lift augmentation is obtained with a minimal increase of the lift/drag ratio. However the drag that arises due to the trailing edge extension constitutes a problem for the blade efficiency. Even if these approaches are very promising to enhance rotorcraft performance, the design, the manufacture and maintenance of the blades become very complicated.

A completely different approach to alleviate the loads transmitted to the helicopter body is represented by the active control in fuselage. In practice, this method does not act at the blade level and does not require actuators in the rotating system. The basic principle is the connection of a number of hydraulic actuators among specific points in the fuselage to suppress the vibration signals [65, 66]. This approach is very promising to reduce the fuselage vibration level, but it requires a very accurate

and detailed model of the rotor/fuselage dynamics in order to determine the optimum placement of the actuators, which is in most cases not easy to obtain. Another disadvantage of directly controlling the vibrations in the fuselage is the fact that the aerodynamic loads, which are the sources of rotorcraft excitations are non modified, thus it is non able to reduce noise and increase rotor performance.

Thesis Objectives

This thesis focuses on the study of the vibrations produced by a helicopter rotor and the aim of this project is the research and development of control systems in conjunction with SMART rotor technologies able to suppress vibratory loads in forward flight using individual blade control.

The basic requirement for designing a robust controller is to have available an adequate mathematical model describing the essential dynamics of the system to be controlled. Since the modeling of rotorcraft vibrations is a strongly coupled aeroelastic problem, in which the nonlinear and complex structural dynamics of the blades interacts with unsteady aerodynamic loads that depend on the complex rotor wake structure, linearized and quasi-static mathematical models fail to properly represent the rotor system behavior. Although advances in computer technology has made it possible more and more accurate high fidelity CFD aeroelastic simulations, capable of reproducing blade loads close to experimental data, the computational time needed to perform such analysis is still overwhelming for the design of a controller, which is usually conceived in the preliminary phase of a project and requires several tuning simulations. As a matter of fact, nowadays the vibration suppression studies are performed using oversimplified models of the helicopter, which may lead to unsatisfactory performance if applied on real rotary-wing aircraft.

Therefore the first objective of the present work is to investigate the possibility of developing an aeroservoelastic rotor simulation toolbox with a good level of accuracy that can be used profitably for both controller design and validation before the experimental tests. A high level of fidelity can be achieved for the structural modeling with low computational effort through multibody softwares, taking into account both nonlinear structural couplings and generic complex motions, as done in this work. Without using full three-dimensional finite element representations, the flexibility of the blades is correctly taken into account through geometrically nonlinear beam models and precise properties computations. The first contribution of this thesis is the development of a new semianalytical algorithm to compute the section properties of a generic beam section with embedded piezoelectric and piezomagnetic actuators. The equation of motion are then solved within the multibody software, without reducing or linearizing the resulting rotor dynamic system. The best way to alleviate the computational cost of the aerodynamic simulations, as outlined in the literature, is to exploit the hybrid methods, in which the blade near field aerodynamics is analyzed through a different method, often more accurate, than the one used to model the far field released rotor wake. Because of the need to keep the simulation time within reasonable levels and of the different degree of approximations available, two methods are exploited and compared, with the aim of understanding which effect is predominant and requires a more accurate modeling. In the first proposed method a full potential CFD solver is used to simulate the blade unsteady aerodynamics coupling it to a generalized wake mathematical model; In the second method the computational time is invested into the rotor wake modeling through vortex filaments, while the blade aerodynamics is approximated with the well known blade element theory adding unsteady corrections. It is important to emphasize that such methods are not meant to replace full CFD aeroelastic models, which are very useful for high fidelity loads prediction and validation

studies for the final design stage, but the whole work is aimed at enhancing the controller design by providing more accurate and computationally fast mathematical models.

The second objective of this thesis is to compare other control theories and to overcome the classical higher harmonic control algorithm. Although this classical method has proved to be quite effective for vibration reduction and simple to be designed, it still relies on a quasi-static rotor model. Therefore more complex control techniques are investigated to understand their limits and applicability to the vibration reduction problem. Starting from the linear periodic system control theory, which permits to take into account the periodicity of the rotor blades in forward flight, the attention is moved to a complete black-box nonlinear adaptive control through neural networks that does not introduce further modeling approximations. The main contribution of this work is not in the development of new controller algorithms. Since such advanced control systems are usually tested on simple academic cases, this work implements these controllers on complex aeroelastic systems, such as the helicopter rotor, and encourages the development of the literature in this research field. This is very useful to assess the possibility of a future practical application. One of the main problem that one can encounter during experimental tests is the actuator saturation due to undesired control activity. This issue is handled in this thesis as well and the classical higher harmonic control algorithm is enhanced by imposing actuator constraints.

The whole study considers an active twist rotor with piezoelectric actuators distributed along the blade span. The last objective of the thesis is to compare the chosen actuation mechanism with other SMART rotor approaches and therefore the rotor vibrations are reduced through active trailing edge flaps to study the most effective solution. To do so, the aeroservoelastic code is extended to include the modeling of movable aerodynamic surfaces. The last part of the thesis is related to an experimental activity ccaried out at the German Aerospace Center (DLR), where the multiple swashplate system (META) is beeing developed. This method permits to individually control the blades for rotor performance enhancement and vibration reduction without actuators on the rotating frame. In this activities the enhanced higher harmonic controller algorithm with the actuator constraints handling is implemented within the real time environment and it has been tested on an experimental rotor model. This application is of significant value because it widens the possibility that actively controlled rotors will be employed in the near future to ensure a more comfortable and safer flight.

Thesis Outline

Due to the complexity of rotorcraft vibration problem and to the multidisciplinary analysis required, the thesis deals with a number of topics ranging from the modeling of the helicopter rotor to the different controller algorithms to reduce vibratory loads. Therefore it is useful to divide the work into three parts. The content of these parts is briefly overviewed hereinafter.

- ***Part I: Helicopter Rotor Modeling***
  The first part of the work covers the modeling approach of the helicopter rotor and proposes a new aeroservoelastic rotor simulation code that can be used for controller design and validation purposes. Chapter 1 *explains the modeling approach chosen to approximate the structure dynamics. First a semianalytical method to compute the stiffness properties of a generic anisotropic beam including magneto-electro-elastic couplings to model both piezoelectric and piezomagnetic actuators is developed and validated with similar methods available in the liter-*

ature; then a multibody rotor model of an active twist rotor is built starting from an available numerical model of the Bo105 rotor. In Chapter 2 *the hybrid aerodynamic simulation methodology is exploited to improve the approximation level of accuracy for helicopter rotor simulations. Two techniques are shown. In the first section a full potential CFD solver is used to simulate the aerodynamic of the blades, while the induced velocity generated by the rotor is taken into account through the Peters-He generalized wake model. The proposed solution is validated at first with CFD Euler simulations and then with the experimental data of the Hart II rotor model. The second section shows a different aerodynamic simulation code, in which the blade aerodynamics is approximated through the blade element method corrected to take into account unsteady effects. A free wake code considering only trailing edge tip vortices is developed and coupled to the blade aerodynamic model, thus being able to simulate the blade vortex interaction. This code is validated using experimental data of the Hart II rotor and similar methods available in the literature.*

- ***Part II: Control Systems Design***
  The second part of the thesis presents the control systems that have been exploited to minimize the rotorcraft vibrations. Several techniques are implemented on the same rotor model and trim configurations in order to compare the different solutions. In Chapter 3 *the periodic behavior of the rotor in forward flight is taken into account by the controller and both the full information H_2 control and the static output feedback one for periodic systems have been considered. The controller are designed on the multibody rotor model and then validated to the more complex hybrid aerodynamic solvers.* Chapter 4 *presents the black-box approach to control the rotorcraft vibrations by exploiting the recurrent neural networks. The parameters of the nonlinear adaptive neural network controller are tuned within the multibody simulations and then validated on the free wake aerodynamic code. The higher harmonic control is revised in* Chapter 5. *After presenting the classical and adaptive algorithm, the method is modified to introduce actuator constraints through a quadratic optimization. The HHC controller capabilities are first assessed on the hybrid CFD aeroelastic simulation code and then the potential of having properly taken into account actuator constraints is shown through simulations with the free wake code.*

- ***Part III: Comparison with Different Control Strategies***
  In the third part of the study other individual blade control methods are considered and compared to the active twist rotor approach. In Chapter 6 *the aeroelastic free wake code is improved in order to model trailing edge flaps and the vibrations are reduced using the enhanced HHC algorithm imposing a limit for the flap deflection. The results are then compared to the ones obtained with the actively twisted blades. The IBC approach described in* Chapter 7 *differs from the previous ones, because the blades are controlled using a double swashplate, hence without actuators in he rotating frame. The HHC algorithm capable of handling actuator constraints is implementer within the real time environment and then linked to an experimental rotor model of the Hart II available at the German Aerospace Center. Results regarding the blades tracking control in hover are shown.*

The last chapter points out the conclusions and the main findings of this work. A brief summary of the study is provided and the original contribution in the vibration suppression research field is analyzed. The last section proposes some ideas for future works to extend and improve this work.

Part I

Helicopter Rotor Modeling

Chapter 1

Structural Approximation

The structural model of an helicopter rotor is particularly critical because of its complex motion at high angular velocities that generate strong inertial couplings and large structural displacement that are intrinsically nonlinear. Even if a linearization around a trim condition and the use of the modal reduction for the flexible blades can reproduce the response of a rotor subsystem, they often result as rough approximations adapt only for fast simulations. One of the main goals of this work is to provide a reliable and computationally efficient aeroelastic model of the helicopter rotor with the purpose of designing controllers robust enough to reduce the risks and the level of uncertainty during real experiments. Therefore, as correct as possible modeling of the structure is mandatory and, to such an end, a deformable multibody model is probably the best choice. While a rigid body representation of the command chain, i.e. swashplate and pitch links is usually a good approximation, well characterized flexible blades are of utmost importance, especially for vibratory loads predictions and transient analysis.

In the literature and in most of the rotor simulation codes, due to their slender shape the blades are represented with equivalent beams, provided the correct sectional stiffness and mass properties are given. The blade section of a helicopter blade is usually composed by different materials, composite layers and internal foam, that make it very complex and anisotropic. Therefore a classical Euler-Bernoulli beam formulation is not able to consider all the structural couplings and the correct estimation of the stiffness matrix of the equivalent beam section is a significant issue and likely the most important aspect when dealing with the structure of a rotor.

The first section of this chapter is aimed at providing a semianalytical tool to compute a full coupled $(6x6)$ *stiffness matrix for a generic anisotropic beam section with the possibility to include piezoelectric layers as actuators [67]. Piezoelectric devices are used for many different applications, either as actuators or sensors. Their relatively high operational bandwidth makes them suitable for applications where a reduction of structural vibrations and noise radiation is sought [68, 69]. Many applications involve piezoelectric devices embedded into slender beams. As an example, piezoelectric patches can be used to actively twist helicopter rotor blades. This solution should allow a reduction of loads and vibrations in the fuselage, as shown in [70] and [71]. Thanks to such methods it is possible to have an accurate estimate of the main structural properties even in a preliminary design phase. Starting form a review of the most relevant methods for the evaluation of the sectional properties available in the literature, the methon here developed is presented and validated through three examples. This method is then extended to model piezomagnetic effects as well. The last section describes*

the multibody model of the active twist rotor used throughout the thesis.

1.1 Characterization of Piezoelectric Beam Stiffness Matrix

Piezoelectrically actuated beams has been studied by researchers for several years and a still valid review, albeit not very recent, about piezoelectric structures modeling can be found in [72]. Three dimensional finite element models are often used to predict the response of beams with embedded piezelectric patches, e.g. in [73]. However, many works strives to avoid the complexity and cost of a full three dimensional model through simpler yet reliable models. The simplest beam model is based on the Euler-Bernoulli approximation, as in [74], and [75]. These works accounts only for the axial beam strain, and not for the change of dimension of the beam section. This allows to obtain an analytical expression for the cross-section properties. This kind of models can be improved by accounting for shear deformations, as found in [76] and [77]. The former proposes a Timoshenko model for the core section and neglects the shear deformation for the external layers; the latter accounts for a parabolic distribution of the shear strain. It must be noted, though, that many of these specialized formulations must resort to constitutive equations specialized for an axial stress state. This fact, by itself, somewhat limits their applicability to the case of complex sections made of laminated composite materials. The use of mixed variational principles have been advocated by [78] to overcome the intrinsic limitations of the Euler-Bernoulli kinematic approximation.

In recent years countless papers on the beam sections structural properties characterization have been published; the interested reader can find a recent, partial overview in [79]. A general procedure for computing the stiffness matrix of a beam of arbitrarily complex geometry and made of composite materials was proposed in [80]. The procedure is based on a semi-analytical expansion of the unknown displacement field, with the stiffness matrix computed from the set of the so-called de Saint-Venant's solutions. To do so, the cross-section is discretized into finite elements, and the null eigenvalue solutions of a system of homogeneous second order differential equations along the beam axis sought. Since then, many similar works have been published on the subject, some of them specializing the theory to the case of thin-walled beams. Among them, it is worth mentioning the works published by Hodges and his co-workers, who approach the problem by aiming at an asymptotically correct solution. Their work is summarized in [81]. Following [80] and [81] extensions to the case of integrated piezoelectric devices were proposed in [82], [83] and [84].

A slightly different approach for the beam section characterization was proposed by [85]. Starting from Giavotto et al., [85] departs from it by resorting to the Hamiltonian structure of the solid beam differential equations, and do not add any (redundant) section rigid motion field to the section finite element displacement. This approach is strongly linked to Mielke's works on the de Saint-Venant's solutions [86]. A similar procedure, based on the works by Zong and co-workers, [87, 88], was proposed by [89].

This work extends [85] to electro-elastic beams. The related problem is first reformulated by accounting for both the structural and the electric virtual work. It is then shown that, when piezoelectric effects have to be accounted for, the governing second order system of equations is no more homogeneous. Rather, it has the charge per unit span imposed on the electrodes as a forcing term. The generalized beam stiffness can thus be computed by accounting for both the homogeneous and the particular solutions of the system. Along a similar line it is worth citing the work of [90]. They adopt the same formalism as [85], and recognize that piezoelectric materials can be accounted for

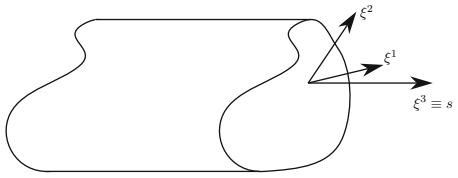

Figure 1.1: Straight beam geometry.

by considering not only the general solutions of the system but also the particular ones. They look for the analytical solution of a clamped beam, obtained by accounting for both of the null eigenvalue solutions and of the decaying ones and neither carry out a finite element discretization of the beam section nor attempt to compute the generalized stiffness matrix of the beam.

The here proposed approach should provide, with the same mesh and finite element family, the same results that can be obtained by following [82], [83] or [84]. The main difference between the proposed approach and the above mentioned works is conceptual. As explained above, all these works define the three dimensional displacement field by superposing a warping field onto the section motion. With the proposed approach, instead, the unknown displacement filed is defined without any redundancy. It is thus not necessary to further impose the indefinite equilibrium equations of the beam solving the three dimensional beam problem for a set of self-balanced internal forces, as in [82]. As a consequence, it is no more required to assume that the average section motion of the three dimensional model coincides with that of the mono-dimensional beam model. Moreover, departing from [82], the electrodes equipotentiality constraint is naturally accounted for, without the need of modifying the equation set any more. Furthermore, each independent electrode requires now the solution of a single additional system of linear equations, while two were required in [82]. Differently from [83] and [84], no asymptotic expansion is carried out. Thus, the result of the proposed procedure naturally leads to a beam stiffness matrix that does account for the shear deformation. In other words, it gives the actual stiffness matrix, computed from the so-called de Saint-Venant's solutions, of a given section, regardless of the beam length. Together with the stiffness matrix of the beam section, the algorithm provides also input-output electric equations for the piezoelectric components.

1.1.1 Kinematical Model and Constitutive Laws

Consider a geometrical model of a beam with the conventions of Fig. 1.1. Let $x(\xi^1,\xi^2,\xi^3)$ *be the position of a point in the reference configuration, where* ξ^3 *represents the coordinate along the straight axis of the beam and* ξ^1 *and* ξ^2 *are two local coordinates on the beam section. Assume the local coordinate* ξ^3 *to be perpendicular to the plane defined by* ξ^1 *and* ξ^2 *and, without loss of generality, coincident with the curvilinear abscissa s. The covariant base vector* $g_3 = \partial x/\partial\xi^3$ *is thus equal to the versor n, normal to the* ξ^1,ξ^2 *plane; the covariant base vector coincides with and to the contravariant one,* $g_3 = g^3 = n$. *Let* $x'(\xi^1,\xi^2,\xi^3)$ *be the position of a point in the deformed configuration, so that* $u = x' - x$ *is the displacement of the point. The deformation gradient F is given by*

$$F = x'_{/\otimes} = x'_{/\otimes S} + x'_{,3} \otimes g^3 \tag{1.1}$$

where g^i *are the three contravariant base vectors relative to the coordinates on the beam,* $x'_{/\otimes}$ *stands for the gradient of vector* x', $x'_{/\otimes} = x'_{,i} \otimes g^i$ *and* $x'_{/\otimes S} = x'_{,1} \otimes g^1 + x'_{,2} \otimes g^2$. *The somewhat awkward*

notation $x'_{/\otimes S}$ is introduced to decompose the deformation gradient F into a component along the direction of the beam axis and a term on the section plane. We are interested in the analysis of straight beams, with constant contravariant base vectors g^i along the span. The virtual variation of the deformation gradient is given by

$$\delta F = \delta x'_{/\otimes S} + \delta x'_{,3} \otimes g^3 \tag{1.2}$$

Assuming infinitesimal deformations and displacements, the strain tensor can be computed as

$$\varepsilon = \tfrac{1}{2}\left(F + F^T\right) - I \tag{1.3}$$

Linear constitutive laws are considered for both the structural and the piezoelectric regions. The relation between the Cauchy stress tensor S and the small strain tensor ε is given by

$$S = \mathbb{E} : \varepsilon. \tag{1.4}$$

The piezoelectric constitutive law is

$$\left\{ \begin{array}{c} S \\ D \end{array} \right\} = \left[\begin{array}{cc} \mathbb{E} & -\mathscr{E}^{T231} \\ \mathscr{E} & \varepsilon \end{array} \right] \left\{ \begin{array}{c} :\varepsilon \\ \cdot E \end{array} \right\}, \tag{1.5}$$

where $\mathscr{E}$ and ε are the piezoelectric and the dielectric tensors, D is the dielectric displacement, the electric field E is equal to minus the gradient of the electric potential V,

$$E = -V_{/\otimes} = -V_{/\otimes S} - V_{,3} g^3, \tag{1.6}$$

and the operator $(\cdot)^{T231}$ applied to the third-order tensor $\mathscr{E} = \mathscr{E}_{ijk} g^i \otimes g^j \otimes g^k$ transforms it into $\mathscr{E}^{T231} = \mathscr{E}_{ijk} g^j \otimes g^k \otimes g^i$.

1.1.2 Virtual Work Principle

Consider the electromechanical virtual work principle (VWP) for a beam of length L with end loads and electric charges q_C per unit surface imposed on the surface boundary ∂V_P

$$\begin{array}{c} \int_V \delta\varepsilon : S dV + \int_{V_p} \delta E \cdot D dV_P = \int_A \delta x'(L) \cdot f(L) dA + \int_A \delta x'(0) \cdot f(0) dA \\ + \int_{A_P} \delta V(L) q(L) dA_P + \int_{A_P} \delta V(0) q(0) dA_P + \int_{\partial V_P} \delta V q_C d\partial V_P \end{array} \tag{1.7}$$

where V_P is the volume of the piezoelectric regions, $E = -V_{/\otimes}$ is understood, and q and q_C are the electric charges on the beam ends and the beam lateral surface, respectively. The electric charges are equal to the normal component of the electric displacement D, $q = D \cdot n$. The integral $\int_{\partial V_P} \delta V q_C d\partial V_P$ on the piezoelectric surface boundary ∂V_P is understood to be carried out only on the surface where the potential V is left free, i.e. where the surface charge can be imposed; wherever the potentials were imposed the electric charge would be unknown.

Following a well-consolidated procedure (e.g. [80, 85]) Eq. (1.7) can be transformed by integrating by part all the terms that have, as virtual variation, the derivative with respect to ξ^3 of either the deformed position vector x' or the electric potential V. This allows to transform Eq. (1.7) into a set of two differential equations in the ξ^3 direction. In doing so the volume integral involving the

contravariant base vector g^3 can be evaluated as $\int_V (\cdot) g^3 dV = \int_L \int_A (\cdot) n dA d\xi^3$, where A is the surface spanned by $\{\xi^1, \xi^2\}|_{\xi^3 = const}$. Integration by part leads to

$$\begin{array}{l} -\int_{V_P} \delta V_{/\otimes S} \cdot D dV_P + \int_{V_P} \delta V n \cdot D_{,3} dA_P d\xi^3 - \left[\int_{A_P} \delta V \left(n \cdot D - q \right) dA_P \right]_L \\ \quad + \left[\int_{A_P} \delta V \left(n \cdot D - q \right) dA_P \right]_0 = \int_{\partial V_P} \delta V q_C d\partial V_P, \end{array} \tag{1.8}$$

$$\begin{array}{l} -\int_V \delta x' \otimes n : S_{,3} dA d\xi^3 + \int_V \delta x'_{/\otimes S} : S dA d\xi^3 \\ + \left[\int_A \delta x' \cdot (S \cdot n - f) \right]_L - \left[\int_A \delta x' \cdot (S \cdot n - f) \right]_0 \quad = \quad 0. \end{array} \tag{1.9}$$

Equation (1.9) is derived by taking into account the symmetry of the stress tensor, so that $\delta\varepsilon : S = \delta F : S$. Using the constitutive law, eq. (1.5) and the definitions of the small strain tensor ε and electric field vector E, eqs. (1.3, 1.6), into eqs. (1.8, 1.9) introduces the second derivative of the deformed position and electric potential, $x'_{,33}$ and $V_{,33}$, and brings the equations to their final form. The terms at the boundary are nothing but the definition of the natural boundary conditions.

Equations (1.8, 1.9) can be reduced to a set of second order ordinary differential equations with a finite number of unknowns by using a finite element approximation. To do so, the unknown displacement $u = x' - x$ and electric potential V are interpolated over the cross sections by means of suitable interpolating functions N_{pi} and N_i, and the nodal values of the electric potential V_i and displacement u_i are assumed to be functions of the ξ^3 coordinate:

$$\begin{array}{c} V = \sum_i N_{pi}(\xi^1, \xi^2) V_i(\xi^3), \\ u = \sum_i N_i(\xi^1, \xi^2) u_i(\xi^3). \end{array} \tag{1.10}$$

The final result is the following set of second-order differential equations in the nodal unknowns:

$$\begin{array}{l} \left[\begin{array}{cc} M_{uu} & M_{uV} \\ M_{uV}^T & -M_{VV} \end{array} \right] \left\{ \begin{array}{c} u_{,33} \\ V_{,33} \end{array} \right\} + \left[\begin{array}{cc} \left(C_{uu}^T - C_{uu}\right) & \left(C_{Vu}^T - C_{uV}\right) \\ \left(C_{uV}^T - C_{Vu}\right) & \left(C_{VV} - C_{VV}^T\right) \end{array} \right] \left\{ \begin{array}{c} u_{,3} \\ V_{,3} \end{array} \right\} \\ \quad + \left[\begin{array}{cc} -E_{uu} & -E_{uV} \\ -E_{uV}^T & E_{VV} \end{array} \right] \left\{ \begin{array}{c} u \\ V \end{array} \right\} = \left\{ \begin{array}{c} 0 \\ Q_C \end{array} \right\}, \end{array} \tag{1.11}$$

or, with a more compact notation,

$$M \left\{ \begin{array}{c} u_{,33} \\ V_{,33} \end{array} \right\} + H \left\{ \begin{array}{c} u_{,3} \\ V_{,3} \end{array} \right\} + E \left\{ \begin{array}{c} u \\ V \end{array} \right\} = \left\{ \begin{array}{c} 0 \\ Q_C \end{array} \right\}. \tag{1.12}$$

The matrices of eq. 1.11 are obtained taking into account the symmetries of the elastic tensor $\mathbb{E}$, the symmetry of the third order tensor $\mathscr{E} = \mathscr{E}^{T132}$ and the symmetry of the second order tensor $\varepsilon = \varepsilon^T$. The domain of integration E is the area of a single finite element. All the sub-matrices have to be assembled, as it is customary.

$$M_{uu}(i,j) = \int_E N_i N_j n \cdot \mathbb{E} \cdot n dA \tag{1.13}$$

$$M_{uV}(i,j) = \int_E N_i N_{pj} n \cdot \mathscr{E}^{T231} \cdot n dA \tag{1.14}$$

$$M_{VV}(i,j) = \int_E N_{pi} n \cdot \varepsilon \cdot n N_{pj} dA \tag{1.15}$$

$$C_{uu}(i,j) = \int_E N_{i/\otimes S} \cdot \mathbb{E} \cdot n N_j dA \tag{1.16}$$

$$C_{uV}(i,j) = \int_E N_i n \cdot \mathscr{E}^{T231} \cdot N_{pj/\otimes S} dA \tag{1.17}$$

$$C_{Vu}(i,j) = \int_E N_{pi/\otimes S} \cdot \mathscr{E} \cdot n N_j dA \tag{1.18}$$

$$C_{VV}(i,j) = \int_E N_{pi/\otimes S} \cdot \varepsilon \cdot n N_{pj} dA \tag{1.19}$$

$$E_{uu}(i,j) = \int_E N_{i/\otimes S} \cdot \mathbb{E} \cdot N_{j/\otimes S} dA \tag{1.20}$$

$$E_{uV}(i,j) = \int_E N_{i/\otimes S} \cdot \mathscr{E}^{T231} \cdot N_{pj/\otimes S} dA \tag{1.21}$$

$$E_{VV}(i,j) = \int_E N_{pi/\otimes S} \cdot \varepsilon \cdot N_{pj/\otimes S} dA \tag{1.22}$$

Note that the matrix E_{uu} is four times singular because of three rigid translations and of the rigid rotation around the beam section ξ^3 axis. These rigid body motions must be constrained. The matrix E_{VV} is singular as well, because the electric potential is defined up to an independent constant for each independent electric region. Thus, it is singular as many times as the number of the independent piezoelectric regions. Conductive surfaces, i.e. equipotential surfaces, are not modeled explicitly, but they are represented by the nodes on the boundaries of each piezoelectric device. The same equation number is given to the nodes which represent the same electrode, so to satisfy the equipotentiality constraint along the section plane[1]*. Therefore, each electrode has a unique electric potential. Constraining the potential value of one electrode for each independent piezoelectric region brings matrix E_{VV} to full rank.*

1.1.3 Beam Section Characterization

Consider the internal work of the piezoelectric beam

$$\delta L_i = \int_V \delta\varepsilon : S dV + \int_{V_p} \delta E \cdot D dV_P \tag{1.23}$$

By following the same steps of the previous sections but without integrating by part, the internal work is equal to

$$\delta L_i = \int_L \begin{Bmatrix} \delta u_{,3} \\ \delta V_{,3} \\ \delta u \\ \delta V \end{Bmatrix}^T \begin{bmatrix} M_{uu} & M_{uV} & C_{uu}^T & C_{Vu}^T \\ -M_{uV}^T & M_{VV} & -C_{uV}^T & C_{VV}^T \\ C_{uu} & C_{uV} & E_{uu} & E_{uV} \\ -C_{Vu} & C_{VV} & -E_{uV}^T & E_{VV} \end{bmatrix} \begin{Bmatrix} u_{,3} \\ V_{,3} \\ u \\ V \end{Bmatrix} d\xi^3 \ , \tag{1.24}$$

or, with a shorter notation

$$\delta L_i = \int_L \delta q^T K_{FEM} q d\xi^3, \tag{1.25}$$

[1] Equipotentiality along the beam axis will be imposed in the stiffness matrix computation.

where $q = \left\{ \begin{array}{cccc} u_{,3}^T & V_{,3}^T & u^T & V^T \end{array} \right\}^T$ *is the* $(N \times 1)$ *vector of state variables.*

As in [85], the stiffness matrix of the beam is recovered by projecting the three dimensional problem into a suitable vector space. Therefore the six generalized deformations ψ *of the beam energetically conjugated to the internal forces and to the electric potentials applied on the* n_C *independent electrodes* V_C *become the new generalized coordinates. We then assume that the state variable q can be approximated as*

$$q \approx \left[Q_{st} \, Q_p \right] \left\{ \begin{array}{c} \psi \\ V_C \end{array} \right\}, \tag{1.26}$$

where matrices Q_{st} *and* Q_p *are* $(N \times 6)$ *and* $(N \times n_c)$*, respectively. The matrix* Q_{st} *represents the beam section behavior for a null electrode potential, i.e. for null forcing terms in Eq. (1.11). The matrix* Q_p*, instead, describes the beam behavior whenever an electric potential is applied, i.e. it describes a particular solution of eq. (1.11). Substituting (1.26) into eq. (1.25) leads to*

$$\delta L_i = \int_L \delta \left\{ \begin{array}{c} \psi^T \\ V_C^T \end{array} \right\} \left[Q_{st} \, Q_p \right]^T K_{FEM} \left[Q_{st} \, Q_p \right] \left\{ \begin{array}{c} \psi \\ V_C \end{array} \right\} d\xi^3. \tag{1.27}$$

The virtual work per unit length of the beam is the work of the generalized internal forces ϑ *and of the imposed electrodes charges* Q_c *for the virtual variations of the beam generalized deformations* $\delta\psi$ *and of the electrodes potential* δV_c*, respectively. It must be equal to the virtual work of the corresponding three dimensional solid, i.e. to the integrand of eq. (1.27). For a beam with linear constitutive laws the internal forces* ϑ *and electric charges* Q_c *can be computed as*

$$\left\{ \begin{array}{c} \vartheta \\ Q_c \end{array} \right\} = \left[\begin{array}{cc} K_{\psi\psi} & K_{\psi V} \\ -K_{\psi V}^T & K_{VV} \end{array} \right] \left\{ \begin{array}{c} \psi \\ V_C \end{array} \right\},$$

where the section stiffness matrix $K_{\psi\psi}$*, the actuation/sensor matrix* $K_{\psi V}$ *and the capacitance matrix* K_{VV} *define the overall generalized stiffness of the beam section and have dimension of* (6×6)*,* $(6 \times n_C)$ *and* $(n_C \times n_C)$*, respectively. Therefore, the following relation must hold*

$$\left\{ \begin{array}{c} \delta\psi \\ \delta V_C \end{array} \right\}^T \left[\begin{array}{cc} K_{\psi\psi} & K_{\psi V} \\ -K_{\psi V}^T & K_{VV} \end{array} \right] \left\{ \begin{array}{c} \psi \\ V_C \end{array} \right\} = \left\{ \begin{array}{c} \delta\psi \\ \delta V_C \end{array} \right\}^T \left[Q_{st} \, Q_p \right]^T K_{FEM} \left[Q_{st} \, Q_p \right] \left\{ \begin{array}{c} \psi \\ V_C \end{array} \right\} \tag{1.28}$$

for every possible $\delta\psi$*,* δV_C*,* ψ *and* V_C*, so that the beam section stiffness matrix can be computed as*

$$\left[\begin{array}{cc} K_{\psi\psi} & K_{\psi V} \\ -K_{\psi V}^T & K_{VV} \end{array} \right] = \left[Q_{st} \, Q_p \right]^T K_{FEM} \left[Q_{st} \, Q_p \right].$$

The problem is to compute meaningful matrices Q_{st} *and* Q_p*, such that Eq. (1.26) do well approximate the overall beam behavior. The procedure, already explained in [85] for the matrix* Q_{st}*, is discussed in the following paragraphs. The two matrices* Q_{st} *and* Q_p *can be computed independently and the computation of the stiffness matrix requires three steps:*

1. *a linear combination* $\tilde{Q}_{st}$ *of the columns of* Q_{st} *is determined in Section 1.1.3.1 by exploiting the homogeneous problem of equations (1.11) with the electrodes of each independent piezoelectric region short–circuited;*

2. *the matrix Q_p is determined in Section 1.1.3.2 by computing the particular solution of the problem (1.11); this can be accomplished either by imposing the electric charge per unit length on the electrodes, and solving for the unknown independent electrodes potential, or by directly imposing the potentials and computing the unknown charges.*

3. *the matrix Q_{st} is computed from $\tilde{Q}_{st}$ in Section 1.1.3.3 by imposing that the beam generalized deformations must be, by definition, energetically conjugated to the internal forces computed for the three dimensional beam model.*

The procedure is detailed in paragraphs 1.1.3.1–1.1.3.3 below.

1.1.3.1 Homogeneous Solution

Equations (1.12) can be reduced to a system of first order differential equations

$$\begin{bmatrix} M & 0 \\ 0 & I \end{bmatrix} q_{,3} = \begin{bmatrix} -H & -E \\ I & 0 \end{bmatrix} q + \begin{Bmatrix} Q_C \\ 0 \end{Bmatrix} \tag{1.29}$$

or, with a shorter descriptor form notation

$$Dq_{,3} = Aq + BQ_C. \tag{1.30}$$

The first term of the vector base $\tilde{Q}_{st}$ can be determined through the solution of the homogeneous problem of Eq. (1.30) with short–circuited electrodes. The piezoelectric electrodes equipotentiality along the beam axis implies not only that the electrode potentials are null, but also their derivatives. The homogeneous short–circuited problem

$$\tilde{q}_{,3} = \tilde{A}\tilde{q} \tag{1.31}$$

has 12 null eigenvalues, as shown in [85]. The solutions corresponding to the null eigenvalues are organized in four polynomial Jordan chains; each chain originates from one of the four rigid body motions of the section, and represent the central solution of the beam. Two polynomial chains grows up to a third order polynomial, while the other two grow up to a linear polynomial. All the remaining solutions of the homogeneous short–circuited problem are exponentially decaying, and are called extremity solutions. Since we are neglecting end effects, only the polynomial solutions are of interest. The sought fourth polynomial solutions assume the following form

$$\tilde{q} = \begin{bmatrix} x_1 & x_2 & x_3 & x_4 \end{bmatrix} \begin{bmatrix} 1 & \xi^3 & \frac{(\xi^3)^2}{2} & \frac{(\xi^3)^3}{6} \\ 0 & 1 & \xi^3 & \frac{(\xi^3)^2}{2} \\ 0 & 0 & 1 & \xi^3 \\ 0 & 0 & 0 & 1 \end{bmatrix} k, \tag{1.32}$$

where the vector k defines the amplitude of each polynomial. The generalized eigenvectors x_i, $i = \{1,2,3,4\}$ of the homogeneous problem can be computed by resolving a set of systems of linear equations:

$$\begin{aligned} Ed_0 &= 0 \\ Ed_1 &= -Hd_0 \\ Ed_i &= -Hd_{i-1} - Md_{i-2},\ i \geq 2 \end{aligned} \tag{1.33}$$

Note that a similar approach was suggested also by [91]. The initial eigenvectors d_0 are known beforehand: they represent the four rigid motions stemming from the null space of E. In fact, matrix E is four times singular and has to be constrained while resolving the Jordan chains. The resulting generalized eigenvectors are computed as follows

$$x_1 = \begin{bmatrix} 0 \\ d_0 \end{bmatrix} \quad \dots \quad x_i = \begin{bmatrix} d_{i-1} \\ d_i \end{bmatrix} \tag{1.34}$$

Once the 12 *generalized eigenvectors are computed, the vector base Q_{st} is constructed by using only the* 6 *eigenvectors which contribute to the deformation of the beam. These vectors are respectively the last two vectors associated to the bending and the last vector related to the axial and to the torsional rigid motions:*

$$\tilde{Q}_{st} = \begin{bmatrix} x_{3bend1} & x_{4bend1} & x_{3bend2} & x_{4bend2} & x_{2axial} & x_{2torsional} \end{bmatrix}. \tag{1.35}$$

1.1.3.2 Particular Solution

In order to compute the vector base Q_p we exploit the particular solution of Eq. (1.12). This allows to compute the solution when an electric potential is applied to the electrodes. Since the applied potential V_c is constant, the particular solution is constant as well. Considering eq. (1.12), the particular solution is given by

$$E \begin{Bmatrix} u \\ V \end{Bmatrix}_{pt} = \begin{Bmatrix} 0 \\ Q_C \end{Bmatrix}. \tag{1.36}$$

As stated before, the matrix Q_p can be computed either by imposing the electric charge per unit length on the electrodes, or by directly imposing the electric potentials. If the first approach is used, unit and opposite charges Q_C are applied at the master and slave electrode for each piezoelectric region and the solution $\begin{Bmatrix} u \\ V \end{Bmatrix}_{pt}$ is then computed. Since we are interested in the behavior of the beam under unit applied electric potential at the electrodes V_C, and not to unit charges, the matrix built with the different solutions as columns must be multiplied at the right by the inverse matrix of the electrodes electric potentials. If the second approach is used instead, i.e. if the solution is directly computed by applying unit electric potential difference on each piezoelectric region, no post-processing is required.

Since the particular solution is constant, its derivative is zero and the sought vector base Q_p is

$$Q_p = \begin{bmatrix} 0 \\ \begin{Bmatrix} u \\ V \end{Bmatrix}_{pt} \end{bmatrix} \tag{1.37}$$

1.1.3.3 Computation of the Generalized Beam Stiffness Matrix

Having computed the generalized eigenvectors $\tilde{Q}_{st}$ and the solution Q_p for applied unit potential on the electrodes V_C the state variable vector q can be approximated as

$$q = \begin{bmatrix} \tilde{Q}_{st} \, Q_p \end{bmatrix} \begin{Bmatrix} k_d \\ V_C \end{Bmatrix} \tag{1.38}$$

where vector k_d defines the amplitude of the 6 eigenvectors. However, the vector k_d is not, in general, energetically conjugated to the internal forces of the beam. A further step is thus needed in order to compute the correct stiffness matrix. Following the same approach as [85], a coordinate transformation G is sought for the short–circuited solutions so that

$$k_d = G\psi. \tag{1.39}$$

This is equivalent to transform the state variable vector q through a linear combination of the columns of matrix $Q_{st} = \tilde{Q}_{st}G$. Consider the internal work per unit length of the beam (1.25) projected onto k_d:

$$\delta\tilde{L}_i = \delta\psi^T G^T \tilde{Q}_{st}^T K_{FEM} \tilde{Q}_{st} G\psi = \delta\psi^T G^T \widetilde{K} G\psi. \tag{1.40}$$

The transformation matrix G is obtained by imposing that the internal work of Eq. (1.40) must be equal to the external work. Since the piezoelectric regions are kept short–circuited the external work is equal to the product of the virtual generalized deformations and the internal forces of the beam,

$$\delta\tilde{L}_{istruct} = \delta\psi^T \vartheta, \tag{1.41}$$

where the internal forces are defined as

$$\vartheta = \int_A \begin{bmatrix} I \\ x_\times \end{bmatrix} S \cdot n dA. \tag{1.42}$$

Consider the constitutive law $S = \mathbb{E}\varepsilon - e^T E$ and Eqs. (1.1) and (1.6). The structural external work can be computed as

$$\delta\tilde{L}_{istruct} = \delta\psi^T \begin{bmatrix} L^T & Y^T & R^T & Z^T \end{bmatrix} \tilde{Q}_{st} k_d = \delta\psi^T \begin{bmatrix} L^T & Y^T & R^T & Z^T \end{bmatrix} \tilde{Q}_{st} G\psi, \tag{1.43}$$

where the matrices L, Y, R and Z are computed from Eq. (1.42) with the finite element discretization of Eq. (1.10). Equating Eqs. (1.40) and (1.43) leads to

$$\delta\psi^T G^T \widetilde{K} G\psi = \delta\psi^T \begin{bmatrix} L^T & Y^T & R^T & Z^T \end{bmatrix} \tilde{Q}_{st} G\psi. \tag{1.44}$$

Note that only the structural deformations have to be transformed. Equation (1.44) must be verified for every possible deformation $G\psi$, so it is equivalent to a system of linear equations

$$\widetilde{K}^T G = \tilde{Q}_{st}^T \begin{bmatrix} L^T & Y^T & R^T & Z^T \end{bmatrix}^T. \tag{1.45}$$

Then the sought coordinate transformation G can be found by solving Eq. (1.45). The generalized stiffness matrix K of the beam section can finally be computed as

$$K = \begin{bmatrix} G & 0 \\ 0 & I \end{bmatrix}^T \left[\tilde{Q}_{st}\, Q_p\right]^T K_{FEM} \left[\tilde{Q}_{st}\, Q_p\right] \begin{bmatrix} G & 0 \\ 0 & I \end{bmatrix}. \tag{1.46}$$

After having computed the stiffness matrix, the finite element model of the beam can be obtained as usual, considering that the generalized deformations ψ can be expressed as a combination of the

Table 1.1: Piezoelectric material properties.

Piezoelectric (PZ21)	
$E_{11} = E_{22}$, GPa	5.9017E+1
E_{33}, GPa	4.0906E+1
ν_{12}	0.3413
$\nu_{13} = \nu_{23}$	0.3856
$G_{12} = G_{23} = G_{13}$, GPa	2.2E+1
$\mathscr{E}_{311}$, C/m^2	-5.3979
$\mathscr{E}_{322}$, C/m^2	-5.3979
$\mathscr{E}_{333}$, C/m^2	2.2836E+1
$\varepsilon_{11} = \varepsilon_{22}$, F/m	3.1892E-8
ε_{33}, F/m	1.3846E-8

displacements of the beam axis as in [92]

$$\psi = \begin{Bmatrix} \psi_1 \\ \psi_2 \\ \psi_3 \\ \gamma_1 \\ \gamma_2 \\ \gamma_3 \end{Bmatrix} = \begin{Bmatrix} s_{1,3} \\ s_{2,3} \\ s_{3,3} \\ \alpha_{1,3} \\ \alpha_{2,3} \\ \alpha_{3,3} \end{Bmatrix} + \begin{bmatrix} 0 & 0 & 0 & 0 & 0 & 0 \\ 0 & 0 & 0 & 0 & 0 & -1 \\ 0 & 0 & 0 & 0 & 1 & 0 \\ 0 & 0 & 0 & 0 & 0 & 0 \\ 0 & 0 & 0 & 0 & 0 & 0 \\ 0 & 0 & 0 & 0 & 0 & 0 \end{bmatrix} \begin{Bmatrix} s_1 \\ s_2 \\ s_3 \\ \alpha_1 \\ \alpha_2 \\ \alpha_3 \end{Bmatrix} \tag{1.47}$$

where s_i and α_i are the three translations and the three rotations of the beam axis respectively.

1.1.4 Examples

The first two examples deal with beams made of homogeneous material and thin piezoelectric patches. The host structure material is an isotropic epoxy resin with elastic modulus $E = 3.5$ GPa and Poisson coefficient $\nu = 0.34$. An orthotropic piezoceramic material is used for the piezoelectric patches. Table 1.1 reports the piezoelectric material properties computed in a local coordinate system, with the polarization applied in the direction of the local z axis. The stiffness matrix computed with the proposed method is compared with results obtained using the software Abaqus and, when available, with literature results obtained with ANBA [82] and VABS [84].

1.1.4.1 Example 1 : Beam with two Piezoelectric Patches

In this example a rectangular beam section with two piezoelectric actuators is considered. Two piezoelectric patches are attached on the upper and lower faces of the beam, as shown in Fig. 1.2. The beam core is 0.1x0.05 m and the piezoelectric patches are 0.002 m thick. The beam section is discretized with a 6x6 mesh, the piezoelectric patches with one element through the thickness. The electrodes are represented by the nodes on the sides above and below the piezoelectric patches; the potentials on the

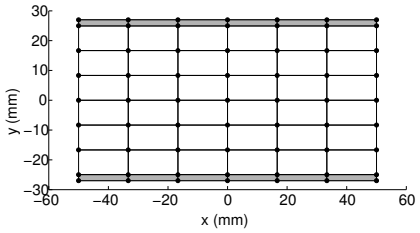

Figure 1.2: Rectangular section.

Table 1.2: Rectangular section beam properties.

$K_{\psi\psi}$		$K_{\psi V}$		K_{VV}	
EA, N	4.1107E+07	T_{zV1}, C/m	1.627	C_{ii}, F/m	1.2688E-6
$(GA)_x$, N	1.3074E+07	T_{zV2}, C/m	1.627	C_{ij}, F/m	-2.1555E-8
$(GA)_y$, N	6.8735E+06	M_{xV1}, C	-4.254E-2		
GJ, Nm^2	1.2050E+4	M_{xV2}, C	4.254E-2		
$(EJ)_x$, Nm^2	1.9673E+4				
$(EJ)_y$, Nm^2	3.4482E+4				

electrodes in contact with the core of the section are fixed to zero, so that the electric fields have the same direction of the material polarization (direction 3 of Tab. 1.1).

The computed stiffness matrix is reported in Tab. 1.2. A three dimensional beam of length 2 m has been analyzed with Abaqus, with isostatic constraints applied on one of the sections. Two load conditions are considered. In the first one an electric potential of 1000 V is applied on both electrodes. In the second one the same electric potential is applied on the lower electrode only. In order to compare the deformations obtained with the present method and the ones obtained with the three dimensional model, the results of the latter needs to be post-processed. The axial beam deformation is estimated as the mean value, computed over the section, of the three dimensional axial deformation. The curvature around the y axis is estimated as the derivative of the section rotation, and is computed by dividing the rotation of the end section by the total beam length. Table 1.3 compares the computed

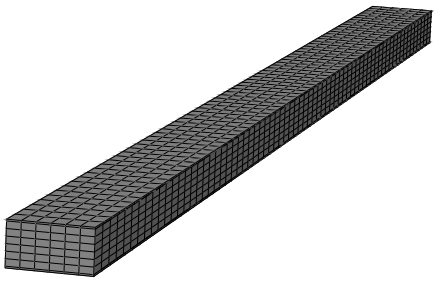

Figure 1.3: Rectangular section beam Abaqus model.

Table 1.3: Rectangular section beam: deformation obtained by applying a 1000 V potential to both (left) and one (right) electrodes.

	both electrodes		lower electrode	
	Present	Abaqus	Present	Abaqus
Axial deformation ψ_z	-7.9159E-5	-7.8498E-5	-3.958E-5	-3.8671E-5
Curvature γ_x	0.0	0.0	2.1623E-3	2.1072E-3

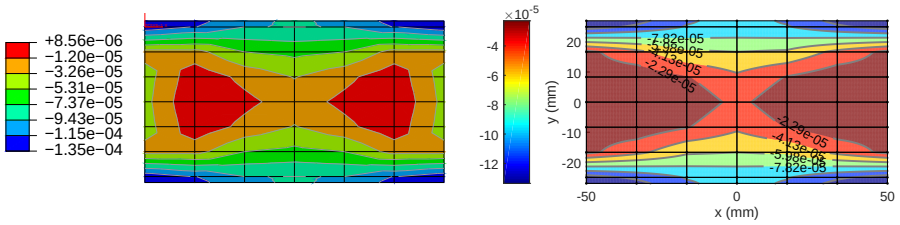

Figure 1.4: Triangular section beam with 100 V applied on the lower electrode: ε_{11}. Abaqus 3D model (left) and present beam section model (right).

deformations.

Figures 1.4 and 1.5 compare the deformation field $\varepsilon_{11}$and ε_{12} predicted, when an electric potential of 1000 V is applied on both electrodes. They are based on the Abaqus model and the proposed section characterization procedure. It should be remarked that the contouring algorithms used by Abaqus and by the present beam section code are different. Abaqus plots the contour after computing, for each material domain, the nodal average of a deformation. The beam section code, instead, post-processes a deformation by projecting it onto the same finite element space used to approximate its parent displacement.

1.1.4.2 Example 2 : Triangular Section

The triangular section of Fig. 1.6 was first considered in [82]. The section core is made of epoxy resin, with three piezoelectric patches attached to each side of the beam. The polarization direction of the piezoelectric materials is normal to the sides of the section and points to the host structure

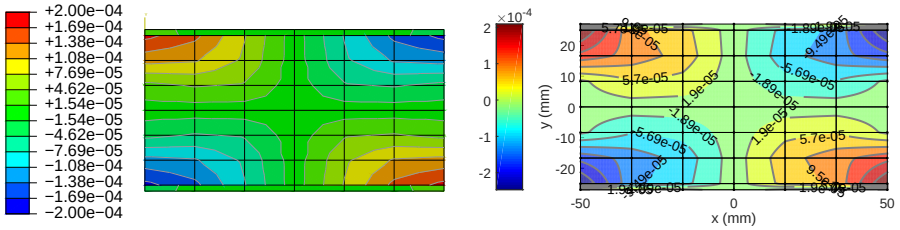

Figure 1.5: Triangular section beam with 100 V applied on the lower electrode: ε_{12}. Abaqus 3D model (left) and present beam section model (right).

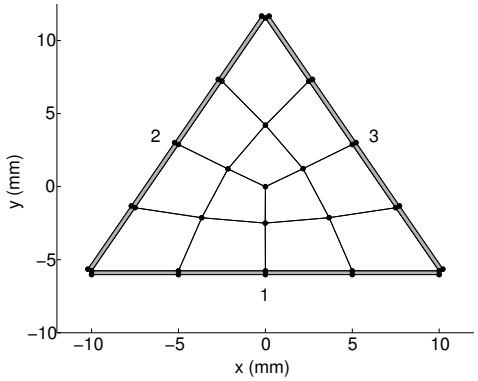

Figure 1.6: Triangular section.

Table 1.4: Triangular section beam properties.

	$K_{\psi\psi}$	
	Present	ANBA
EA, N	1.4915E+6	1.4915E+6
$(GA)_x$, N	3.7123E+5	3.70485E+5
$(GA)_y$, N	3.7122E+5	3.70485E+5
GJ, Nm^2	1.8189E+1	1.8156E+1
$(EJ)_x$, Nm^2	4.0748E+1	4.0749E+1
$(EJ)_y$, Nm^2	4.0747E+1	4.0749E+1

	K_{VV}	
	Present	ANBA
C_{ViVi}, F/m	1.9269E-6	1.9303E-6
$C_{ViVj,i\neq j}$, F/m	-1.7807E-8	-2.075E-8

	$K_{\psi V}$	
	Present	ANBA
T_{zV1}, C/m	0.32549	0.3255
T_{zV2}, C/m	0.32549	0.3255
T_{zV3}, C/m	0.32549	0.3255
M_{xV1}, C	-1.9486E-3	-1.929E-3
M_{xV2}, C	9.741E-4	9.77E-4
M_{xV3}, C	9.741E-4	9.77E-4
M_{yV1}, C	2.3E-8	2.8E-10
M_{yV2}, C	1.685E-3	1.6927E-3
M_{yV3}, C	-1.685E-3	-1.6927E-3

center. The three inner electrodes are unloaded, with the electric potential applied to the outer ones. The electrodes are numbered as in Fig. 1.6. The beam core sides are 0.02 m wide; the piezoelectric patches are .25 mm thick. The beam section has 4 elements on each side, with one element through the thickness for the piezoelectric patches. The center of the triangular section is located in the origin of the reference system. The results, shown in Table 1.4, are almost indistinguishable from those reported in [82], obtained with the ANBA code. As for the previous example, the behavior of a three dimensional beam of length 0.5 m has been analyzed with Abaqus. Two load conditions are considered. In the first one an electric potential of 100 V is applied on each electrode; only the lower electrode is loaded in the second load condition. The deformations of the three dimensional model are post-processed as in the previous example. As can be seen form Tab. 1.5 the results obtained with the three dimensional model and the proposed method show a good agreement. Figures 1.8 and 1.9 compare the deformation fields $\varepsilon_{11}$and ε_{12}, as predicted, for this case, by the three dimensional Abaqus model and the proposed section characterization procedure.

This test case is used as a mean to verify the effectiveness of modeling this kind of structures as beams characterized by the computed stiffness matrix. To do so, the axis displacement due to 100 V

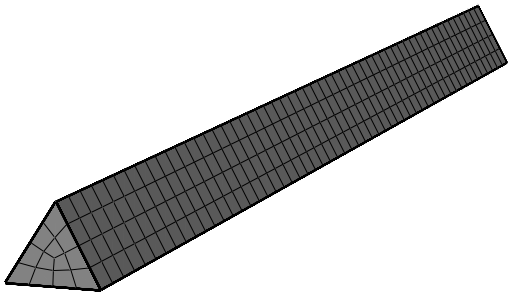

Figure 1.7: Triangular section beam Abaqus model.

Table 1.5: Deformation due to a 100 V applied to all electrodes (left) and to the lower electrode (right).

	all electrodes		lower electrode	
	Present	Abaqus	Present	Abaqus
Axial deformation ψ_z	-6.547E-5	-6.4235E-5	-2.1823E-5	-2.1409E-5
Curvature γ_x	0.0	0.0	0.478E-2	0.466E-2

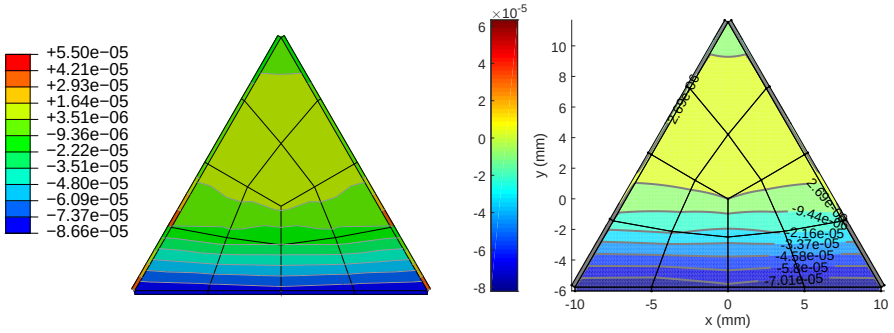

Figure 1.8: Triangular section beam with 100 V applied on the lower electrode: ε_{11}. Abaqus 3D model (left) and present beam section model (right).

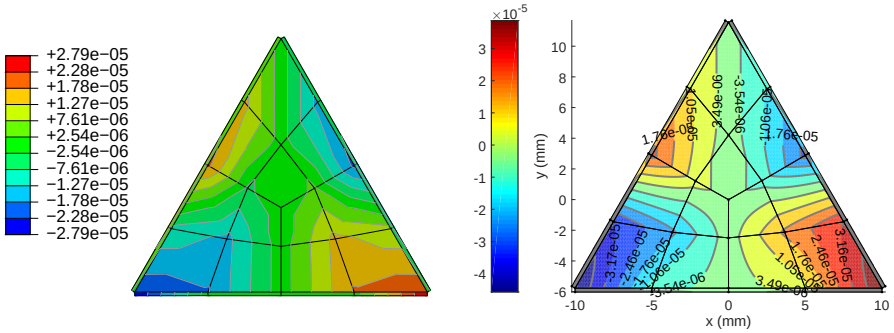

Figure 1.9: Triangular section beam with 100 V applied on the lower electrode: ε_{12}. Abaqus 3D model (left) and present beam section model (right).

Table 1.6: Displacements of the end section.

	Present	Abaqus
s_x, m	-4.954E-4	-4.986E-4
s_y, m	2.860E-4	2.879E-4
s_z, m	-1.091E-5	-1.063E-5

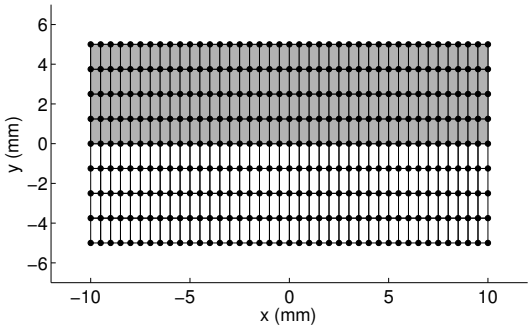

Figure 1.10: Two layered section.

on the left electrode is computed by means of a beam model and compared with that of the three dimensional FEM analysis. The beam model uses the stiffness matrix of Tab. 1.4 and has the same discretization along the beam axis of the three dimensional model. Table 1.6 compares the beam end section displacements with the average end section displacements of the 3D FEM model.

1.1.4.3 Example 3 : Two Layered Beam

The case study analyzed by [84] is considered. The rectangular cross section is composed of an aluminum layer bounded to a thick piezoelectric layer. A voltage of 10 kV is applied on the surface of the piezoelectric material, with the interface between the piezoelectric and the aluminum layers grounded. The piezoelectric material is polarized along the global y axis, that corresponds to the piezoelectric local z axis. Both layers are 5 mm thick and the section is 20 mm wide. The mesh, shown in Fig. 1.10, has 40x8 elements. The aluminum elastic modulus is equal to $E = 68.9$ *GPa, its Poisson coefficient to* $\nu = 0.25$*. The properties of the piezoelectric material are reported in Tab. 1.7.*

The computed stiffness matrix is shown in Tab. 1.8. The results are compared with those reported by [84]; however, no comparison is possible for the shear stiffness since that work is based on the variational asymptotic method. The only significant difference in Tab. 1.8 is that for the torsional stiffness GJ, 122.18 Nm^2 *vs. 130.04 Nm*^{2}*. At a first glance, this could be imputed to the fact that VABS results are computed using 80 8-noded parabolic elements, while the present results are computed by using 320 4-noded bilinear elements. However, increasing the number of elements from 320 to 5120 brings the torsional stiffness from 122.18 Nm*^{2} *down to 121.78 Nm*^{2}*.*

Table 1.7: Material properties.

	PZT4
$E_{11} = E_{22}$, GPa	8.13E+1
E_{33}, GPa	6.45E+1
ν_{12}	0.329
$\nu_{13} = \nu_{23}$	0.432
G_{12}, GPa	3.06E+1
$G_{13} = G_{23}$, GPa	2.56E+1
$\mathscr{E}_{311} = \mathscr{E}_{322}$, C/m^2	-5.2
$\mathscr{E}_{333}$, C/m^2	1.508E+1
$\mathscr{E}_{212} = \mathscr{E}_{123}$, C/m^2	1.27E+1
$\varepsilon_{11} = \varepsilon_{22}$, F/m	6.761E-9
ε_{33}, F/m	5.874E-9

Table 1.8: Comparison with the VABS method.

	$K_{\psi\psi}$	
	Present	VABS
EA, N	1.5026E+7	1.5026E+7
$K_{M_x s_z}$, Nm	3.0589E+3	3.0622E+3
$K_{T_x s_y}$, Nm	1.7179E+5	—
$K_{M_z s_x}$, Nm	1.1645E+3	—
$(GA)_x$, N	4.4191E+6	—
$(GA)_y$, N	4.2307E+6	—
GJ, Nm^2	1.2218E+2	1.3004E+2
$(EJ)_x$, Nm^2	1.2796E+2	1.2777E+2
$(EJ)_y$, Nm^2	5.0096E+2	5.0081E+2

	$K_{\psi V}$	
	Present	VABS
T_{zV}, C/m	-0.20263	-0.20245
M_{xV}, C	-4.832E-4	-4.8434E-4

	K_{VV}	
	Present	VABS
C, F/m	4.0073E-8	—

1.2 Extension to Piezomagnetic Beams

After having validated the semianalytical method for the computation of piezoelectric beam sections properties, this formulation can be easily extended to include the modeling of piezomagnetic materials to allow the correct representation of magneto-electro-elastic devices, which are very interesting for the vibration control of structures as shown in [93, 94]. Therefore there is the need to develop an appropriate beam model, capable of considering all the couplings of the different physical phenomena in an accurate way. A relevant work in the literature for the modeling of magneto-electro-elastic beams can be found in [95, 96, 97, 98], in which a dynamic two-dimensional beam model is built through the variational boundary element method. By using the same approach explained in the previous section for piezoelectric beam, the aim of this work is to extend the modeling of magneto-electro-elastic beam to the three dimensional domain, thus reducing the approximation assumptions.

The first step is the definition of the fully coupled linear constitutive law

$$\left\{ \begin{array}{c} S \\ D \\ B \end{array} \right\} = \left[\begin{array}{ccc} \mathbb{E} & -\mathscr{E}^{T231} & -\mathscr{D}^{T231} \\ \mathscr{E} & \varepsilon & \mathscr{G}^{T231} \\ \mathscr{D} & \mathscr{G} & \mu \end{array} \right] \left\{ \begin{array}{c} :\varepsilon \\ \cdot E \\ \cdot H \end{array} \right\}, \tag{1.48}$$

where μ is the magnetic permeability, $\mathscr{D}$ is the piezomagnetic constants tensor, $\mathscr{G}$ is the matrix describing the direct magneto-electric coupling, B is the magnetic induction and the magnetic field H is equal to minus the gradient of the magnetic potential ϕ,

$$H = -\phi_{/\otimes} = -\phi_{/\otimes S} - \phi_{,3} g^3. \tag{1.49}$$

After that, the virtual work principle of eq. 1.7 has to be completed by adding the following volume integrals that introduce the virtual work of the magnetic field H

$$\int_{V_M} \delta H \cdot B dV_M = \int_{A_M} \delta\phi(L) J(L) dA_M + \int_{A_M} \delta\phi(0) J(0) dA_M + \int_{\partial V_M} \delta\phi J_C d\partial V_M \ ,$$

where V_M is the volume of the piezomagnetic regions, and J and J_C are the current density on the beam ends and the beam lateral surface, respectively. The current density is equal to the normal component of the magnetic induction B, $J = B \cdot n$. The integral $\int_{\partial V_M} \delta\phi J_C d\partial V_M$ on the piezomagnetic surface boundary ∂V_M is understood to be carried out only on the surface where the potential ϕ is left free, i.e. where the surface current density can be imposed; wherever the potentials were imposed the electric charge would be unknown.

Following the sectional finite element discretization, the final result is a set of second-order differential equations

$$M \left\{ \begin{array}{c} u_{,33} \\ V_{,33} \\ \phi_{,33} \end{array} \right\} + H \left\{ \begin{array}{c} u_{,3} \\ V_{,3} \\ \phi_{,3} \end{array} \right\} + E \left\{ \begin{array}{c} u \\ V \\ \phi \end{array} \right\} = \left\{ \begin{array}{c} 0 \\ Q_C \\ J_C \end{array} \right\}. \tag{1.50}$$

As in the previous section, conductive surfaces, i.e. equipotential surfaces, are not modeled explicitly, but they are represented by the nodes on the boundaries of each piezoemagnetic device and they are treated in the same way as the piezoelectric conductors for the beam stiffness matrix computation. The sectional stiffness matrix K can be obtained with the same algorithm presented in the previous

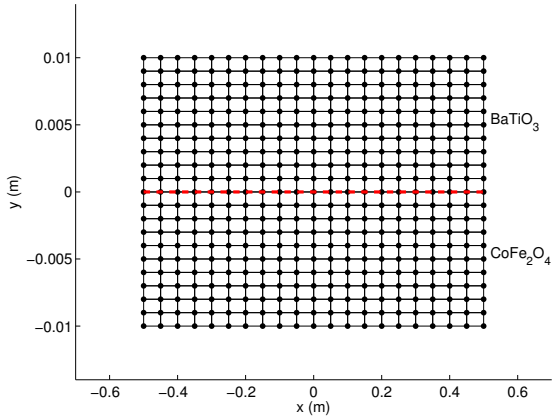

Figure 1.11: Two layered section.

section by exploiting both the homogeneous solution and the particular one of eq. 1.50, leading to the magneto-electro-elastic beam constitutive law

$$\left\{ \begin{array}{c} \vartheta \\ Q_C \\ J_C \end{array} \right\} = K \left\{ \begin{array}{c} \psi \\ V_C \\ \phi_C \end{array} \right\}.$$

Similarly to the piezoelectric beam, this relationship permits to model both piezomagnetic actuators, by imposing the magnetic potential ϕ_C on the conductive surfaces and piezomagnetic sensors considering the three dimensional couplings.

1.2.1 Example

The validation of the proposed three-dimensional beam section analysis formulation for magneto-electro-elastic beams has been done by reproducing the example reported in [96]. A simply supported two layered $CoFe_2O4/BaTiO_3$ laminated beam with a length $L = 0.3$ m and an overall thickness of $h = 0.02$ m, whose material properties are well detailed in [96], is studied. The beam undergoes a uniformly quasi-static distributed load $q = 1 - e^{(-t/0.15)}$ N/m, while the electric and magnetic potentials at the beam top surface are set to zero. The sketch of the layered beam section is shown in fig. 1.11. A total of 400 elements are used to discretize the beam section, while 100 beam elements approximate the beam axis.

In the reference, the authors analyze this problem through a boundary element method, thus performing a two-dimensional beam analysis. After reaching the steady state solution, the through the thickness distribution of both the electric potential and the magnetic one is observed at the section in the middle of the beam at $z = L/2$. Figure 1.12 reports the comparison of the potentials distribution between the boundary element method and the semianalytical method presented in this chapter. Being the proposed approach a three-dimensional one, the potential distribution is computed by averaging the potential values along the x axis. From the graphs it can be seen that even if the shape of the potentials distribution is the same for both approaches, the three-dimensional analysis exhibits higher electric and magnetic potential values.

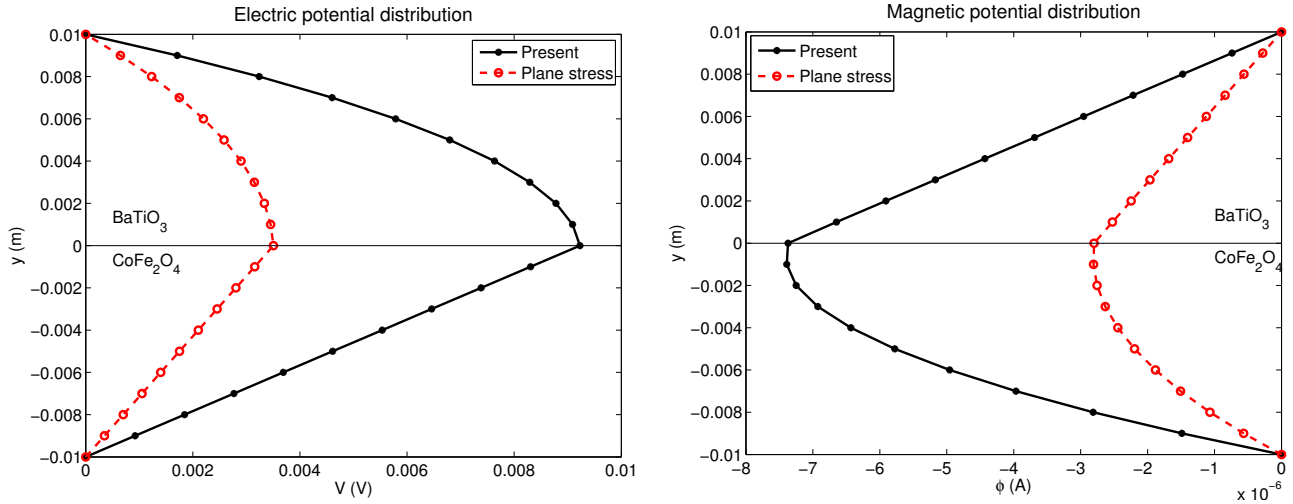

(a) Steady state through the thickness electric potential distribution at $z = L/2$.

(b) Steady state through the thickness magnetic potential distribution at $z = L/2$.

Figure 1.12: Comparison with ROSITA.

Although this example provides a first glimpse of the capabilities of the proposed approach, further comparisons have to be done by exploiting three-dimensional finite element analysis or experimental data to validate the magneto-elastic extension.

1.3 Multibody Rotor Model

The test case chosen as the subject of the simulations and analysis shown in the next chapters is an available numerical model of the Bo105 rotor [99]. It is a 4 blades hingeless rotor with only one physical hinge for the blade pitch, while the flap and lag main deflections are obtained through the deflection of an ad hoc designed flexbeam located at the blade root. In order to design an active twist rotor, which will be exploited throughout this thesis, capable of reducing hub loads vibrations by modifying the periodic aerodynamic loads in forward flight condition, the original blades of the Bo105 rotor are replaced with actively twisted ones, including macro-fiber composite (MFC) piezoelectric actuators with interdigitated electrodes. These actuators exploit the primary piezoelectric direction of polarization, thus allowing to achieve a high strain rate with low actuation power. They are oriented in such a way that the strain is applied at ± 45 *to generate maximum torsional authority.*

Since an accurate structural modeling is demanded for a reliable loads estimation, we decided to use the free software MBDyn [100, 101] to build the rotor model in a nonlinear multibody environment. MBDyn is a general purpose multibody software developed at Politecnico di Milano by the Dipartimento di Scienze e Tecnologie Aerospaziali. This code deals with Initial Value Problems (IVP) by solving Differential Algebraic Equations (DAE). The equations of motion are based on Newton-Euler principles and the kinematic constraints are enforced through Lagrange multipliers. It is also possible to model flexible bodies as nonlinear beams and plates with the full constitutive law of the material.

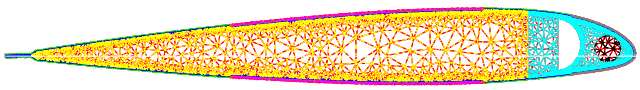

Figure 1.13: Blade section discretization.

Table 1.9: Mass properties of the piezoelectric section.

Data	Piezoelectric section
x_{CG}	$-1.5 \cdot 10^{-3}$ m
y_{CG}	$3.92 \cdot 10^{-3}$ m
M	5.843 Kg/m
I_{XX}	$6.792 \cdot 10^{-4}$Kgm
I_{yy}	$3.118 \cdot 10^{-2}$ Kgm
I_{ZZ}	$3.186 \cdot 10^{-2}$ Kgm

In the developed multibody model the swashplate and the pitch links are represented with rigid bodies, and each blade is modeled using five geometrically exact finite volume nonlinear beam elements [102]. MBDyn is also able to handle piezoelectrically actuated beams provided the stiffness and the piezoelectric coupling matrices of the blade section are known. The beam section stiffness and and mass data of the original Bo105 blades are known. The section properties of the actively twisted blades, on the contrary, have to be computed. An accurate way to compute such properties, still accounting for three dimensional elastic and piezoelectric constitutive laws, is the semianalytical approach described in [103, 104, 105]. The three dimensional continuum is decomposed into the one dimensional domain of the beam model and the two dimensional domain of the beam section. A finite element discretization of the beam section, such as that shown in fig. 1.13, allow to compute, by means of the previously shown semi-analytic procedure, the sought generalized beam section stiffness matrix. Such a method was already used to optimize the piezoelectric blade section in [91]; the position of the elastic axis and of the center of mass were constrained during the optimization to avoid aeroelastic instabilities. Considering the blade section in fig. 1.13 with the x axis along the blade span and the y axis pointing from the trailing edge to the leading edge located in the elastic axis of the section at 25% of the chord, the computed mass properties of the equivalent beam section are reported in tab. 1.9, where x_{CG} and y_{CG} are the position of the center of mass with respect to the elastic axis of the blade section, M is the weight per unit length and I_{XX}, I_{YY} and I_{ZZ} are the inertia moments per unit length. The semianalytical method used to determine the blade stiffness matrix $\mathbf{K}_{\psi\psi}$, shown in eq. 1.51, provides a full $(6x6)$ relation taking into account all material couplings. It also computes the piezoelectric coupling matrix $\mathbf{K}_{VV}$, reported in eq. 1.52, which is used to transmit mechanical forces due to the electric potential V. The terms of the stiffness matrix $\mathbf{K}_{\psi\psi}$ are organized so that it multiplies the displacements related to the three linear displacements along x, y and z and the three curvature

Table 1.10: BO 105 model data with original and piezoelectric blade.

Rotor data	BO 105 blade	Piezoelectric blade
R	4.9 m	4.9 m
p	0.23 m	0.23 m
ϑ_p	2.5°	2.5°
c	0.3025 m	0.3025 m
ϑ_{tw}	−8°	−8°
Ω	44.4 rad/s	44.4 rad/s
α	3°	3°
ν_β	1.11	1.1
ν_ξ	0.69	0.73
ν_ϑ	3.63	3.89

along x, y and z, respectively.

$$\mathbf{K}_{\psi\psi} = \begin{bmatrix} 6601.878 & 211.403 & 1.86 & -1.073 & -12.462 & 72.417 \\ & 907.462 & 13.787 & 0 & 0.318 & 13.859 \\ & & 82.216 & 0 & -0.273 & 0.386 \\ & & & 0.658 & -0.072 & -0.075 \\ & & & & 0.822 & -0.749 \\ & & & & & 33.505 \end{bmatrix} \cdot 10^4 \tag{1.51}$$

$$\mathbf{K}_{VV} = \begin{Bmatrix} -128.245 \\ -85.34 \\ -8.343 \\ -1.948 \\ 2.393 \\ -9.09 \end{Bmatrix} \cdot 10^{-2} \tag{1.52}$$

Rotor data, together with the first frequencies of the original passive blades and of the optimized piezoelectric blades, are shown in tab. 1.10, where R is the blade radius, p is the pitch bearing position, ϑ_p is the precone angle, c is the blade chord, ϑ_{tw} is the blade twist, Ω is the rotor angular velocity, α is the shaft angle and ν_β, ν_ξ and ν_ϑ are the non-dimensional flap, lag and torsional frequency, respectively.

Even if MBDyn is a general purpose multibody software, it contains some specialized elements for the simulation of helicopter rotors; among them, it provides simple aerodynamic elements, such as the blade theory and linear inflow models. Taken together, these elements allow to quickly approximate the system response with a level of accuracy that is deemed suitable to reproduce representative vibratory loads in forward flight, at least for a preliminary design of the controller. The simulations were performed by combining the blade element method (BEM) with the Drees inflow model. The required data are the lift, drag and moment coefficients, C_L, C_D and C_M of the blade NACA 23012 airfoil, with respect to the Mach number and to the aerodynamic angle of attach. This rotor model will be later extensively used as a low fidelity model to design the vibration controller because of the low computational effort it requires.

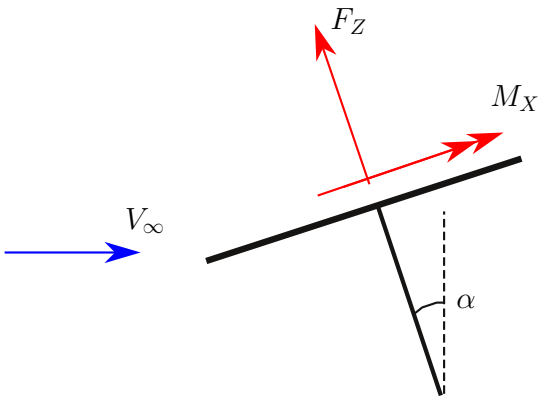

Figure 1.14: Rotor shaft inclination.

Table 1.11: BO 105 trim data.

Rotor forces	$\mu = 0.23$	$\mu = 0.33$
T_Z	20010 N	20200 N
M_X	740 Nm	1030 Nm
M_Y	-85 Nm	-1400 Nm

Once the multibody rotor model is built, the rotor is trimmed in forward flight at two advance velocity parameters $\mu = 0.23$ *and* $\mu = 0.33$. *The swashplate is set so that the rotor thrust and moments reproduce a realistic condition for both advance velocities. The rotor shaft is inclined forward by* 3° *and the chosen absolute reference frame, to which the hub forces are referred, is shown in fig. 1.14. Table 1.11 presents the target of the rotor forces for each trim configuration.*

The coupling between MBDyn and Simulink is already available, thus allowing aeroservoelastic simulations. MBDyn can be easily coupled to external softwares using bidirectional socket communication to exchange information between a server program and one or more client programs. The interface between the two programs is managed through Matlab MEX-functions. The closed loop simulation can be entirely performed in the Simulink environment, in which the multibody model of the rotor appears as Simulink blocks, hence there are no limitations imposed on the controller design.

Having developed a method to properly compute the sectional properties of helicopter beams, together with the nonlinear beam formulation of the multibody approach, it is possible to provide a high level of fidelidy for the rotor structural modeling. Althoug the aerodynamics provided by MBDyn is quite simple, it permits to have fast simulations while representing the main features of the rotor behavior, therefore it will be extensively used throughout this work to iteratively design the active vibration control systems, which will be then validated using more sophisticated aerodynamic models, presented in the following chapter.

Chapter 2

Hybrid Aerodynamic Models

The accurate prediction of the blades and hub loads of a rotor in forward flight is a very challenging task. The flow around the blade is unsteady with strong nonlinear and three dimensional effects, as transonic regions and dynamic stall. Moreover the wake shed by the blades generates a complex induced velocity distribution and blade vortex interactions (BVIs), which strongly modify the aerodynamic loads. Due to the rotary movement at high angular velocity and to the blade kinematics, the accurate modeling of the inertial couplings and the structural motion play an important role in the aeroelastic analysis as well.

While relying on multibody simulations with a beam model of the blades provides a sufficient level of accuracy for the structure with a relatively low computational effort, a complete aerodynamic model considering all the nonlinear effects is nowadays possible only through computational fluid dynamic (CFD), which requires a substantial computational time to perform a full rotor analysis [106, 107, 108]. For industrial users and during the design phase such expensive simulations are prohibitive and it is common practice to adopt simplified methods, without undue approximations in the modeling process. This approach is often referred as hybrid CFD method; the aerodynamic near field of the blade is solved with a CFD tool while the far field and the wake are modeled through simpler models, which are by far less expensive than CFD analysis. Several examples of this technique can be found in the literature. In [109] the near field of the blade is computed through a Navier-Stokes based CFD software and the rotor wake is approximated by a potential rigid/free wake obtained with a collection of piecewise linear bound and trailing tip vortex elements. Euler equations are used in [110] to compute the blade flow in the vicinity of the blade and full potential flow is considered to model the flow region far away from the rotor. A Lagrangian wake model is used to take into account the effect on other blades. A similar approach, in which the flow around the blade is modeled using Navier-Stokes based equations can be found in [111]. A hybrid code is developed in [112], where the Navier-Stokes solution of the blade aerodynamics is coupled with a far field wake modeled as trailing edge vortices of all blades. The approach proposed in [113] is a weak coupling between the wake and the Navier-Stokes based solution of the blade near field, in which the boundary conditions of the mesh boundaries are provided by a time marching free-wake rotor analysis computed with another software. Couplings between a Reynolds Averaged Navier-Stokes (RANS) solver and a free wake model of the blade tip vortices can be found in [114, 115, 116]. Another linearized method to realize a hybrid approach is presented in [117, 10, 118], where the CFD RANS-based code is used before the full rotor analysis to generate frequency domain aerodynamic response to basic motions. Subsequently, the

frequency domain loads are converted to the time domain using the Rational Function Approximation (RFA) approach. This procedure is repeated for different airfoil configurations leading to a parameter varying linearized state space model for the airfoil response, function of the Mach number, the airfoil angle of attach and position of the control surfaces. This model provides cross-sectional unsteady lift, moment, and drag coefficients that can be used at each time step of the simulation within the blade element theory. The RFA model is then linked to a free wake model. In the original RFA model the cross-sectional aerodynamic loads were obtained in the frequency domain using a doublet lattice unsteady potential flow solver [9].

Two different solutions to obtain a hybrid rotorcraft aerodynamics solver are proposed in this chapter. The goal of this work is to obtain an aerodynamic code that gives a good approximation of the rotor aerodynamics, which can be useful both for the preliminary rotor design and for the tuning and testing of control systems, hence without spending a great amount of simulation time. In the first method a greater attention is given to the blades and a full potential CFD solver is used to approximate the near field aerodynamics. In order to limit the simulation time the wake structure is not modeled and the induced velocity is computed through the Peters-He model, which enhances the higher harmonics content of the classical linear inflow ones. The second method does not rely on a CFD approach and the blade element method is improved considering unsteady effects and tip losses. In contrast to the first hybrid code, the free wake geometry of the tip vortices of the blades is modeled, providing a more sophisticate inflow estimation and the possibility to simulate blade vortex interactions (BVIs). The two methods are presented in the following sections and they are validated using experimental data of the Hart II rotor to assess their applicability and limitations.

2.1 Full Potential CFD with Peters-He Inflow

The aim of this section is to develop an aeroservoelastic rotor simulation tool with an intermediate level of accuracy between the classical blade element method with simple inflow models and a full potential CFD simulation, able to model the main features of the rotor behavior. The main goal is to overcome the limitations of the simple quasi-steady blade element method combined with linear inflow models available in MBDyn and to provide a hybrid code, which allows the user to perform fast simulations. To achieve our objectives, without losing the advantages of a multibody approach to model the structure, the multibody software MBDyn is coupled to the developed hybrid CFD code that simulates the rotor aerodynamics. The near field of all blades are simulated independently with a full potential software and the rotor wake is computed with the Peters-He inflow model, thus coupling the individual blade flow fields and considering higher harmonics in the predicted inflow. The choice of the potential flow approximation introduces some limitations, it is nonetheless adopted a fast aerodynamic solver. The use of the Peters-He inflow model represents a good compromise in view of enhancing the frequency content of the induced velocity, with respect to linear inflow approaches, without modeling the wake geometry.

2.1.1 Blade Aerodynamics

The aerodynamic loads of the rotor blades are computed using a two-field full potential formulation through the open source CFD software S^T developed at Dipartimento di Scienze e Tecnologie Aerospaziali, Politecnico di Milano [119]. Attached flows past aerodynamic bodies at high Reynolds

numbers ensure thin boundary layers and narrow vortical regions. The absolute motion field of such a flow can be suitably defined by a discontinuous velocity potential ϕ,

$$\vec{V} = \nabla\phi, \tag{2.1}$$

where the vorticity bounded to lines or surfaces is related to the jump of ϕ across them. This is the so-called quasi-potential flow. Assuming the viscous stress and the heat sources to be negligible, the governing equations of the flow are:

- *the continuity equation,*

$$\frac{\partial\rho}{\partial t} + \nabla\cdot(\rho\nabla\phi) = 0, \tag{2.2}$$

- *Bernoulli theorem,*

$$\frac{\partial\phi}{\partial t} + H - H_\infty = 0. \tag{2.3}$$

Both the potential function ϕ and the density function ρ can be defined on a reference domain R_G moving according to an absolute velocity field $\vec{V}_G$ on a spatial domain R_g. Let us define the integral form of the continuity equation, eq. 2.2, in the fixed spatial domain R_g:

$$\int_v \frac{\partial\rho}{\partial t} dv + \int_v \nabla\cdot\left(\rho\vec{V}\right) dv = 0. \tag{2.4}$$

Defining the total time derivative with respect to R_G as:

$$\frac{d*}{dt} = \frac{\partial*}{\partial t} + \nabla* \cdot \vec{V}_G, \tag{2.5}$$

and applying the divergence theorem the continuity equation, eq. 2.4, becomes:

$$\int_v \left(\frac{d\rho}{dt} - \nabla\rho\cdot\vec{V}_G\right) dv + \int_\gamma \rho\vec{V}\cdot\vec{n}d\gamma = 0, \tag{2.6}$$

which represents an Arbitrary Lagrangian Eulerian (ALE) formulation independent from the time derivative of the control volume. The Bernoulli theorem, eq. 2.3, in the spatial domain R_g with the fluid at rest is:

$$\frac{\partial\phi}{\partial t} + \frac{1}{2}|\nabla\phi|^2 + \frac{c_\infty^2}{\gamma-1}\left(\left(\frac{\rho}{\rho_\infty}\right)^{\gamma-1} - 1\right) = 0. \tag{2.7}$$

Applying the total time derivative, eq. 2.5, to the potential function the ALE form becomes

$$\frac{d\phi}{dt} - \nabla\phi\cdot\vec{V}_G + \frac{1}{2}|\nabla\phi|^2 + \frac{c_\infty^2}{\gamma-1}\left(\left(\frac{\rho}{\rho_\infty}\right)^{\gamma-1} - 1\right) = 0. \tag{2.8}$$

The related integral form is

$$\int_v \left(\frac{d\phi}{dt} - \nabla\phi\cdot\vec{V}_G + H - H_\infty\right) dv = 0. \tag{2.9}$$

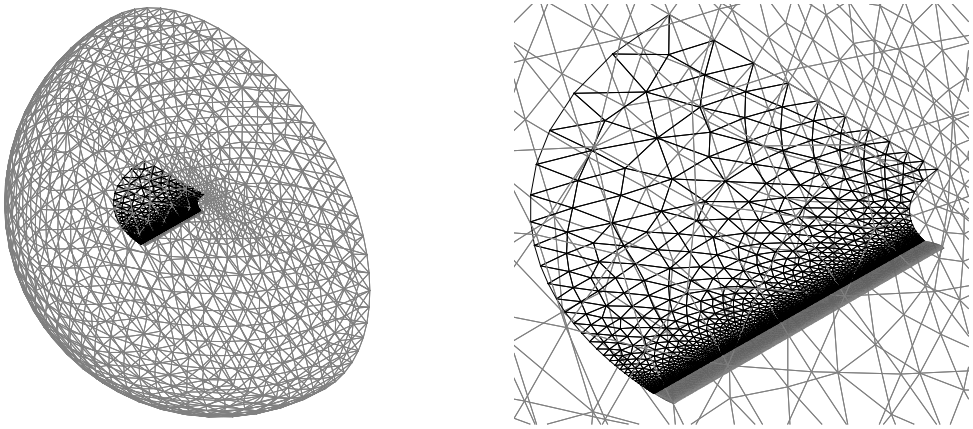

(a) External domain of the blade. (b) Blade mesh and wake discretization.

Figure 2.1: Aerodynamic mesh.

The integral equations, Eqs. 2.6 and 2.9, are treated trough a node centered finite volume discretization in space obtaining a set of first order nonlinear Ordinary Differential Equations (ODEs) in time:

$$A\frac{\partial x(t)}{\partial t} = f(x(t)), \qquad x^T = \left\{\rho^T \quad \varphi^T\right\}. \tag{2.10}$$

Thanks to the two fields approach the pressure continuity on the wake must also be applied easily,

$$\Delta(\rho) = 0. \tag{2.11}$$

The line/surface which represents the wake is part of the domain discretization and is not trimmed according to the motion field. The spatial discretization uses triangles and tetrahedrons and the approximation for ρ and φ is based on linear shape functions within each element with solution variables located at the vertices. Time marching solutions are obtained through a first/second order implicit integration schemes. References [120, 121, 122] should be consulted for a more detailed presentation of the discretization scheme, treatment of supersonic regions and boundaries, assembly of the discrete equations, implicit time marching integration and solution schemes.

The near field aerodynamics of each blade is simulated independently with the described full potential CFD method and a typical unstructured mesh of the blade is shown in fig. 2.1a, where the blade body is isolated form other blades and immersed in a hemispherical far field. Being the proposed CFD approach a potential one, it is necessary to set the structure and position of the blade's wake in the meshing process, as shown in fig. 2.1b.

2.1.2 Peters - He Generalized Wake Model

Since the aerodynamic near field of the blades is computed through a full potential CFD analysis, a compromise solution is here pursued for the rotor wake approximation, in order to provide a reasonable computational time. A full CFD analysis or the use of a time marching free wake method is avoided by adopting the finite states inflow model developed by Peters-He [12]. This method approximates the rotor inflow by considering a series expansion using higher harmonics both in the azimuth

ad blade radius coordinates; it is conceptually an evolution of the classical Pitt-Peters induced velocity model [11], which is steady and considers only constant and linear terms. Starting from the potential flow Laplace equations in elliptical coordinates, its solution can be found by using Legendre functions of the first and the second kind. By manipulating those equations it is possible to impose a solution for the vertical induced velocity, w, as function of the radius, r, the blade azimuth, ψ, and the nondimensional time, $\bar{t}$:

$$w = \sum_{k,j} \phi_j^k(r) \left[a_j^k(\bar{t}) cos(k\psi) + b_j^k(\bar{t}) sin(k\psi) \right] \tag{2.12}$$

where the flow potential, ϕ_j^k, is approximated with Legendre functions and the unknowns of the problem, a_j^k and b_j^k, are computed through the solution of the following system of equations

$$\begin{cases} \mathbf{G}\dot{\mathbf{a}} + 2V_\infty \mathbf{L}^{c^{-1}} \mathbf{a} = \tau^c \\ \mathbf{G}\dot{\mathbf{b}} + 2V_\infty \mathbf{L}^{s^{-1}} \mathbf{b} = \tau^s \end{cases} \tag{2.13}$$

where the superscript notation ^{c} ad ^{s} refers to the cosine and sine components. After deciding the number of the desired inflow harmonics in Eq. 2.12, k, the number of states, N_{states}, in the system of equations 2.13 can be computed as $N_{states} = k(k+1)/2$. For the computation of the terms of the matrices $\mathbf{G}$, $\mathbf{L}^c$ and $\mathbf{L}^s$ and a more detailed presentation of the theory, which is beyond the scope of this work, the reader is referred to [12, 123].

On the contrary it is interesting to recall the expressions of the generalized force components, τ^c and τ^s, because they are related to the lift of the blade and are the ones that allow the coupling between the near field blade analysis and the rotor wake. They can be computed as

$$\tau_j^{0c} = \frac{1}{2\pi} \sum_{q=1}^{n_{blades}} \left[\int_S \frac{P\mathbf{n}_z}{\rho\Omega^2 R^3} \phi_j^0(r) dS \right] \tag{2.14}$$

$$\tau_j^{kc} = \frac{1}{\pi} \sum_{q=1}^{n_{blades}} \left[\int_S \frac{P\mathbf{n}_z}{\rho\Omega^2 R^3} \phi_j^k(r) dS \right] cos(k\psi_q) \tag{2.15}$$

$$\tau_j^{ks} = \frac{1}{\pi} \sum_{q=1}^{n_{blades}} \left[\int_S \frac{P\mathbf{n}_z}{\rho\Omega^2 R^3} \phi_j^k(r) dS \right] sin(k\psi_q) \tag{2.16}$$

where P is the pressure, $\mathbf{n}_z$ is the z-component of the element normal, S is the surface of the lifting body and $r = \sqrt{x^2 + y^2}$ is the radial coordinate.

2.1.3 Aeroservoelastic Code Setup

The complete aeroservoelastic analysis tool is obtained by coupling MBDyn with Matlab, to simulate the rotor aerodynamics with the full potential software S^T and the Peters-He inflow model, and with Simulink to have no limitations in the controller design. MBDyn is already designed to be coupled with external softwares using bidirectional socket communications to exchange data and a conceptual block diagram of the simulation tool developed in this work is shown in fig. 2.2.

The coupling between MBDyn and Simulink is available in the original version of the software and can be easily configured. The user can entirely design the controller within the Simulink environment,

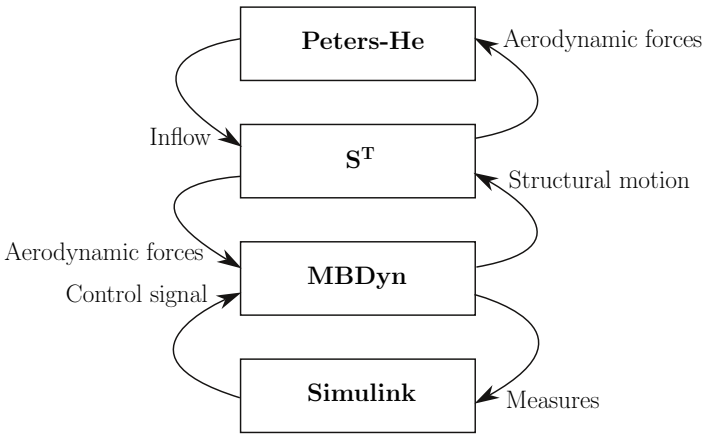

Figure 2.2: Aeroservoelastic code structure.

the two Simulink Blocks that read and write data for MBDyn being already provided by MBDyn itself. These blocks are connected with proper MBDyn functions that allow to manage the measures of the sensors and the control signals during the simulation.

While further modifications are not needed for the coupling with Simulink, the interface for Matlab has been developed to fulfill our goals. Since MBDyn supports the python language as a means to exchange data with external programs, it has been decided to exploit the free software matpy [124], which is a very useful python interpreter for Matlab. In particular the coupling interface was coded so that MBDyn sends the position and the velocity of the structural nodes of the blades to Matlab and receives the aerodynamic forces computed by S^T with the Peters-He inflow model. These operations are managed by using the "external structural mapping" *element of MBDyn. It also has an internal energy-conserving moving least squares algorithm [125] that permits to compute the aeroelastic interface matrix* $\mathbf{H}$ *between the blade structural and aerodynamic nodes,* $\mathbf{u}_s$ *and* $\mathbf{u}_a$*, which is in turn used also inside Matlab to map the structural displacements and velocities to the aerodynamic domain and to correctly compute the aerodynamic forces acting on the structural nodes, as shown in fig. 2.3.*

At each time step of the simulation the blade movement is considered in the CFD environment as a transpiration boundary condition together with the induced velocity computed by Peters-He, through which all the blades are coupled. The relation between S^T and the inflow model involves the computation of the generalized force components, τ^c and τ^s, where the pressure, P, on the blade is directly obtained from the CFD solution of S^T. Working with identical blades the computational effort and the required memory are considerably reduced with respect to a complete rotor model. In fact, the preprocessing phase, involving the calculation of normals, cells volumes etc, and the factorization for the numerical integration scheme, are computed only for one blade. Since a full potential formulation can model attached flows only and requires an a priori identification of a trailing edge to model lifting bodies, this approach is not capable to reproduce reverse flow conditions, which are experienced at the retreating blade root in high forward flight velocities. To avoid this problem we decided to neglect part of the blade root loads when reverse flow occurs, thus allowing an increased error in the loads estimate with the increasing forward flight speed. A further issue that has to be taken into account before coupling S^T to the Peters-He inflow model, is the role of the induced velocity of the blade's

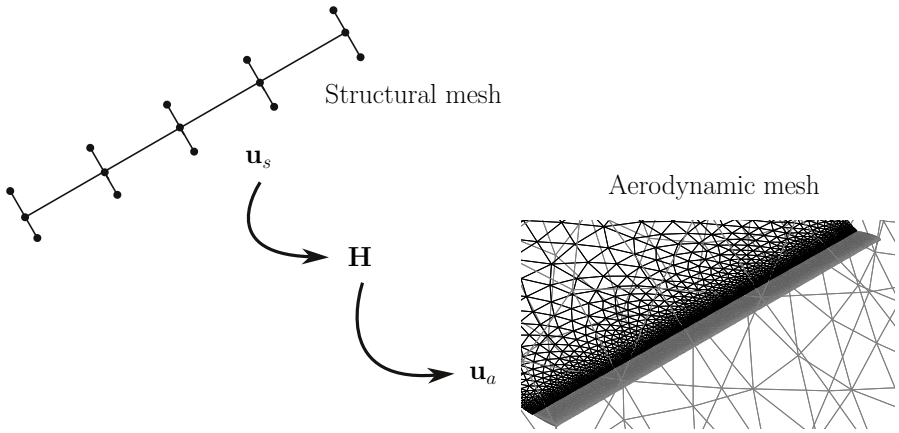

Figure 2.3: Aeroelastic interface handling.

wake computed by the CFD solver. Since the Peters-He model is formulated through the actuator disk model, it already considers all induced velocity sources and therefore the wake influence of each blade has to be subtracted during the simulation, otherwise the mean value of the inflow will be higher than expected. Therefore, the surface elements of the wake of fig. 2.1b are considered as panels having a circulation equal to the potential difference and their contribution to the blade induced velocity, computed through the Biot-Savart law, is subtracted at each time step.

2.1.4 Model Validation

The first simulation presented in this work is focused on the validation of the proposed hybrid aerodynamic approach. In fact, while the full potential code S^T has already been validated for fixed wing aircraft in [120, 121, 122], we want to test if the adaptation for rotary wing simulations and the coupling with the Peters-He inflow model to reproduce the rotor wake gives reasonable and reliable results. To this aim a simple blade using the NACA 0012 airfoil is taken into account. The blade has a chord $c = 0.3$ m and a radius R =5 m with a root cutout of 1 m and it has an angle of attach equal to 6°. The rotor angular velocity is Ω =39.7 rad/s and the free stream advancing and vertical speed are equal to V_{∞_x} =15 m/s and V_{∞_z} =-1 m/s respectively. In this case there is no coupling with MBDyn and the blade pitch is kept constant. The reference solution is the one obtained with a full CFD Euler simulation carried out with ROSITA [126, 127], a compressible solver developed at Dipartimento di Scienze e Tecnologie Aerospaziali at Politecnico di Milano. ROSITA numerically integrates the RANS equations, in systems of moving, overset, multi-block grids. The adopted Chimera approach is derived from that originally proposed by Chesshire and Henshaw [128], with modifications to further improve robustness and performance. The governing equations are discretized in space by means of a cell-centred finite-volume implementation of the Roe scheme [129]. Time advancement is carried out with a dual-time formulation [130], employing a second order backward differentiation formula to approximate the time derivative and a fully unfactored implicit scheme in pseudo-time.

The first step is to compare the simulation results with a single blade rotating in an unperturbed flow field and hence without inflow. The total vertical force F_z generated by the blade over one revolution is shown in fig. 2.4. As it can be seen the two plots are very close and the slight difference could

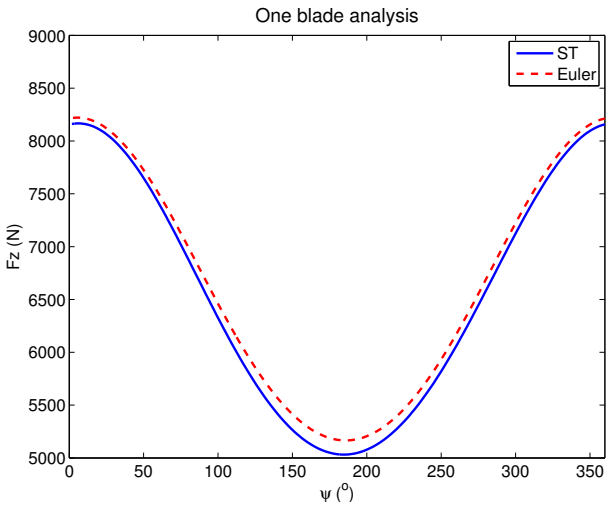

Figure 2.4: Root vertical force of the blade. Simulation with one blade.

be attributed to the differing volume discretizations.

After ensuring that the full potential aerodynamics of S^T provides good results, we proceed with the addition of the inflow model simulating up to the 5th harmonic. The results using four blades are reported in fig. 2.5. The comparison of the computed vertical force F_z of one blade in this case is very promising and shows the potentiality of our approach. It can be seen that the signal obtained by S^T reproduces the main features of the Euler simulation in what concerns the harmonic content. Even if the amplitudes predicted by S^T have a lower magnitude, this simple wake model coupled to a robust control design is able to provide a sufficient level of reliability that can be profitably used as an intermediate simulation tool for both the design and validation of controllers and aeroelastic simulations of rotors. A further investigation about the induced velocity distribution can be done through the Fourier analysis of the predicted inflow by the two methods. While the more complicated Euler simulation exhibits all the harmonic content from the 1/rev to the 8/rev, the inflow prediction with Peters-He has only a relevant peak for the 4/rev harmonic. Figures 2.6 and 2.7 compares the mean value and the magnitude of the 4/rev harmonic of the vertical induced velocity of the rotor for both of the codes. It can be seen that the shape of the computed inflow is very similar and the difference in the intensity, especially for the 4/rev harmonic, gives us the explanation of the underestimation of the blade root load harmonics of fig. 2.5b. It is also interesting to notice that the simulation time required to achieve such results is about 10 minutes for one rotor revolution (it depends on the mesh size) using 200 time steps and it is not even comparable with the computational cost of the ROSITA Euler simulation, which requires a highly parallelized algorithm. The details about the computational effort are summarized in tab. 2.1.

Although the comparison with the Euler solution shows satisfactory results, apart form a little shift in the mean value, the main differences, especially the ones related to the harmonics of the blade load, could be due to the presence of blade vortex interactions, which are not taken into account by our induced velocity model. To better evaluate the aerodynamic prediction of the presented hybrid approach, another simulation to decrease BVI effects is carried out by increasing the climbing rotor velocity up to V_{∞_z} =-5 m/s, so that the rotor wake is pushed down by the free stream velocity, while

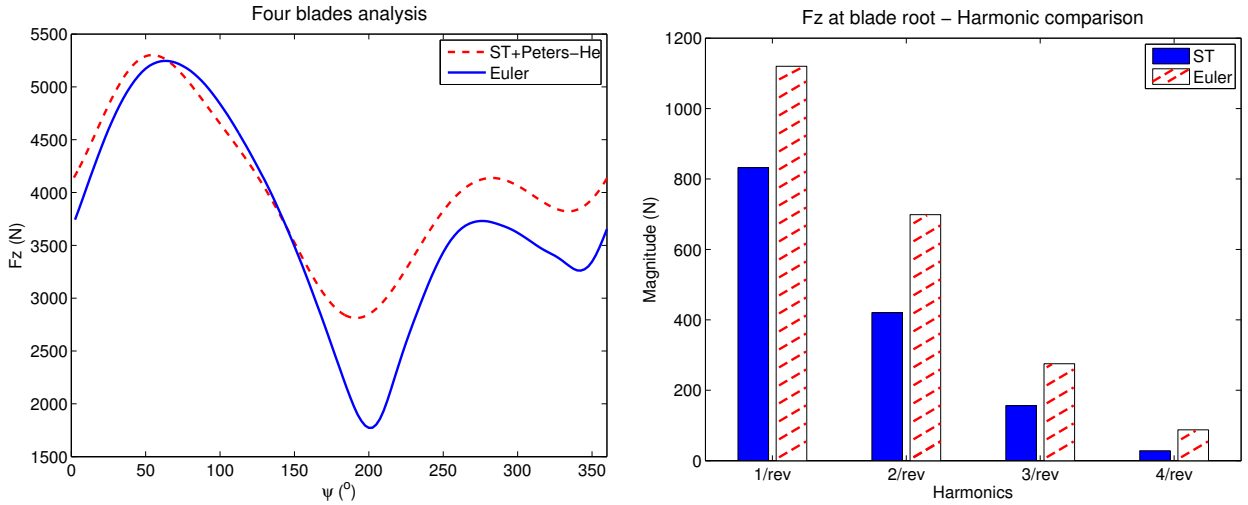

(a) Root vertical force of the blade. Simulation with four blades. V_{∞_x} =15 m/s and V_{∞_z} =-1 m/s.

(b) Fourier analysis of the force signal. V_{∞_x} =15 m/s and V_{∞_z} =-1 m/s.

Figure 2.5: Comparison with ROSITA.

Table 2.1: Computational details.

	#Cells	#Unknowns	#CPUs	Freq. CPU	CPUtime/rev
S^T	58 k	116 k	1	1.6 GHz	10 min
ROSITA	4.3 M	21.5 M	8	2.4 GHz	16 h

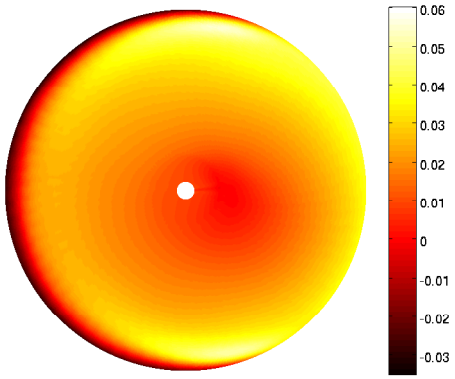

(a) Mean nondimensional inflow - Euler simulation.

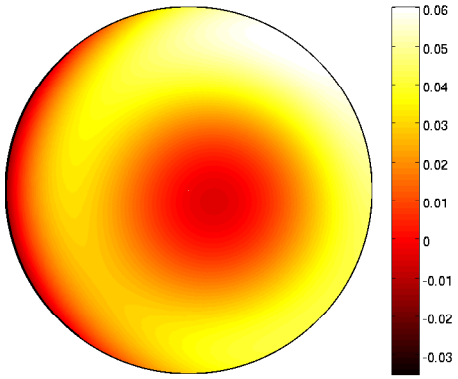

(b) Mean nondimensional inflow - Peters-He.

Figure 2.6: Comparison of the mean inflow over one rotor revolution.

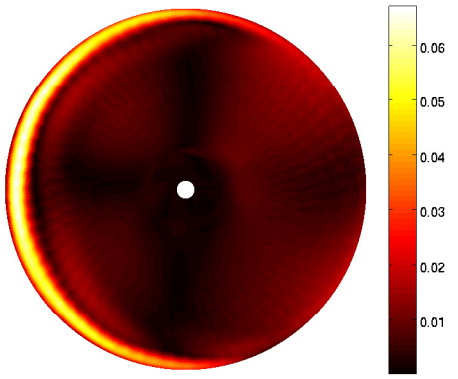

(a) 4/rev harmonic of the inflow - Euler simulation.

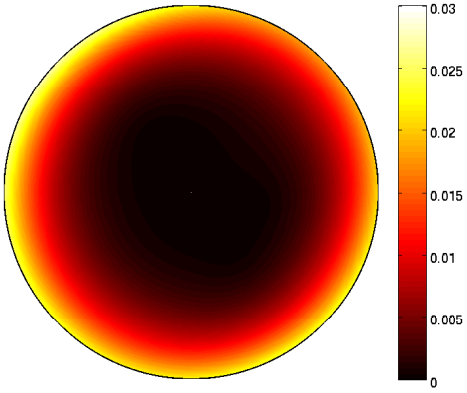

(b) 4/rev harmonic of the inflow - Peters-He.

Figure 2.7: Comparison of the nondimensional 4/rev harmonic of the induced velocity.

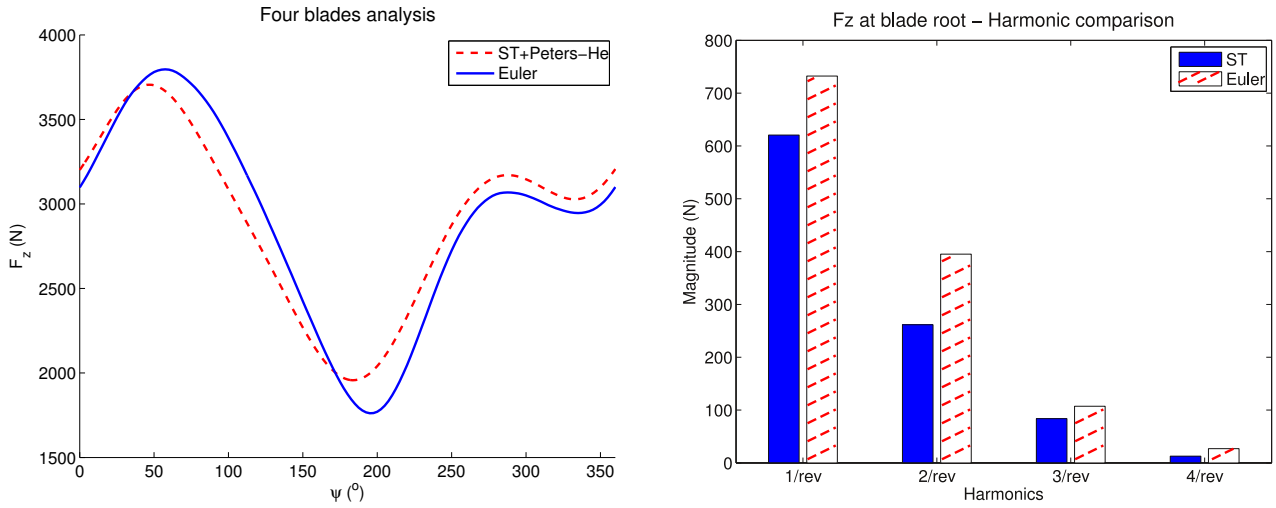

(a) Root vertical force of the blade. Simulation with four blades. V_{∞_x} =15 m/s and V_{∞_z} =-5 m/s.

(b) Fourier analysis of the force signal. V_{∞_x} =15 m/s and V_{∞_z} =-5 m/s.

Figure 2.8: Comparison with ROSITA.

Table 2.2: Mean value comparison - Root vertical force.

	S^T	*ROSITA*	Difference
V_z =-1 m/s	4057.7 N	3719.2 N	9.1 %
V_z =-5 m/s	2906.8 N	2895.2 N	0.4 %

leaving the other parameters unchanged. As it can be seen from the results of figs. 2.8a and 2.8b, the correlation of the blade root force harmonics with less BVI is improved and the whole amplitude of the force signal better approximates the one of the Euler computation. The mean values of the loads for both of the simulations are compared in tab. 2.2, showing that error on the mean value is correctly recovered in the second simulation where there is less influence of BVI effects.

To conclude the validation study of the proposed simulation code, it has been compared with the experimental data of the Hart II baseline trim condition [131]. Figure 2.9 confronts the experimental normal force coefficient C_nM^2, without the mean value, of the airfoil section at 87% of the radius R, with our hybrid CFD code and the two hybrid approaches described in [114]. In the first method the lifting line theory is combined with the free wake (FW) geometries of the tip vortices only, while in the second approach a more accurate and time consuming RANS-based CFD code is used for the near field aerodynamics of the blade and both the tip and root vortices are modeled to simulate the wake geometry. As can be seen in the figure, even if the Peters-He model is very simple and does not model the geometry of the wake it is still able to reproduce the main characteristics of the sectional load. In fact, while the trend of the low frequency behavior is followed quite correctly, the high frequency content of the normal force coefficient, which is due to the presence of the vortices released by the blades, cannot be approximated. In order to evaluate the mean value prediction of the hub

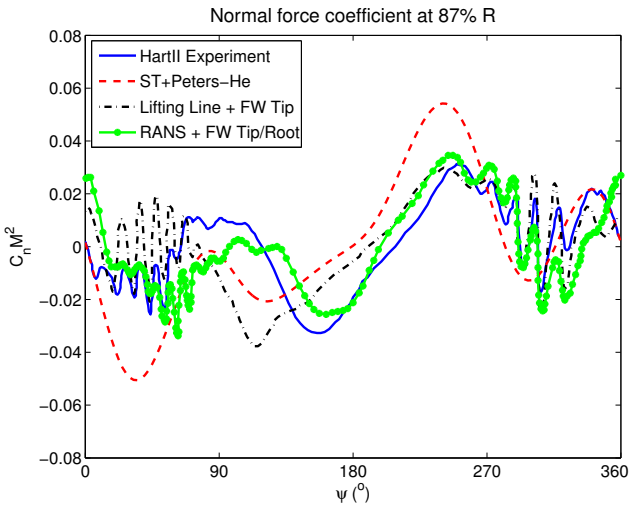

Figure 2.9: Hart II Baseline condition. Sectional normal force coefficient comparison with S^T and Peters-He.

loads, the trim angles of the swashplate used to achieve this forward flight configuration, are shown in fig. 2.13 together with the experimental data, the blade element theory combined with the dynamic inflow of MBDyn and the two hybrid method presented in [114]. While the cyclic cosine and sine angles predicted by our code are pretty close to the experimental ones and the prediction error is in agreement with the other simulation methods, the collective angle is a little bit overestimated and for this case it exceeds the experimental value by $0.7°$.

This validation study points out the strength and weakness of the proposed hybrid approach. Thanks to the full potential CFD method it is possible to correctly take into account the unsteadiness of the aerodynamic loads as well as compressibility effects, tip losses and an approximation of shock waves. This main limitations of this near field blade aerodynamics modeling is the impossibility to simulate both the static and dynamic stall, which could be very important in rotorcraft applications, and the fact that the potential solver cannot handle reverse flow conditions that occur in the blade root, mainly leading to an error in the hub mean forces prediction. The choice of a mathematical model for the induced velocity computation, as the Peters-He approach, helps to speed up the whole simulation, in contrast with more sophisticated free wake geometry methods, which are very time consuming. Although the Peters-He model increases the harmonic content of the induced velocity, with respect to linear inflow models, its main limitation is that BVI effects are not modeled. These effects are very important for a proper estimate of the $4/rev$ *harmonic of the vertical loads and are responsible for the higher frequency content of the airloads.*

2.2 Blade Element Method with Free Wake Geometry

In contrast to the previous hybrid CFD code, in this section the modeling of the blade near field aerodynamics is relaxed and the computational time is invested into the wake geometry representation. Therefore a free wake code is presented and coupled with MBDyn. The purpose of the development

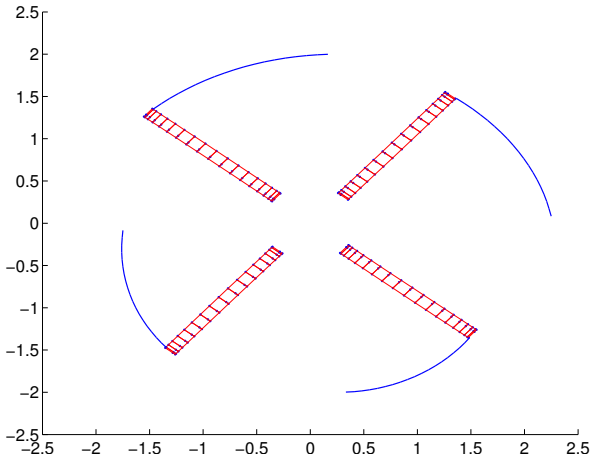

Figure 2.10: Free wake evolution.

of a more complex wake structure is demanded by the fact that an induced velocity model leads to an underestimation of the harmonic content of the resulting blade load, especially the $4/rev$ *one of the vertical force, as shown in the previous section. Another important advantage of representing the rotor wake is the consideration of BVI effects that have a great influences on the airloads. Being the numerical free wake analysis of all blades a quite time consuming task, the CFD approach to model the blade aerodynamics is abandoned and it has been decided to improve the classical and computationally faster blade element method instead. By doing so, it is possible to develop an aeroelastic code capable of providing a good level of accuracy about loads prediction with an affordable simulation time; a very important aspect when dealing with controller design and validation.*

2.2.1 Free Wake Code Description

The first step of this approach is the enhancement of the quasi-static blade element theory to simulate the near field aerodynamics of the blades. The blade span is divided into strips, with more elements at the blade root and tip, as shown in fig. 2.10, so that the user is able to define a tip loss factor with a higher level of accuracy by simply scaling the lift of the outer strips. The lift, drag and aerodynamic moment of the strip is computed through the data sheet for the C_L*,* C_D *and* C_M *coefficients that was used for the MBDyn simulations, thus taking into account the static stall and the compressibility effects thanks to the Prandtl-Glauert correction. While the classic blade element method considers the instantaneous aerodynamic angle of attach, in this work the effective angle of attach is corrected by accounting for unsteady effects. The unsteady effects are divided into two parts: the unsteady angle of attach related to the airfoil motion is computed by using both the Theodorsen lift deficiency function, but its variation due to the interaction between the blades and the tip vortices are better represented by the Kussner function, since they can be considered as gusts [132, 133].*

After having implemented an unsteady and fast blade element method for the blade loads computation, the second step is the generation of the rotor wake. To limit the computational burden, we decided to simulate only the tip vortices, which are the most relevant one and permit to consider the

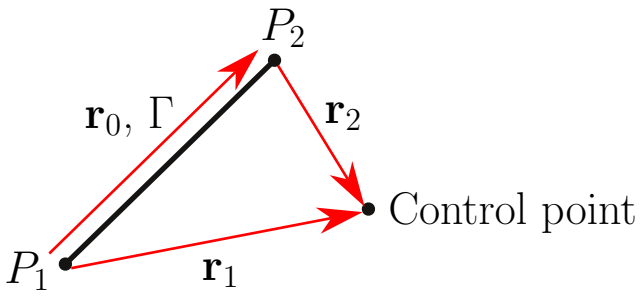

Figure 2.11: Vortex line element.

main effects of the rotor wake. At each time step a single vortex filament is released from the tip of each blade with a circulation Γ *that can be computed from the aerodynamic loads of the blade strips. After computing the loads of every blade element, it is possible to calculate the equivalent bound circulation through the Kutta-Jukovsky theorem and then the strength of the tip vortex that is going to be released at a given time step is set to the 80% of the maximum bound circulation of the blade outer portion, as suggested in the literature [134], with a dual-peak model in case of a negative load on the outer portion of the blade tip [135]. Another important model parameter, crucial for the proper estimation of the BVIs, is the size of the vortex core. Since we are only using the tip vortex to approximate the rotor wake, reproducing the physical size of the core vortex would overestimate the blade vortex interaction loads [136]. Therefore we assume that the blade tip vortex initial radius* r_0 *is overestimated and set equal to 50% of the blade chord [137]. In this free wake code the vortex aging follows Squire's law [138, 136] and the vortex core radius* r_c *becomes a function of the time and the initial core radius* r_0

$$r_c = \sqrt{r_0^2 + 4\sigma\delta\nu t}, \tag{2.17}$$

where σ *is a constant equal to* 1.25643, δ *is the vortex growth rate set to* 100 *in this work,* ν *is the kinematic viscosity and* t *is the simulation time that is related to the wake age. An example of the rotor wake evolution in the first steps of the simulation is reported in fig. 2.10. Since we modeled the unsteady aerodynamic effects and the tip loss function that approximate the main features of the near wake released by the blades, the far wake influence, represented by the tip vortices, is activated after* 30° *of rotor revolution in order not to duplicate the induced velocity contribution. The mutual induction among the trailing vortex filaments and the blade bound circulations are computed through the Biot-Savart law*

$$\mathbf{v}_{ind} = K_v \frac{\Gamma}{4\pi} \frac{\mathbf{r}_1 \times \mathbf{r}_2}{|\mathbf{r}_1 \times \mathbf{r}_2|^2} \left[\frac{\mathbf{r}_0 \cdot \mathbf{r}_1}{|\mathbf{r}_1|} - \frac{\mathbf{r}_0 \cdot \mathbf{r}_2}{|\mathbf{r}_2|} \right], \tag{2.18}$$

which gives the velocity induced by a vortex filament, defined by two points P_1 *and* P_2*, on a control point as shown in fig. 2.11. The factor* K_v *desingularizes the Biot-Savart equation when the evaluation point distance tends to zero and prevents a high induced velocity in the vicinity region of the vortex core radius. As suggested in [139], the velocity profile of the rotor tip vortices, in order to take into account the effect of a viscous vortex core can be modeled as*

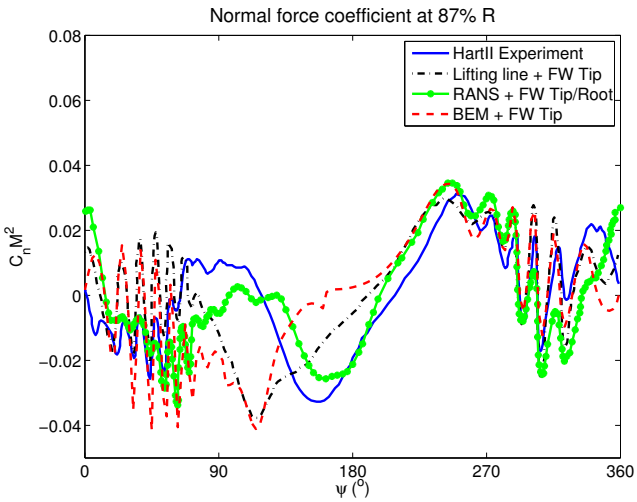

Figure 2.12: Hart II Baseline condition. Sectional normal force coefficient comparison with the free wake code.

$$K_v = \frac{h^2}{\sqrt{r_c^4 + h^4}}, \tag{2.19}$$

where h is defined as the perpendicular distance of the control point as

$$h = \frac{|\mathbf{r}_1 \times \mathbf{r}_2|}{l}. \tag{2.20}$$

The velocity of the points that form the vortex filaments, which is given by the mutual induction among the wake vortices and the bound circulations of the blades and the free stream velocity, is then integrated to update the position and the geometry of the wake at each time step.

The entire aerodynamic code is written in Matlab and therefore it is coupled with MBDyn exploiting the same elements discussed in the previous section. The multibody software sends to Matlab the position and the velocity of the blades structural nodes through the "external structural mapping" *element and receives the aerodynamic forces to be applied on the structural nodes. The communication is managed using the software mat py.*

2.2.2 Model Validation

To assess the quality of the aerodynamic approximation provided by the developed free wake code , it has been validated with the experimental data of the Hart II baseline trim condition [131] and other results presented in the literature, as done for the full potential hybrid code presented in the previous section. The normal force coefficient of the section at 87%R over one rotor revolution is compared in fig. 2.12 and permits to evaluate the BVI prediction and the loads estimation capabilities of the code. The normal force coefficient predicted by this hybrid free wake approach (BEM + FW Tip in the figure) is very close to the one obtained with the lifting line theory with only the free wake of tip vortex and it is able to predict the position of the BVI. However, both of the codes overestimate the BVI

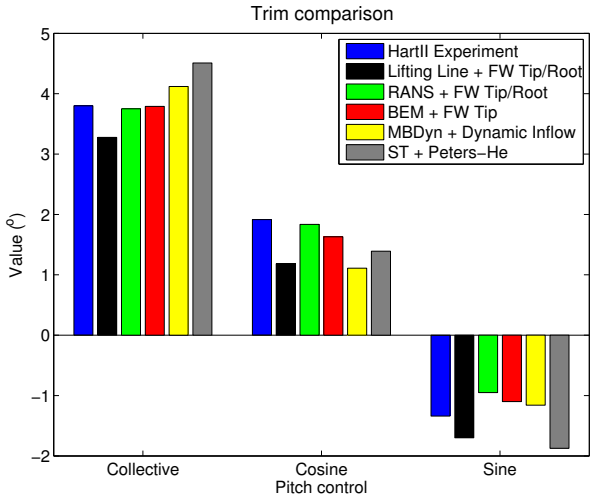

Figure 2.13: Hart II Baseline trim comparison.

peaks. It can be seen that by adding the root vortices, thus increasing the computational cost, the BVI peaks are reduced to acceptable levels and the low frequency content of the normal force coefficient is better approximated. The comparison of the swashplate angles to reach the desired trim condition is given in fig. 2.13. As can be seen in the figure, the trim angles are very close to the experimental data and comparable with the more complex and time consuming hybrid method of [114] using a RANS equation solver and the free wake of both the blade tip and root vortices.

The comparison between our free wake code and the experimental data shows the improvements of the proposed hybrid code. It is possible to obtain very satisfactory results and accurate loads prediction with a reasonable simulation time, which vary with respect to the growing wake. The improved blade element method for the near field aerodynamic representation is not computationally expensive and is stable in all flow conditions, because of the tabular force coefficients structure. Even if the static stall is considered, this approach does not comprise the dynamic stall and the tip losses have to be adjusted every time a new simulation is required. In this case shock waves cannot be simulated. The wake modeling increases the airloads prediction capabilities and the influence of the vortices on the blades are well approximated, giving a good approximation of the induced velocity field that is observed in the trim analysis. The limits of the free wake approach are given by the fact that there is not a general rule to tune some simulation parameters, such as the vortex core radius and aging, the quantity of the bound vorticity released at each time step and the position of the released tip vortex. Although the main characteristics of the inflow are reproduced by the tip vortices only, the introduction of the root vortices would provide a more sophisticated and accurate solution.

Part II

Control Systems Design

Chapter 3

Periodic Controllers

The rotor subsystem in forward flight exhibits a nonlinear and complex behavior, in what concerns both the structural dynamics of the blades and the dissimilar aerodynamic field. It limits the possibility to achieve satisfactory performance through linearized time invariant controller theories. In particular the periodicity of the dynamical system plays an important role and more sophisticated solutions to design a vibration controller taking into account this issue can be found by exploiting the periodic control theory. Even if such controllers are linear and require a linearization of the controlled system, they achieve good performance because the periodicity is properly accounted. Several works about helicopter control that considers the periodicity of the system can be found in the literature. A model following approach to stabilize lag and pitch moments using periodic control is proposed in [140]. Periodic vibration controllers can be found in [141, 142], where the baseline loads alleviation by means of IBC is considered as a disturbance rejection problem. Active twist flaps are used in [143] to reduce hub loads by a dynamic compensator arising from the periodic H_2 and H_∞ design.

In this chapter we start from a review of the periodic H_2 design and of the periodic output feedback (POF) technique to reduce hub loads as shown in [144, 145]. The two solutions are then compared and it is shown that satisfactory results can be achieved by using the static POF approach, which represents an advantage in terms of the computational cost for its design and for the simplicity of the control law that can be profitably used for scheduling purposes. The last part of the work investigates the robustness of the two controllers. The aim is to show that even if a simple design model is used in the design phase of the periodic vibration controllers, it is still possible to predict satisfactory loads reduction when a more complex numerical model, that better approximates the real rotor behavior, is used.

3.1 Periodic System Identification

The design of a linear periodic controller requires a previous knowledge of the the process behavior and hence the estimate of a linearized periodic state space model of the system to be controlled. Dealing with a helicopter in forward flight, the system is obviously periodic, and this has to be taken into account while identifying the model. Classical identification procedures for linear time invariant (LTI) systems cannot be used for periodic systems; thus, a periodic subspace identification algorithm

[146] is used to find a linear discrete-time periodic (LTP) model of the blade in the form

$$\begin{aligned} \mathbf{x}_{k+1} &= \mathbf{A}_k \mathbf{x}_k + \mathbf{B}_k u_k \\ y_k &= \mathbf{C}_k \mathbf{x}_k + \mathbf{D}_k u_k \end{aligned} \tag{3.1}$$

where the system matrices have period N. Without loss of generalization, external disturbances are here not not cconsidered because we are working with simulations, but in case of practical tests this formulation can still be valid because it is possible to filter the disturbances through low-pass filters.

After collecting the required input/output time histories signals from numerical simulations, they are organized in input/output Hankel matrices $\mathbf{U}_{k,s}$ *and* $\mathbf{Y}_{k,s}$ *for* $k = 1...N$ *as follows*

$$\mathbf{U}_{k,s} = \begin{bmatrix} u_k & u_{k+1} & \cdots & u_{k+s-1} \\ u_{N+k} & u_{N+k+1} & \cdots & \vdots \\ \vdots & & \cdots & \vdots \\ u_{(n-1)N+k} & & \cdots & u_{(n-1)N+k+s-1} \end{bmatrix} \tag{3.2}$$

$$\mathbf{Y}_{k,s} = \begin{bmatrix} y_k & y_{k+1} & \cdots & y_{k+s-1} \\ y_{N+k} & y_{N+k+1} & \cdots & \vdots \\ \vdots & & \cdots & \vdots \\ y_{(n-1)N+k} & & \cdots & y_{(n-1)N+k+s-1} \end{bmatrix} \tag{3.3}$$

where N is the period, n is the total number of simulations and s is the length of each experiment. Here the Hankel matrices are computed using a single numerical simulation. Considering the QR factorization of the compound square matrices

$$\begin{bmatrix} \mathbf{U}_{k,s} & \mathbf{Y}_{k,s} \end{bmatrix} = \begin{bmatrix} \mathbf{Q}_{1_k} & \mathbf{Q}_{2_k} \end{bmatrix} \begin{bmatrix} \mathbf{R}_{11_k} & \mathbf{R}_{12_k} \\ \mathbf{R}_{21_k} & \mathbf{R}_{22_k} \end{bmatrix} \tag{3.4}$$

the observability matrix $\mathbf{O}_k$ *is given by the row space of matrix* $\mathbf{R}_{22_k}$ *and can be computed through its singular value decomposition (SVD)*

$$\mathbf{R}_{22_k} = \mathbf{U}_k \Sigma_k \mathbf{V}_k^T \tag{3.5}$$

$$\mathbf{O}_k = \tilde{\mathbf{V}}_k^T \tag{3.6}$$

The order of the identified system is chosen according to the magnitude of the singular values of Σ_k *and then the observability matrix is computed as* $\tilde{\mathbf{V}}_k^T$*, which contains the first rows and columns of* $\mathbf{V}_k^T$ *up to the defined system order. Afterwards, the matrices* $\mathbf{A}_k$ *and* $\mathbf{C}_k$ *can be obtained by exploiting the observability matrix at the instants* $k+1$ *and k, see [146, 143] for details. The periodicity is imposed by setting* $\mathbf{O}_{N+1} = \mathbf{O}_1$.

An output error approach is used for the identification of the matrices $\mathbf{B}_k$ *and* $\mathbf{D}_k$*, which are computed through the minimization of the squared 2-norm error between the real and the model output,* y_{real} *and y respectively:*

$$\min_{\mathbf{B}_k, \mathbf{D}_k} \| y_{real} - y \|_2^2 . \tag{3.7}$$

After identifying the linearized blade model, performance specifications and model disturbances have to be introduced in the generalized plant. The block diagram of the complete design model is

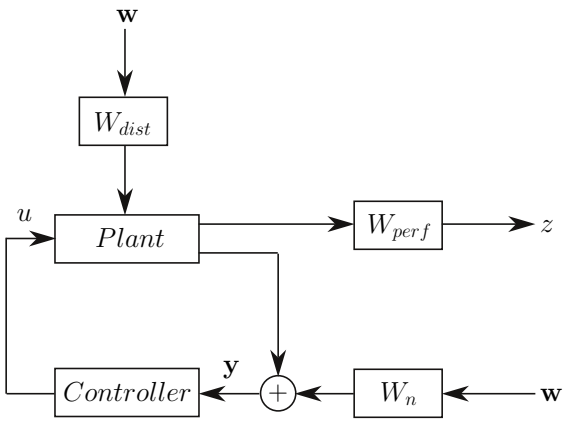

Figure 3.1: Generalized plant.

shown in fig. 3.1 where **z** *are the controlled outputs. We want to minimize the blade root shear force* F_z*,* **y** *are the measures,* **w** *are white noise disturbances and u the control signal. The shaping filters* W_{dist} *models the baseline loads, which are now reintroduced as output disturbances of the system. While the sensors noise is modeled with white noises having a constant amplitude* W_n*, the performance of the controller are defined by means of the hand-tuned frequency weighting function* W_{perf} *to impose the proper reduction of the harmonics of the blade root load* F_z*; it is adjusted in the controller design phase to obtain the best vibration reduction. The resulting generalized plant model including possible weight dynamics is then described with the following linear periodic model*

$$\begin{aligned} \mathbf{x}_{k+1} &= \mathbf{A}_k\mathbf{x}_k + \mathbf{B}_{1_k}\mathbf{w}_k + \mathbf{B}_{2_k}u_k, \\ \mathbf{z}_k &= \mathbf{C}_{1_k}\mathbf{x}_k + \mathbf{D}_{11_k}\mathbf{w}_k + \mathbf{D}_{12_k}u_k, \\ \mathbf{y}_k &= \mathbf{C}_{2_k}\mathbf{x}_k + \mathbf{D}_{21_k}\mathbf{w}_k + \mathbf{D}_{22_k}u_k. \end{aligned} \tag{3.8}$$

3.2 H_2 Periodic Controller

This section describes the design of the optimal H_2 *controller, that stabilizes the system and minimizes the* H_2 *norm of the transfer function between the plant disturbance and the desired performance. Starting from the identified generalized plant model a dynamic output feedback controller can be found by solving two Discrete Time Periodic Riccati Equations (DTPRE) [147] corresponding to the filtering and the state feedback control problem:*

$$\begin{aligned} \mathbf{Q}_{k+1} &= \mathbf{A}_k\mathbf{Q}_kA_k^T + \mathbf{B}_{1_k}\mathbf{B}_{1k}^T - \left(\mathbf{A}_k\mathbf{Q}_k\mathbf{C}_{2_k}^T + \mathbf{B}_{1_k}\mathbf{D}_{21_k}^T\right) \\ &\quad + \left(\mathbf{D}_{21_k}\mathbf{D}_{21_k}^T + \mathbf{C}_{2_k}\mathbf{Q}_k\mathbf{C}_{2_k}^T\right)^{-1}\left(\mathbf{A}_k\mathbf{Q}_k\mathbf{C}_{2_k}^T + \mathbf{B}_{1_k}\mathbf{D}_{21_k}^T\right), \end{aligned} \tag{3.9}$$

$$\begin{aligned} \mathbf{P}_k &= \mathbf{A}_k^T\mathbf{P}_{k+1}\mathbf{A}_k + \mathbf{C}_{1_k}^T\mathbf{C}_{1_k} - \left(\mathbf{A}_k^T\mathbf{P}_{k+1}\mathbf{B}_{2_k} + \mathbf{C}_{1_k}^T\mathbf{D}_{12_k}\right) \\ &\quad + \left(\mathbf{D}_{12_k}^T\mathbf{D}_{12_k} + \mathbf{B}_{2_k}^T\mathbf{P}_{k+1}\mathbf{B}_{2_k}\right)^{-1}\left(\mathbf{A}_k^T\mathbf{P}_{k+1}\mathbf{B}_{2_k} + \mathbf{C}_{1_k}^T\mathbf{D}_{12_k}\right). \end{aligned} \tag{3.10}$$

A cyclic QZ decomposition method is used, as described in [148, 149], for the solution of eqs. 3.9 and 3.10. Once the solutions of the Riccati equations have been obtained, the periodic control system can be easily defined by [147, 143]

$$\begin{aligned} \xi_{k+1} &= \mathbf{A}_k^C \xi_k + \mathbf{B}_k^C y_k, \\ u_k &= \mathbf{C}_k^C \xi_k + \mathbf{D}_k^C y_k. \end{aligned} \tag{3.11}$$

The the controller matrices $\mathbf{A}_k^C$, $\mathbf{B}_k^C$, $\mathbf{C}_k^C$ and $\mathbf{D}_k^C$ of eqs. 3.11 can be computed by following the procedure outlined in [143] as described in [144]. It can be derived by the filtering and control theory in H_2 described in [147] by combining the observer and the full information state feedback control. After solving the two periodic Riccati equations 3.9 and 3.10, the sought matrices are given by

$$\mathbf{A}_k^C = \mathbf{A}_k - \mathbf{L}_k \mathbf{C}_{2_k} + \mathbf{B}_{2_k} \mathbf{K}_k - \mathbf{B}_{2_k} \mathbf{L}_k^O \mathbf{C}_{2_k}, \tag{3.12}$$

$$\mathbf{B}_k^C = \mathbf{L}_k + \mathbf{B}_{2_k} \mathbf{L}_k^O, \tag{3.13}$$

$$\mathbf{C}_k^C = \mathbf{K}_k - \mathbf{L}_k^O \mathbf{C}_{2_k}, \tag{3.14}$$

$$\mathbf{D}_k^C = \mathbf{L}_k^O, \tag{3.15}$$

where

$$\mathbf{L}_k = \left(\mathbf{A}_k \mathbf{Q}_k \mathbf{C}_{2_k}^T + \mathbf{B}_{1_k} \mathbf{D}_{21_k}^T\right) \left(\mathbf{C}_{2_k} \mathbf{Q}_k \mathbf{C}_{2_k}^T + \mathbf{D}_{21_k} \mathbf{D}_{21_k}^T\right)^{-1}, \tag{3.16}$$

$$\mathbf{L}_k^O = \left(\mathbf{K}_k \mathbf{Q}_k \mathbf{C}_{2_k}^T + \mathbf{W}_k \mathbf{D}_{21_k}^T\right) \left(\mathbf{C}_{2_k} \mathbf{Q}_k \mathbf{C}_{2_k}^T + \mathbf{D}_{21_k} \mathbf{D}_{21_k}^T\right)^{-1}, \tag{3.17}$$

$$\mathbf{K}_k = -\left(\mathbf{B}_{2_k}^T \mathbf{P}_{k+1} \mathbf{B}_{2_k} + \mathbf{D}_{12_k}^T \mathbf{D}_{12_k}\right)^{-1} \left(\mathbf{B}_{2_k}^T \mathbf{P}_{k+1} \mathbf{A}_k + \mathbf{D}_{12_k}^T \mathbf{C}_{1_k}\right) \tag{3.18}$$

and

$$\mathbf{W}_k = -\left(\mathbf{B}_{2_k}^T \mathbf{P}_{k+1} \mathbf{B}_{2_k} + \mathbf{D}_{12_k}^T \mathbf{D}_{12_k}\right)^{-1} \left(\mathbf{B}_{2_k}^T \mathbf{P}_{k+1} \mathbf{B}_{1_k} + \mathbf{D}_{12_k}^T \mathbf{D}_{11_k}\right). \tag{3.19}$$

Should matrix $\mathbf{D}_{22_k}$ be non null, i.e. should direct feedthrough be present, then the matrices would have to be modified into [150]

$$\tilde{\mathbf{A}}_k^C = \mathbf{A}_k^C - \mathbf{B}_k^C \mathbf{D}_{22_k} \mathbf{T}_k^{-1} \mathbf{C}_k^C, \tag{3.20}$$

$$\tilde{\mathbf{B}}_k^C = \mathbf{B}_k^C - \mathbf{B}_k^C \mathbf{D}_{22_k} \mathbf{T}_k^{-1} \mathbf{D}_k^C, \tag{3.21}$$

$$\tilde{\mathbf{C}}_k^C = \mathbf{T}_k^{-1} \mathbf{C}_k^C, \tag{3.22}$$

$$\tilde{\mathbf{D}}_k^C = \mathbf{T}_k^{-1} \mathbf{D}_k^C, \tag{3.23}$$

where

$$\mathbf{T}_k = \mathbf{D}_k^C \mathbf{D}_{22_k} + \mathbf{I} \tag{3.24}$$

and $\mathbf{I}$ is the identity matrix.

The order of the controller is the same as the order of the generalized plant of eq. 3.8 and it depends on the selected frequency weighting functions and shaping filters for performance specification and the disturbance modeling. The dynamic compensator structure is here necessary because the system state is not available and have to be reconstructed by the controller, in the next approach a direct output feedback controller, which does not require any knowledge of the system state, is presented.

3.3 Periodic Output Feedback Controller

The second approach analyzed in this work consists in the design of a periodic output feedback (POF) static controller, where the control law is a direct feedback relationship of the sensors measures of the form

$$u_k = \mathbf{K}_k \mathbf{y}_k,$$

where the gain matrix $\mathbf{K}_k$ can either be periodic with period N or a constant matrix equal for all sample times. Assuming that there is no direct feedthrough in the system response, i. e. matrix $\mathbf{D}_{22_k} = \mathbf{0}$ in eqs. 3.1 and 3.8, the periodic output feedback (POF) control law is obtained by minimizing the quadratic performance index

$$J = E\left[\sum_{k=0}^{\infty}\left(\mathbf{z}_k^T \mathbf{Q}_k \mathbf{z}_k + \mathbf{u}_k^T \mathbf{R}_k \mathbf{u}_k\right)\right], \tag{3.25}$$

where $\mathbf{Q}_k$ and $\mathbf{R}_k$ are symmetric periodic user defined weighting matrices. In the general case no closed form solutions can be found to this problem and a design solution must be found by resorting to a numerical optimization procedure. The problem can be reformulated, as explained in [151], as

$$J(\mathscr{K}) = tr(\sigma\mathscr{P}\mathscr{G}), \tag{3.26}$$

$$\nabla_{\mathscr{K}} J(\mathscr{K}) = 2(\mathscr{R}\mathscr{K}\mathscr{C}_2 + \mathscr{B}_2^T \sigma\mathscr{P}\overline{\mathscr{A}})\mathscr{S}\mathscr{C}_2^T, \tag{3.27}$$

where the gradient of the cost function is provided as well since efficient optimization algorithms require it. The script notation $\mathscr{X}$ indicates the block diagonal matrix $\mathscr{X} = diag(\mathbf{X}_1, \ldots, \mathbf{X}_N)$ related to the cyclic sequence of the periodic matrix $\mathbf{X}_k$; the notation $\sigma\mathscr{X}$ denotes the K-cyclic shift $\sigma\mathscr{X} = diag(\mathbf{X}_2, \ldots, \mathbf{X}_N, \mathbf{X}_1)$. Matrices $\mathscr{P}$ and $\mathscr{S}$ satisfy the Discrete Periodic Lyapounov Equations (DPLEs)

$$\mathscr{P} = \overline{\mathscr{A}}^T \sigma\mathscr{P}\overline{\mathscr{A}} + \overline{\mathscr{Q}} \tag{3.28}$$

and

$$\sigma\mathscr{S} = \overline{\mathscr{A}}\mathscr{S}\overline{\mathscr{A}}^T + \mathscr{G} \tag{3.29}$$

respectively, where $\overline{\mathscr{A}} = \mathscr{A} + \mathscr{B}_2\mathscr{K}\mathscr{C}_2$ is the closed loop matrix and $\overline{\mathscr{Q}} = \mathscr{Q} + \mathscr{C}_2^T\mathscr{K}^T\mathscr{R}\mathscr{K}\mathscr{C}_2$. Matrix $\mathscr{G}$ is defined as $\mathscr{G} = diag(0, \ldots, 0, \mathbf{X}_0)$, where $\mathbf{X}_0$ represents the influence of initial conditions and disturbances on the state dynamics defined as $\mathbf{X}_0 = E\left[\overline{\mathbf{x}}_0\overline{\mathbf{x}}_0^T\right]$. In the closed loop system the perturbed initial conditions are $\overline{\mathbf{x}}_0 = \mathbf{x}_0 + (\mathbf{B}_{1_N} + \mathbf{B}_{2_N}\mathbf{K}_N\mathbf{D}_{21_N})\mathbf{w}$ and assuming null cross-correlation between the initial conditions $\mathbf{x}_0$ ad the disturbances $\mathbf{w}$, i.e. $E\left[\mathbf{x}_0\mathbf{w}^T\right] = 0$, the matrix $\mathbf{X}_0$ is given by $\mathbf{X}_0 = E\left\{\mathbf{x}_0\mathbf{x}_0^T\right\} + \mathbf{B}_{1_N}E\left\{\mathbf{w}\mathbf{w}^T\right\}\mathbf{B}_{1_N}^T + \mathbf{B}_{2_N}\mathbf{K}_N\mathbf{D}_{21_N}E\left\{\mathbf{w}\mathbf{w}^T\right\}\mathbf{B}_{1_N}^T + \mathbf{B}_{1_N}E\left\{\mathbf{w}\mathbf{w}^T\right\}\mathbf{D}_{21_N}^T\mathbf{K}_N^T\mathbf{B}_{2_N}^T$ $+\mathbf{B}_{2_N}\mathbf{K}_N\mathbf{D}_{21_N}E\left\{\mathbf{w}\mathbf{w}^T\right\}\mathbf{D}_{21_N}^T\mathbf{K}_N^T\mathbf{B}_{2_N}^T$ (The variance matrices are here approximated as identity matrices).

An important issue that has to be solved at each iteration of the optimization procedure, is the solution of the Reverse-Time Discrete Periodic Lyapounov Equation (RTDPLE) 3.28 and the Forward-Time Discrete Periodic Lyapounov Equation (FTDPLE) 3.29, whose solution algorithms are detailed in [151, 152]. If the monodromy matrix $\Phi_A(N)$ of the dynamical system has no reciprocal eigenvalues, then it is possible to use a very simple solution method, based on reducing these problem to a single Lyapounov equation to compute a periodic generator. These equations can be solved by using standard methods. The rest of the solution is computed by backward- or forward-time recursion. This method is briefly described below for both equations.

- *Solution of the RTDPLE: The periodic generator can be computed through the solution of the following discrete Lyapounov equation (DLE)*

$$\mathbf{P}_1 = \Phi_A^T(N)\mathbf{P}_1\Phi_A(N) + \sum_{j=1}^{N} \Phi_A^T(j,1)\overline{\mathbf{Q}}_j\Phi_A(j,1),$$

where $\Phi_A(j,i)$ is the transition matrix and the backward-time recursion is given by

$$\mathbf{P}_{N-i} = \overline{\mathbf{A}}_{N-i}^T\mathbf{P}_{N+1-i}\overline{\mathbf{A}}_{N-i} + \overline{\mathbf{Q}}_{N-i} \qquad i = 0,\ldots,N-2$$

- *Solution of the FTDPLE: The periodic generator can be computed through the solution of the following DLE*

$$\mathbf{S}_1 = \Phi_A(N)\mathbf{S}_1\Phi_A^T(N) + \sum_{j=1}^{N} \Phi_A(N+1,j+1)\mathbf{G}_j\Phi_A^T(N+1,j+1);$$

the forward-time recursion is given by

$$\mathbf{S}_i = \overline{\mathbf{A}}_{i-1}\mathbf{S}_{i-1}\overline{\mathbf{A}}_{i-1}^T + \mathbf{G}_{i-1} \qquad i = 2,\ldots,N.$$

3.4 Simulation Results

3.4.1 Controllers Design

The periodic controller are designed and tested on the trim configuration having the advancing parameter equal to $\mu = 0.23$. The design model is based on the low fidelity aerodynamic theory provided by MBDyn, thus allowing to tune the controllers with a reasonable computational effort. The interference among the actuation of one blade and the forces on other blades is almost null due to the very simple aerodynamic model. Therefore, each blade is considered independent and the IBC controller is designed considering only a single blade. We are interested into the linearized input/output relation between the voltage V applied on the blade and the blade sensors measures. In order to well represent the blade response, we chose to measure the blade root shear force F_z and five vertical accelerations at locations uniformly distributed along the blade span.

The periodic load and the accelerations on the blade of the reference trimmed configuration are saved; they will be subsequently subtracted to the excited response signals to linearize the system around the trimmed configuration. The blade are excited with a random voltage with an amplitude of 40 V filtered above $6/rev$ so to limit higher harmonics in the dynamic response. Being the Bo105 a four blades rotor, the most important harmonics for the vibratory hub loads are the $3/rev$ and the $4/rev$ and all output signals have been filtered before the identification to consider only those harmonics, hence reducing the size of the state space model. The controllers should minimize the $4/rev$ harmonic of the blade root shear force F_z to reduce the hub vertical force and reduce the $3/rev$ harmonic as well to alleviate the vibratory loads associated to the moments of the blade root loads. The aeroelastic multibody simulation requires a small integration time step; the simulations are performed with $N = 140$ time steps for every rotor revolution. The direct identification of such signals will lead to the computation of 140 linear systems spanning the period. Since we want to reduce the computational

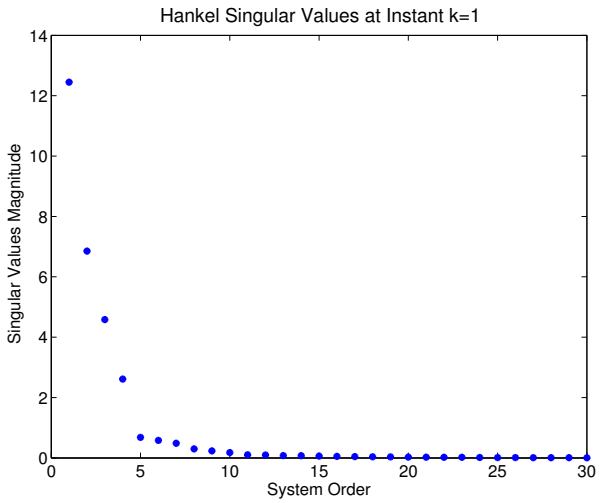

Figure 3.2: System order.

burden of both the identification and the controller design, we decimated the system outputs to $N = 28$ *time steps per rotor revolution, still approximating the outputs required for the identification with a good level of accuracy. Hints about the order of the identified system can be found by analyzing the singular value magnitudes of the matrix* $\mathbf{R}_{22_k}$ *at each time step. The best compromise between data fitting and system order is given by retaining the most important singular values. For example, fig. 3.2 shows the singular values computed for the first time step. Based on the singular values, the chosen linear periodic model of the blade is a* $14th$ *order system for every time step spanning the period.*

Being the design model identified, the generalized plant is built and model disturbances as well as performance specifications are modeled. While the white noise amplitude of the sensors noise is assumed to have a value of $W_n = 0.1$*, the baseline loads are reintroduced as output disturbances by the shaping filters* W_{dist} *for all the measure channels and fig. 3.3 shows for simplicity only the baseline tip acceleration. The frequency weighting function to impose the performance of the controller output,* F_z*, is tuned through several simulations so to have the optimize the controller effectiveness and the selected functions for both the* H_2 *controller and the POF one are reported in figs. 3.4a and 3.4b. The performance weighting matrix* $\mathbf{Q}_k$ *of the POF cost function J of eq. 3.25 is the identity matrix, because the performance specifications have been taken into account by* W_{perf}*, and is kept constant for the whole period, while the other weight matrix is* $\mathbf{R}_k$*, which prescribes further limitation for the control signal, is tuned until satisfactory loads reduction is achieved and in this example it has a value of* 5000*. The design of this controller is faster than the* H_2 *one because of the less number of parameters involved in the optimization and due to the more efficiency in the solution of the two DPLEs in contrast to the solution of the DTPREs [149].*

Closed loop simulations are carried out by coupling MBDyn and Simulink; since the multibody simulation and the controller have been designed using different sample times, Simulink Rate-Transition blocks are used to implement a sample and hold procedure, thus overcoming this issue. The results of the vibration reduction achieved by the periodic controllers are summarized in fig. 3.5, which shows the magnitude of the hub load harmonics with and without control. Although a significant passive load reduction is obtained by simply replacing the Bo105 blades with the piezoelectric

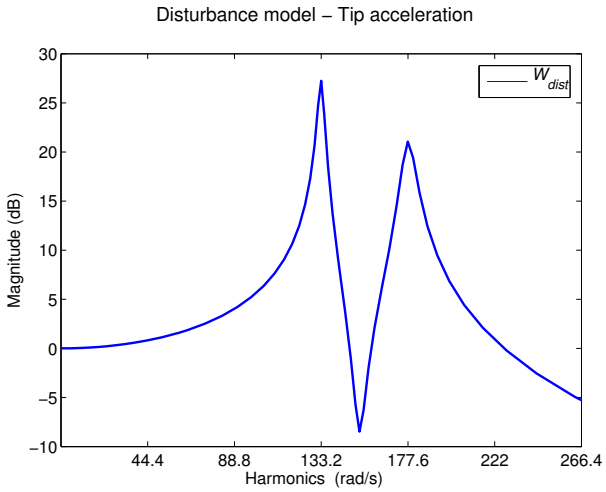

Figure 3.3: Baseline tip acceleration.

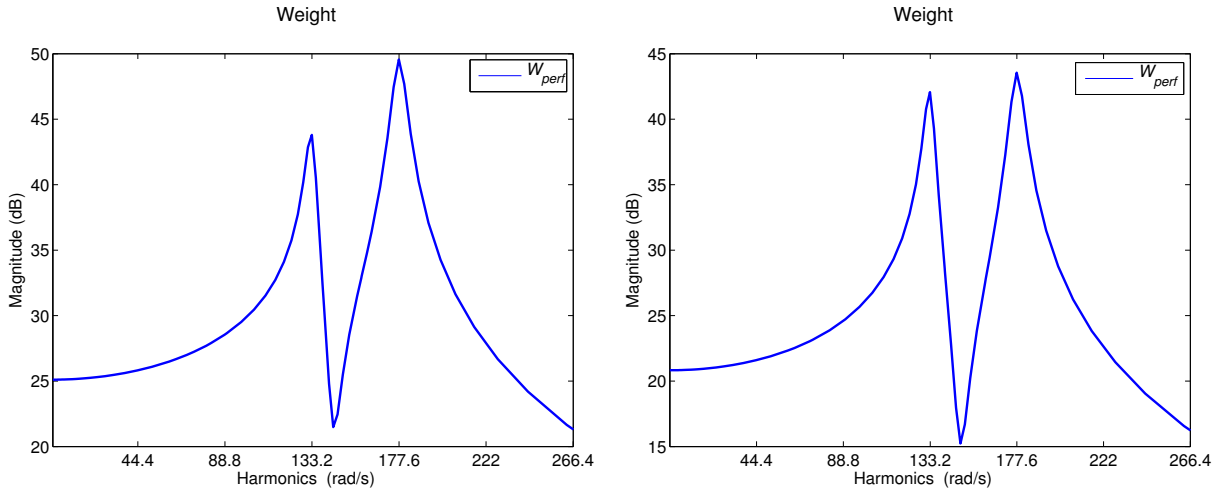

(a) W_{perf} - H_2Control

(b) W_{perf} - POF Control

Figure 3.4: Controller performance specifications

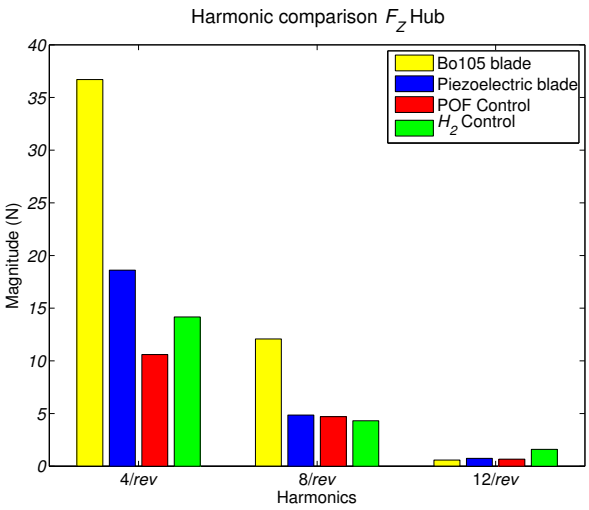

(a) Hub vertical force F_Z.

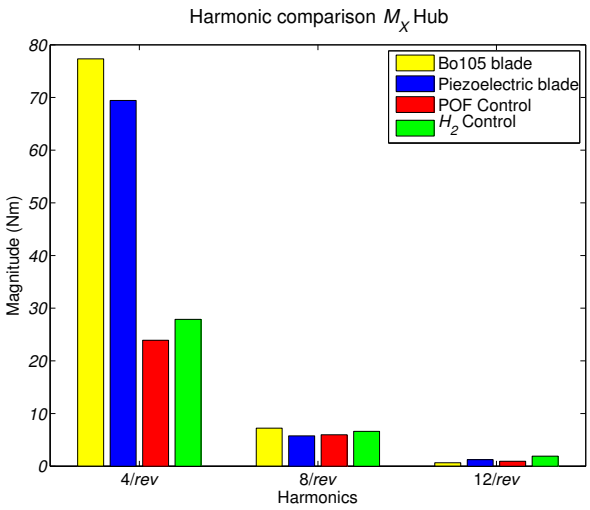

(b) Hub moment M_X.

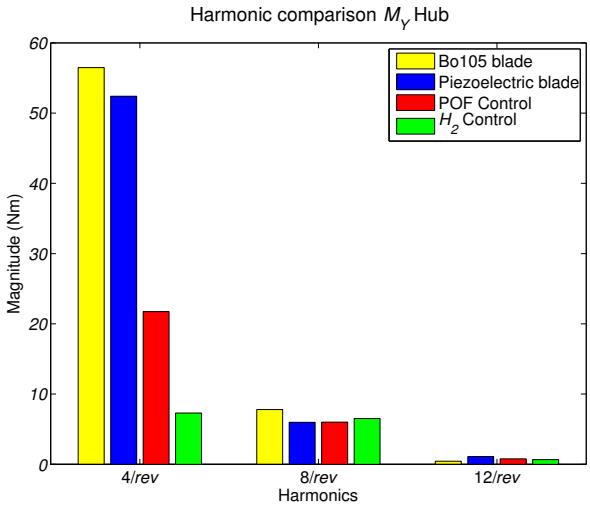

(c) Hub moment M_Y.

Figure 3.5: Vibrations reduction on the design model.

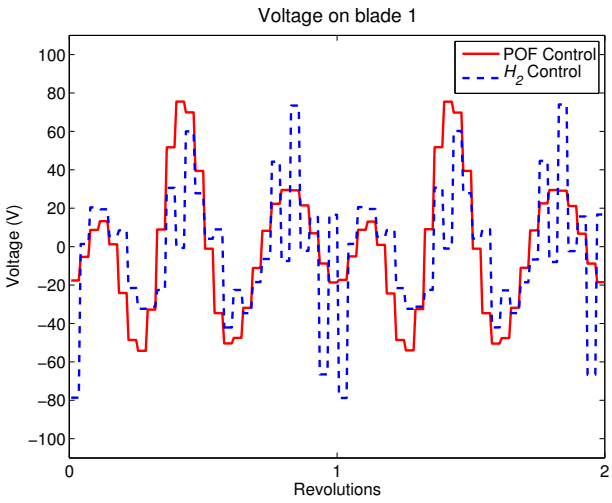

Figure 3.6: Applied voltage on blade 1.

ones,the closed loop simulations with both controllers allow to further alleviate the hub loads. The $4/rev$ *harmonic of the hub force and moments* F_Z*,* M_X *and* M_Y *is reduced through the* H_2 *controller by* 24% *,* 60% *and* 86% *respectively. The static output feedback controller allows a reduction of* 43%*,* 65% *and* 58%*. Note that both of the active solutions are satisfactory, with comparable performances. The* H_2 *has a better capability to reduce the moment* M_Y*, while the direct output feedback approach better alleviates the force* F_Z*. On the average, the simpler static output feedback controller can be a valid substitute of the* H_2 *controller dynamic compensator, in spite of its faster algorithm and fewer design parameters. Note also that higher than the* $4/rev$ *harmonics are only marginally excited. The applied voltage on the first blade is shown in fig. 3.6. The control signal is a sequence of steps because of controller sampling time. The control effort remains quite low, and doesn't exceed* 80 V *in both simulations. Note also that the control voltage computed by the static output feedback control has a lower frequency content than that of the* H_2 *dynamic compensator; this may lead to better robustness properties, since it does not excite high harmonics that may not have been considered in the controller design phase.*

3.4.2 Controllers Validation

In this section the periodic controllers designed using the simple aerodynamic model are adopted to reduce the loads predicted by the model coupled with the free-wake code to evaluate their robustness. Figure 3.7 shows the computed rotor wake and the nondimensional inflow for the baseline condition. Dealing with the time marching wake of the tip vortices, it is possible to model the blade vortex interaction and to have a good approximation of the induced velocity of the rotor. We state that this validation model is a very useful test-bed for robustness validation because the dynamics of the blades is different, since the swashplate setting is changed to reach the same trim configuration of the previous model, and the well approximated induced velocity increases the harmonic content of the aerodynamic loads. The baseline loads of fig. 3.8, estimated by the free wake model, are almost an order of magnitude higher than those those of fig. 3.5, estimated with the simple inflow model.

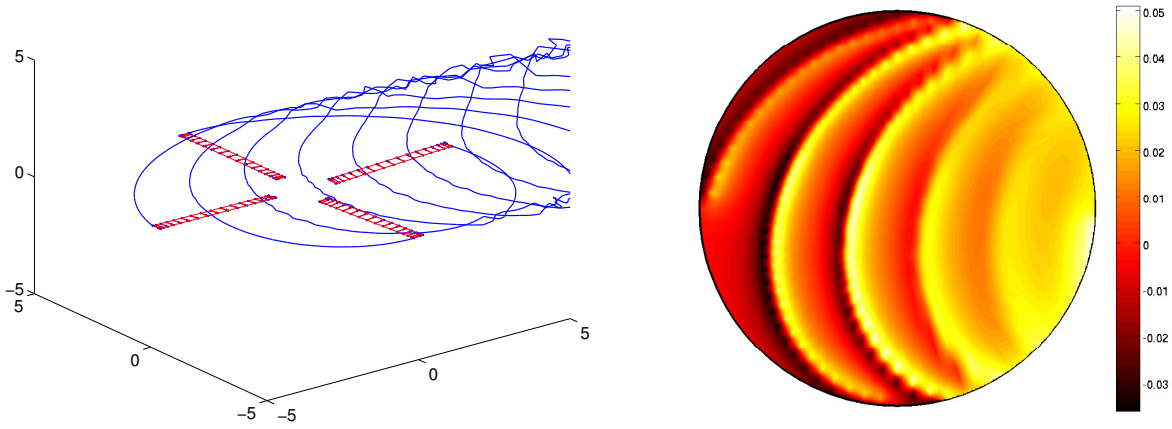

(a) Rotor wake.

(b) Nondimensional inflow at azimuth $\psi = 0^\circ$.

Figure 3.7: Free wake aerodynamics (baseline condition).

The closed loop results are shown in fig. 3.8. Even if the improved aerodynamic model introduces new dynamics and raises the hub loads, none of the two controllers destabilize the rotor system and a good load reduction is still obtained by both of them. The moment M_X of fig. 3.8b is reduced by more than 75% *using both of the controllers. Looking at the force F_Z of fig. 3.8a, the static output feedback controller seems to be more robust and allows a greater reduction than that achieved by the H_2 controller. Such a behavior could be explained by the fact that the dynamic system of the H_2 theory implies a feedback relationship with a periodic state space model, which involves a very large number of controller parameters to be designed and introduces additional dynamics in the closed loop system. On the contrary, the direct output feedback control law is a simple gain matrix that is kept constant throughout the period of the system. It is also interesting to notice, that even in the validation case the higher* $8/rev$ *and* $12/rev$ *harmonics of the hub loads are only negligibly excited. Figure 3.9 reports the applied control voltage. The control activity is significantly higher than that of fig. 3.6 because of the higher loads, but it remains bounded and acceptable, since it doesn't surpass* 800 *V. The application of a high voltage on the helicopter for control purposes remains still a problem for crew safety but the computation of such a value is coherent with what can be found in the literature showing experimental activities. In fact in [35] the active twist blades are excited with an amplitude of* 1000 *V to assess vibrations reduction capabilities, while in [153] a voltage of* ± 500 *V is applied for blade de-icing. From these results we can conclude that the choice of using the periodic static output feedback controller instead of the H_2 one is fully justified by both reduction capabilities and robustness properties. Moreover, it involves fewer parameters in the design phase and it can be easily scheduled to cover the whole flight envelope of the helicopter, because we only have to interpolate a simple algebraic gain matrix depending on the rotor trim condition only. It is useful to remember that the interpolation of state space models, when they arise form an identification procedure or a model reduction technique, is not straightforward, as outlined in [154, 155].*

To complete the study on the periodic controllers, the robustness properties of the POF controller have been also tested on the rotor model simulated with the hybrid full potential CFD aerodynamics

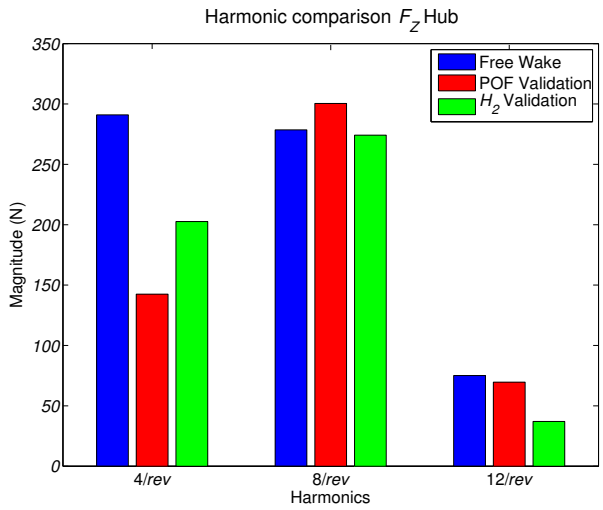

(a) Hub vertical force F_Z.

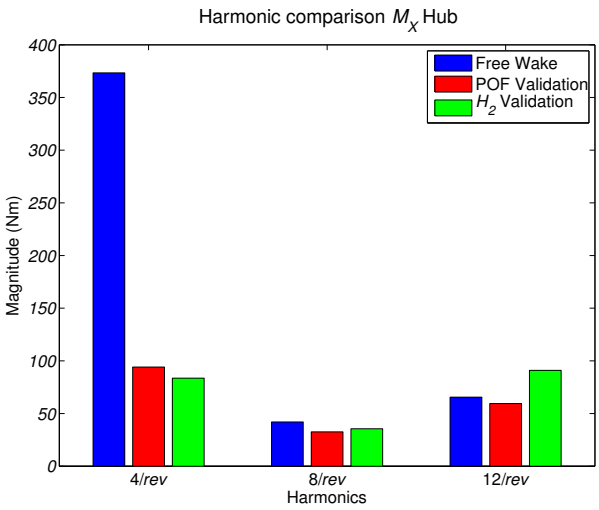

(b) Hub moment M_X.

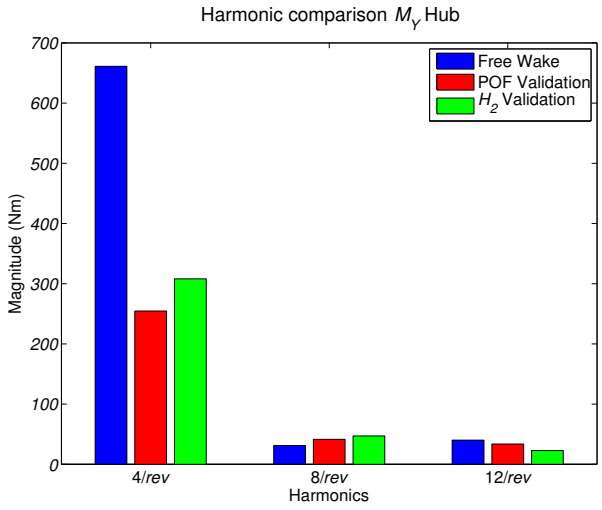

(c) Hub moment M_Y.

Figure 3.8: Validation of the periodic controllers on the Free Wake model.

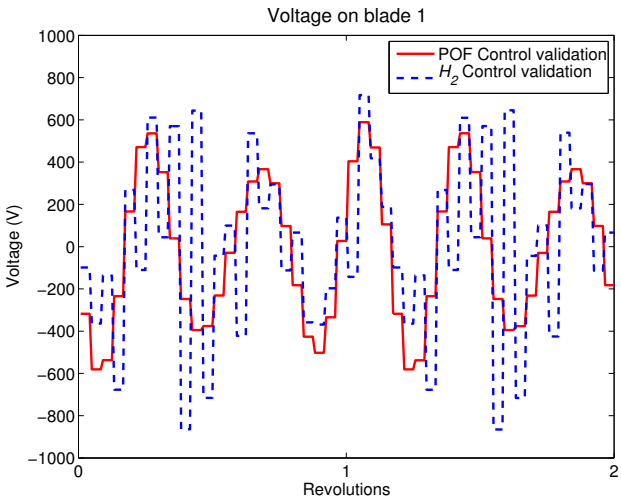

Figure 3.9: Applied voltage on blade 1 in the periodic controller validation phase on the Free Wake model.

combined with the Peters-He inflow model. The Mach number distribution on the advancing blade and the nondimensional inflow for the baseline condition is shown in fig. 3.10. Closed loop results regarding the achieved loads reduction is shown in fig. 3.11. Even if the aerodynamic model is different from both the simple one provided by MBDyn and the Free Wake approach, the controller is able to halve the hub moment vibrations and to ensure the stability of the system. On the other hand the $4/rev$ *harmonic of the vertical force* F_Z *is increased. Such behavior could be due to the underestimation of the* $4/rev$ *loads, since the BVI is not simulated in this aerodynamic model. Being the hub moments vibrations an order of magnitude higher than the one of the vertical force, the controller fails to provide a simultaneous reduction because it has been designed considering a model in which all of the* $4/rev$ *hub loads harmonics have a comparable value. Instead of redesigning the controller, which is the usual procedure in the preliminary phase to meet the required performance in the validation model as well, we propose an alternative solution using only a different pass band filter for the system outputs. Since the* $4/rev$ *harmonic of the measured signals is underestimated by this hybrid aerodynamic model, the pass band filter shown in fig. 3.13 is applied to the blade root shear force* F_z *and the five accelerations along the blade span, so to artificially increase the* $4/rev$ *harmonic content of the signals and hence mitigating the negative effect of the controller on the hub shear force* F_Z*. This approach leads to a better performing controller, as shown in fig. 3.11; the hub vertical force* F_Z *is now only marginally excited and a little improvement of the moments reduction can be appreciated. The control activity for both cases is shown in fig. 3.12 and it remains within acceptable levels. Even if this last example may be not very useful as a validation study, it is very representative and effective to assess the potential of the periodic output feedback control when working far away from the design assumptions. It shows also that satisfactory performance of the controller can be recovered by simply shaping the measures through appropriate filters without altering the closed loop stability.*

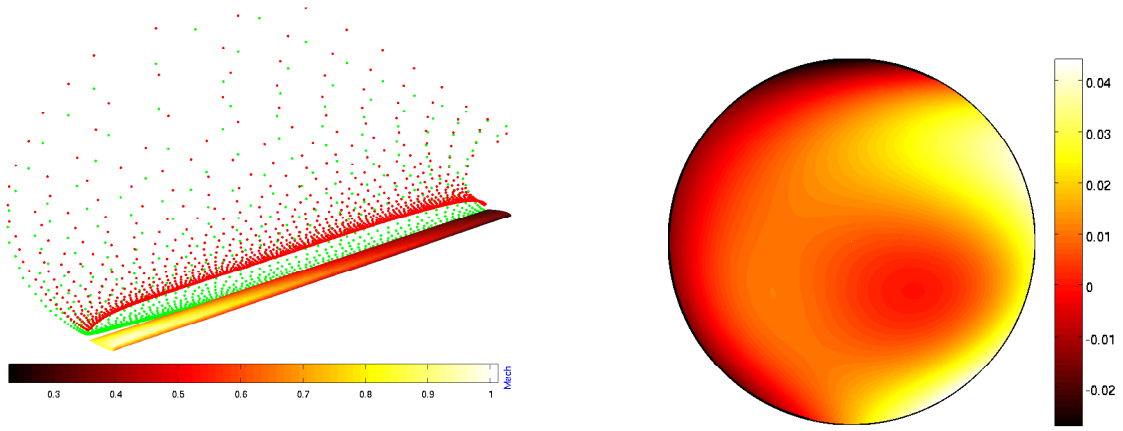

(a) Mach distribution of the advancing Bo105 blade at azimuth Ψ =90°. The wake is opened to represent the potential discontinuity on it, typical of lifting bodies.

(b) Peters-He nondimensional mean inflow over one rotor revolution. $\Delta\phi$

Figure 3.10: Hybrid full potential CFD aerodynamics (baseline condition).

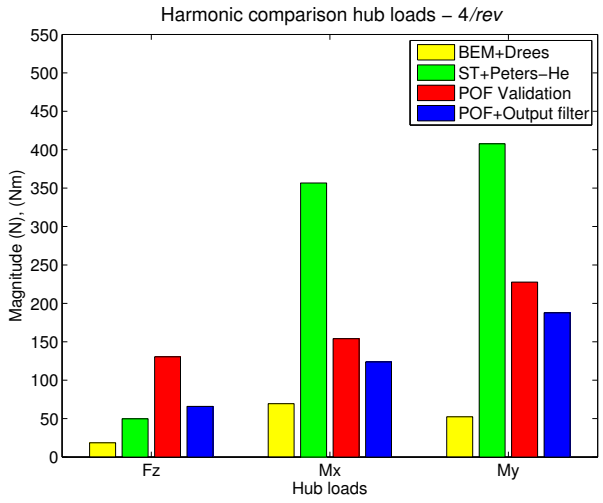

Figure 3.11: POF controller validation on the hybrid full potential CFD code.

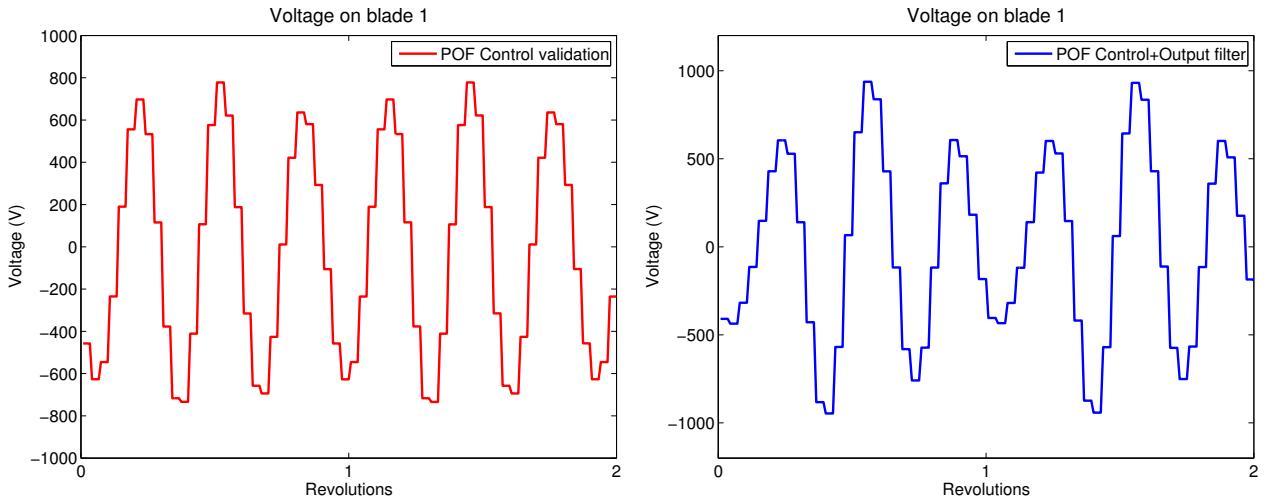

(a) POF Control validation

(b) POF Control combined with the output filters

Figure 3.12: Applied voltage on blade 1 in the POF control validation phase on the hybrid full potential CFD code.

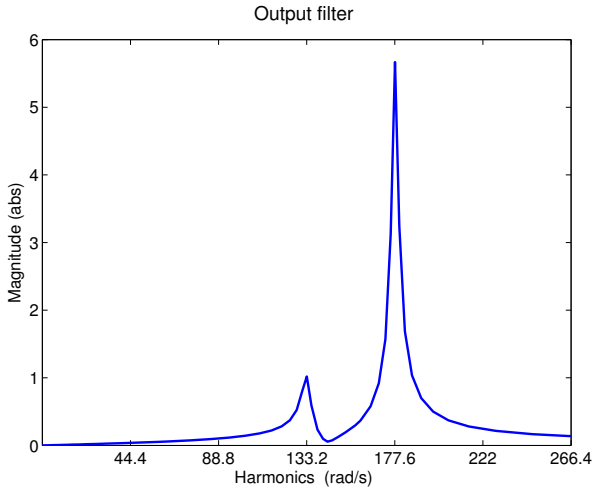

Figure 3.13: Pass band filter applied to the system output to amplify the $4/rev$ harmonic.

Chapter 4

Neural Networks Control

Aeroelastic systems change their properties in relation to the considered flight condition and an efficient control law should be able to carry out its functions over the whole flight envelope without losing its efficiency. Moreover, nonlinear effects may play an important role in aeroelastic response and should be taken into account to increase the performance of the control system. Helicopter rotors show all of the issues outlined and in the case of vibrations reduction it is possible that the use of a nonlinear adaptive control strategy could be the right path to follow to address such a problem. While model based methods require the previous knowledge of the system to be controlled and inevitably introduce approximations in the representation of the aeroelastic response, the black-box approach, such as the one of the neural networks based controllers, is very interesting because of its capability to quickly adapt to model variations and because the identification of the controlled system can be carried out on-line. While different nonlinear adaptive control techniques aimed at suppressing aeroelastic vibrations for fixed-wing aircraft such as feedback linearization [156], sliding mode [157], immersion and invariance [158] and neural networks [159, 160, 161] have been tested on numerical and experimental models, helicopter vibrations are usually reduced by means of linear controllers [162, 163] and nonlinear control applications are preferred for flight dynamics problems as in [164]. The interest in controllers based on neural networks is growing for helicopter applications; for example in [165] a nonlinear adaptive control with a neural network compensator is proposed for trajectory tracking of a model-scaled helicopter. An application of an adaptive neural network identifier to compute a model relating the higher harmonic blade pitch motion to the vibration state can be found in [166]. Vibrations reduction analysis, where a real-time capable Neural Network controller is employed to actuate movable aerodynamic surfaces of the blades can be found in [15, 167]; in [167] the unknown parameters of the rotor model are estimated through an extended Kalman filter.

In this chapter we focus on the application of a nonlinear adaptive neural network control to the helicopter's vibrations reduction problem. In order to represent a dynamic process we use discrete recurrent neural networks (RNN), whose structure is shown in fig. 4.1, instead of the static ones. The jth neuron output at the kth time step is computed as

$$y_j(k) = f(v_j(k)) \tag{4.1}$$

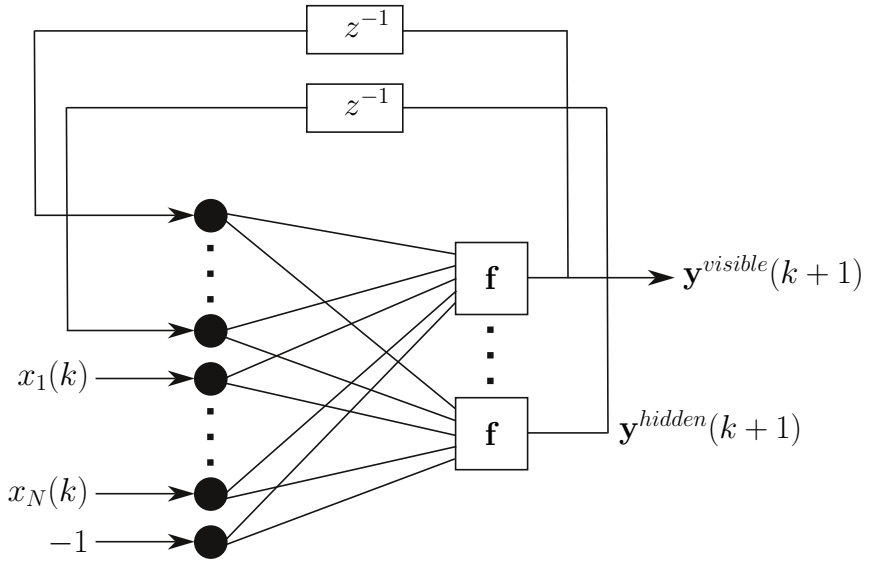

Figure 4.1: Recurrent neural network structure.

and the neuron internal activity $v_j(k)$ is given by

$$v_j(k) = \sum_{i=1}^{N_{in}} W_{ji}(k) u_i(k) \tag{4.2}$$

where N_{in} is the number of the network's input parameters u_i and W_{ji} are the components of the synaptic weights matrix that are initialized with random values and updated at each time step to tune the network. In is useful to notice that among the input parameters there is a constant bias set to -1 to shift the origin of the neuron's activity value. All neurons in this work use the hyperbolic tangent activation function shown in fig. 4.2

$$y_j = \sqrt{3}\tanh\left(\frac{2}{3}v_j(k)\right) \tag{4.3}$$

as suggested by [168]. The chosen activation function limits the network outputs to $\pm\sqrt{3}$ and saturates when the input is too high, leading to the instability of the learning algorithm. The network should be able to learn its evolution path from the input-output data pairs only. The memory is included through a time delay applied to the hidden neurons, defining the state of the network. In this case the input layer **u** *is composed by a set of external input* **x** *and the set of the delayed output of the hidden neurons. The output layer simply consists of the first outputs of the hidden layer $\mathbf{y}^{visible}$. An RNN presents many advantages over static networks because of their smaller size and faster learning. They also have a reduced computational cost, which is very important for real-time control problems [161].*

The complete black-box controller is constituted by an identifier network (ID-RNN) and a controller network (CO-RNN) connected in series, whose synaptic weights matrices $\mathbf{W}_{ID}$ and $\mathbf{W}_{CO}$ are tuned on-line and hence during the simulation. In the following sections these two blocks are explained

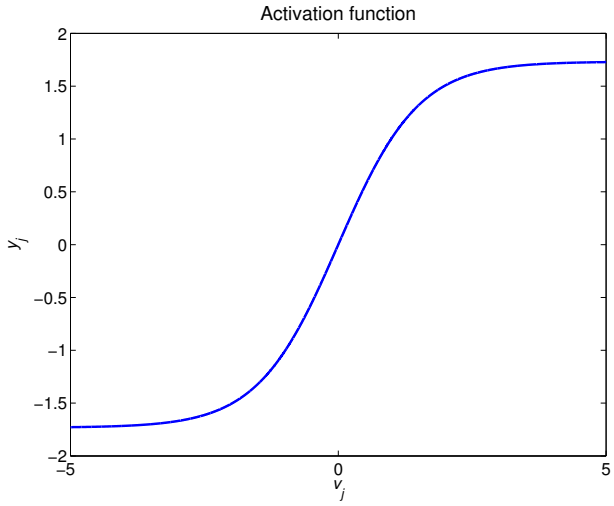

Figure 4.2: Neuron's activation function.

in details and in the last part of this chapter this controller is employed to reduce the hub vibrations of the Bo105 helicopter rotor by means of active twist blades in two different trim configurations to test the adaptive properties of the proposed controller.

4.1 Identifier Network

Neural networks are very promising and common in system identification because they are able to approximate generic nonlinear functions within a desired accuracy. The identifier reproduces the input-output relationship of the system and can be seen as a nonlinear map $\mathbf{P}$ *from the inputs* $\mathbf{u}_{ID}(k)$ *to the prediction of the outputs at the* $(k+1)th$ *time step* $\mathbf{y}_{ID}(k+1)$

$$\mathbf{y}_{ID}(k+1) = \mathbf{P}(\mathbf{u}_{ID}(k)). \tag{4.4}$$

The input vector of the identifier network is composed by the delayed feedback form both the hidden and visible neurons $\mathbf{y}_{ID}^{visible}(k)$ *and* $\mathbf{y}_{ID}^{hidden}(k)$*, the measured variables to be identified* $\mathbf{y}_M(k)$*, the control signals acting on the system* $\gamma(k)$ *and the bias* -1

$$\mathbf{u}_{ID}(k) = \left\{ \begin{array}{cccccc} \mathbf{y}_{ID}^{visible}(k), & \mathbf{y}_{ID}^{hidden}(k), & \mathbf{y}_M(k), & \gamma(k), & -1 \end{array} \right\}^T. \tag{4.5}$$

Subjected to the same input of the physical model, the ID-RNN should be able to minimize the error between its output and the measured one computed and the training law of the network's synaptic weights $\mathbf{W}_{ID}$ *can be obtained through an optimization algorithm that minimizes the following cost function*

$$E_{ID}(k) = \frac{1}{2}\sum_{j=1}^{N_M}\left(y_{M_j}(k) - y_{ID_j}(k)\right)^2. \tag{4.6}$$

where N_M *is the number of the physical system output that we want to identify. Since we are interesting in a nonlinear on-line identification, which leads to an accurate description of the plant under control*

at each sampling time, we use here the Real Time Recurrent Learning (RTRL) algorithm. Adjustments are made to the synaptic weights in real time, while the networks continues to perform its signal processing function [169, 170]. Given that $\mathbf{y}_{ID}(k)$ *depends on* $\mathbf{W}_{ID}$*, the simplest approach to minimize the error of eq. 4.6 is a gradient descent method such as*

$$W_{ID_{kl}}(k+1) = W_{ID_{kl}}(k) - \eta \frac{\partial E_{ID}(k)}{\partial W_{ID_{kl}}(k)} \tag{4.7}$$

and the weights variation goes in the opposite direction of the gradient of the identification error. The parameter η *is the learning rate that governs the ID-RNN training velocity and has to be properly tuned through design simulations: High values may destabilize the training algorithm, leading to a divergence of the synaptic weights, while too low values limit the adaption to system variations.*

The term $\frac{\partial E_{ID}(k)}{\partial W_{ID_{kl}}(k)}$ *of eq. 4.7 can be computed by following the chain of partial derivatives as shown in eqs. 4.8 and 4.9*

$$\frac{\partial E_{ID}(k)}{\partial W_{ID_{kl}}(k)} = -\sum_{j=1}^{N_M} \left(y_{M_j}(k) - y_{ID_j}(k) \right) \frac{\partial y_{ID_j}(k)}{\partial W_{ID_{kl}}(k)} \tag{4.8}$$

$$\frac{\partial y_{ID_j}(k)}{\partial W_{ID_{kl}}(k)} = f'\left(v_{ID_j}(k)\right) \left(\sum_{i=1}^{N_{ID}^{neurons}} W_{ID_{ji}}(k) \frac{\partial y_{ID_j}(k)}{\partial W_{ID_{kl}}(k)} + \delta_{jk} u_{ID_l}(k) \right), \tag{4.9}$$

where $N_{ID}^{neurons}$ *is the chosen number of the ID-RNN neurons. To effectively compute the error gradient, the RTRL algorithm introduces an approximation. The weights variation during the training phase is neglected and the term* $\frac{\partial y_{ID_j}(k)}{\partial W_{ID_{kl}}(k)}$ *of eq. 4.9 is replaced with the one computed at the previous time step* $(k-1)$

$$\frac{\partial y_{ID_j}(k)}{\partial W_{ID_{kl}}(k)} = \frac{\partial y_{ID_j}(k)}{\partial W_{ID_{kl}}(k-1)}, \tag{4.10}$$

which is initialized as the null matrix at the beginning of the simulation. This approximation has been verified through simple simulations and does not invalidate the identification algorithm.

4.2 Controller Network

The control strategy can be considered by a nonlinear map $\mathbf{G}$ *form the inputs* $\mathbf{u}_{CON}(k)$ *to the prediction of the suitable control signals at the* $(k+1)th$ *time step* $\gamma(k+1)$ *to obtain the desired system outputs* $\mathbf{y}^{ref}(k+1)$

$$\gamma(k+1) = \mathbf{G}(\mathbf{u}_{CON}(k)). \tag{4.11}$$

The inputs to the CO-RNN $\mathbf{u}_{CON}(k)$ *are, apart from the delayed feedback* $\mathbf{y}_{CON}^{visible}(k)$ *and* $\mathbf{y}_{CON}^{hidden}(k)$*, the outputs of the ID-RNN* $\mathbf{y}_{ID}(k+1)$*, the control signals acting on the system* $\gamma(k)$ *and the bias* -1

$$\mathbf{u}_{CON}(k) = \left\{ \begin{array}{cccccc} \mathbf{y}_{CON}^{visible}(k), & \mathbf{y}_{CON}^{hidden}(k), & \mathbf{y}_{ID}(k+1), & \gamma(k), & -1 \end{array} \right\}^T \tag{4.12}$$

Similarly to the ID-RNN case, the training of the controller can be interpreted as an optimization algorithm which minimizes the following cost function:

$$E_{CON}(k) = \frac{1}{2}\sum_{j=1}^{N_M}\left(y_j^{ref}(k+1) - y_{ID_j}(k+1)\right)^2 + \frac{1}{2}\rho\sum_{j=1}^{N_C}\gamma_j^2(k), \tag{4.13}$$

where $\mathbf{y}^{ref}(k+1)$ is the reference output and N_C is the number of control signals. The tunable parameter ρ is defined as the control signal penalization and is used to limit the control effort in a way similar to to what is done in a classical LQG controller. In this case, the penalty term is necessary to avoid the divergence of the control [160, 161]. As shown for the ID-RNN, the gradient descent algorithm is used to minimize the cost function of eq. 4.13 and to update the synaptic weights $\mathbf{W}_{CON}$

$$W_{CON_{kl}}(k+1) = W_{CON_{kl}}(k) - \eta\frac{\partial E_{CON}(k)}{\partial W_{CON_{kl}}(k)} \tag{4.14}$$

The gradient of the cost function can be derived analytically:

$$\frac{\partial E_{CON}(k)}{\partial W_{CON_{kl}}(k)} = -\sum_{j=1}^{N_M}\left(y_j^{ref}(k+1) - y_{ID_j}(k+1)\right)\frac{\partial y_{ID_j}(k+1)}{\partial W_{CON_{kl}}(k)} + \rho\sum_{j=1}^{N_C}\gamma_j(k)\frac{\partial \gamma_j(k)}{\partial W_{CON_{kl}}(k)}, \tag{4.15}$$

where the presence of the cross term $\frac{\partial y_{ID_j}(k+1)}{\partial W_{CON_{kl}}(k)}$ makes it explicit the coupling between the two networks and it can be computed as

$$\frac{\partial y_{ID_j}(k+1)}{\partial W_{CON_{kl}}(k)} = f'\left(v_{ID_j}(k)\right)\sum_{i=1}^{N_C} W_{ID_{j(i+N_{ID}^{neurons}+N_M)}}(k) f'\left(v_{CON_j}(k)\right)\left(\sum_{i=1}^{N_{CON}^{neurons}} W_{CON_{ji}}(k)\frac{\partial y_{CON_j}(k)}{\partial W_{CON_{kl}}(k)} + \delta_{jk}u_{CON_l}(k)\right). \tag{4.16}$$

The term related to the control penalization can be obtained as

$$\sum_{j=1}^{N_C}\gamma_j(k)\frac{\partial \gamma_j(k)}{\partial W_{CON_{kl}}(k)} = \sum_{j=1}^{N_C} y_{CON_j}(k)\frac{\partial y_{CON_j}(k)}{\partial W_{CON_{kl}}(k)}. \tag{4.17}$$

Similarly to what explained for the ID-RNN, the variation of the weights is neglected and $\frac{\partial y_{CON_j}(k)}{\partial W_{CON_{kl}}(k)}$ is given by $\frac{\partial y_{CON_j}(k+1)}{\partial W_{CON_{kl}}(k)}$ computed at the previous time step.

Once the identifier and the controller networks are implemented the dynamic black-box controller is connected to the aeroelastic system as shown in fig. 4.3. It is useful to remark that all external inputs to the networks have to be normalized to avoid the saturation of the activation functions of eq. 4.3. Therefore the measures $\mathbf{y}_M(k)$ and the control signals $\gamma(k)$, which enter in the ID-RNN block are divided by a scaling factor and then the outputs of the CO-RNN block $\gamma(k+1)$ are multiplied by a gain to adjust the bounds of the control action (note that $\gamma(k+1)$ and $\gamma(k)$ share the same normalization factor). These scaling and amplification factors are design parameters that have to be properly tuned, along with the network parameters, to ensure the correct function of the neural networks and to provide a suitable magnitude of the control activity.

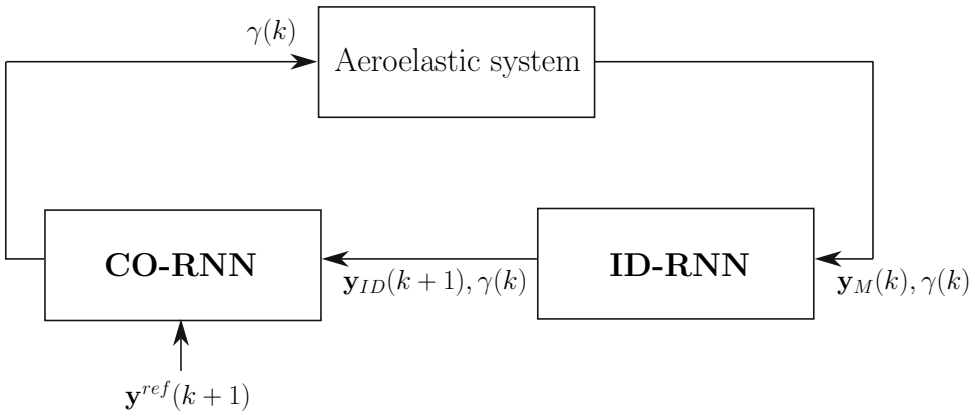

Figure 4.3: Neural network controller architecture.

4.3 Simulation Results

4.3.1 Controller Design

The neural network controller is here adapted to suppress helicopter vibrations and is applied to the multibody model of the Bo105 rotor. Here only the simple aerodynamics provided by MBDyn is considered, because of its low computational effort in the design simulations that are carried out by the coupling between MBDyn and Simulink, in which the RNN control is implemented. Following the same idea for the design of the periodic controllers, we are interested in minimizing the $4/rev$ *and the* $3/rev$ *harmonics of the blade root shear force* F_z *to minimize the* $4/rev$ *harmonic of the hub vertical force* F_Z *and to act on the* $4/rev$ *harmonic of the hub moments* M_X *and* M_Y*.*

The identifier approximates on-line the nonlinear map between the applied voltage on the blade V *and the blade root shear force* F_z*, while the controller computes the voltage to be applied to minimize the blade response. Therefore, to match the notation of the previous sections, the measured output of the physical system is* $y_M(k) = F_z(k)$*, the control signal is* $\gamma(k) = V(k)$ *and the identified output is* $y_{ID}(k+1) = F_{ID_z}(k+1)$*. Since we want to consider only the harmonics of the blade force* F_z *that have to be minimized by the controller, the pass-band filter shown in fig. 4.4 is applied to the blade response before the ID-RNN. The reference signal* $y^{ref}(k+1)$ *is equal to* 0 *for the whole simulation. Even in this application, the controller is designed for the blade having initial azimuth* $\psi = 0$ *only and taking into account the periodicity of the system, the same control signal is delayed and applied to the other blades.*

The two trim configurations, at advancing parameters of $\mu = 0.23$ *and* $\mu = 0.33$*, are analyzed and we choose to use* 120 *time steps per rotor revolution for both simulations. Since there is not a general rule to apply, the controller parameters are tuned through several simulations for the higher advancing velocity case, where vibrations are significantly stronger. The results of the networks tuning are shown in tab. 4.1. A scaling factor of* 200 *is applied to the filtered measure of the blade root vertical force* F_z*, while a gain of* 300 *is used for the controller output* V*. It is important that the measured variable is normalized to avoid the network saturation, but in the meantime the input to the identifier should have an adequate magnitude with respect to system noises for the learning algorithm to perform correctly.*

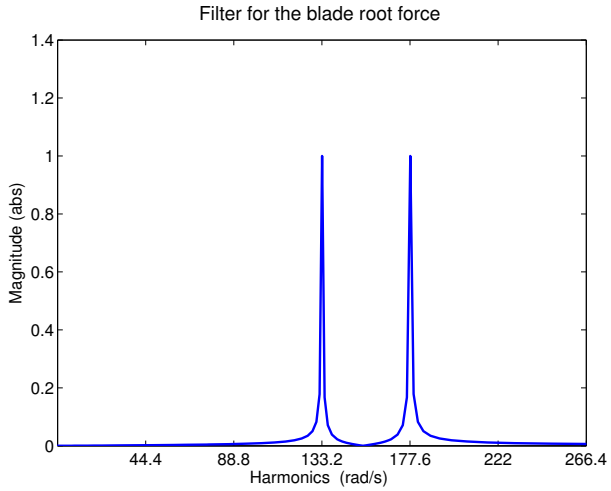

Figure 4.4: Filter used on the system output F_z.

Table 4.1: Networks parameters.

	ID-RNN	**CO-RNN**
$N^{neurons}$	3	3
η	$2 \cdot 10^{-1}$	$1 \cdot 10^{-1}$
ρ	-	$1 \cdot 10^{-4}$

To show the potentiality of the proposed adaptive controller, the already designed controller is used for the other flight condition. Results for both cases are shown in figs. 4.5 and 4.6. As it can be seen in such figures, a great reduction of vibratory loads is achieved and up to 90% reduction is obtained in the flight condition where the controller parameters have been tuned. It is interesting to notice that even for the flight condition at $\mu = 0.23$ *the results are good and the drop of vibratory loads is satisfactory. Figures 4.7 and 4.8 show the computed control signals for the two configurations. The maximum amplitude of the electric potential remains within reasonable levels, it does not exceed peaks of* 300 *V; note that due to the nature of the synaptic function of eq. 4.3 and to the chosen controller gain* 300*, the maximum voltage allowed by the neural controller is about* 520 *V.*

4.3.2 Controller Validation

After having tuned the two networks, the ID-RNN and the CO-RNN, on the design model, showing the capability of the neural controller to adapt itself in different flight conditions, the next step is to verify the robustness of the proposed controller to assess the possibility and the effects of a practical implementation. The validation model is built by coupling the multibody rotor with the free wake aerodynamic code described previously and the rotor is trimmed at $\mu = 0.23$*. The parameters of the networks, shown in tab. 4.1, are left unchanged and the black-box controller is fed back to the rotor model. The crucial aspect of practical implementations, when dealing with neural networks, is that we usually do not have an exact estimate of the magnitude of the real system loads. Therefore if the normalization of the input measures to the ID-RNN is not appropriate, saturation or performance degradation may occur. While a gain of* 800 *is used to limit the control activity, we can easily measure the baseline loads, after the trim condition is reached, and then tune the normalization factors for the blade root shear force trying to maintain the same proportions achieved during the design phase of the controller.*

The results of the closed loop simulation are shown is fig. 4.9. The nonlinear adaptive controller fully satisfies our expectations and is able to properly adapt to the behavior of this rotor model using a more accurate aerodynamic prediction. It can be seen that the $4/rev$ *harmonic of the hub loads* F_Z*,* M_X *and* M_Y *are reduced by* 43%*,* 83% *and* 65% *respectively, providing only a marginal excitation to the higher* $8/rev$ *and* $12/rev$ *harmonics and the computed control activity, represented in fig. 4.10, has peaks smaller that* 500 *V.*

The results obtained in this section are very interesting and the adaptive nonlinear black-box approach shows the potential for the vibration reduction of helicopters. However, the fact that there is not a general rule to tune the network parameters and the normalization factors makes it difficult to design an adaptive controller to cover the flight envelope and further investigations is required in order to use neural networks in real helicopters.

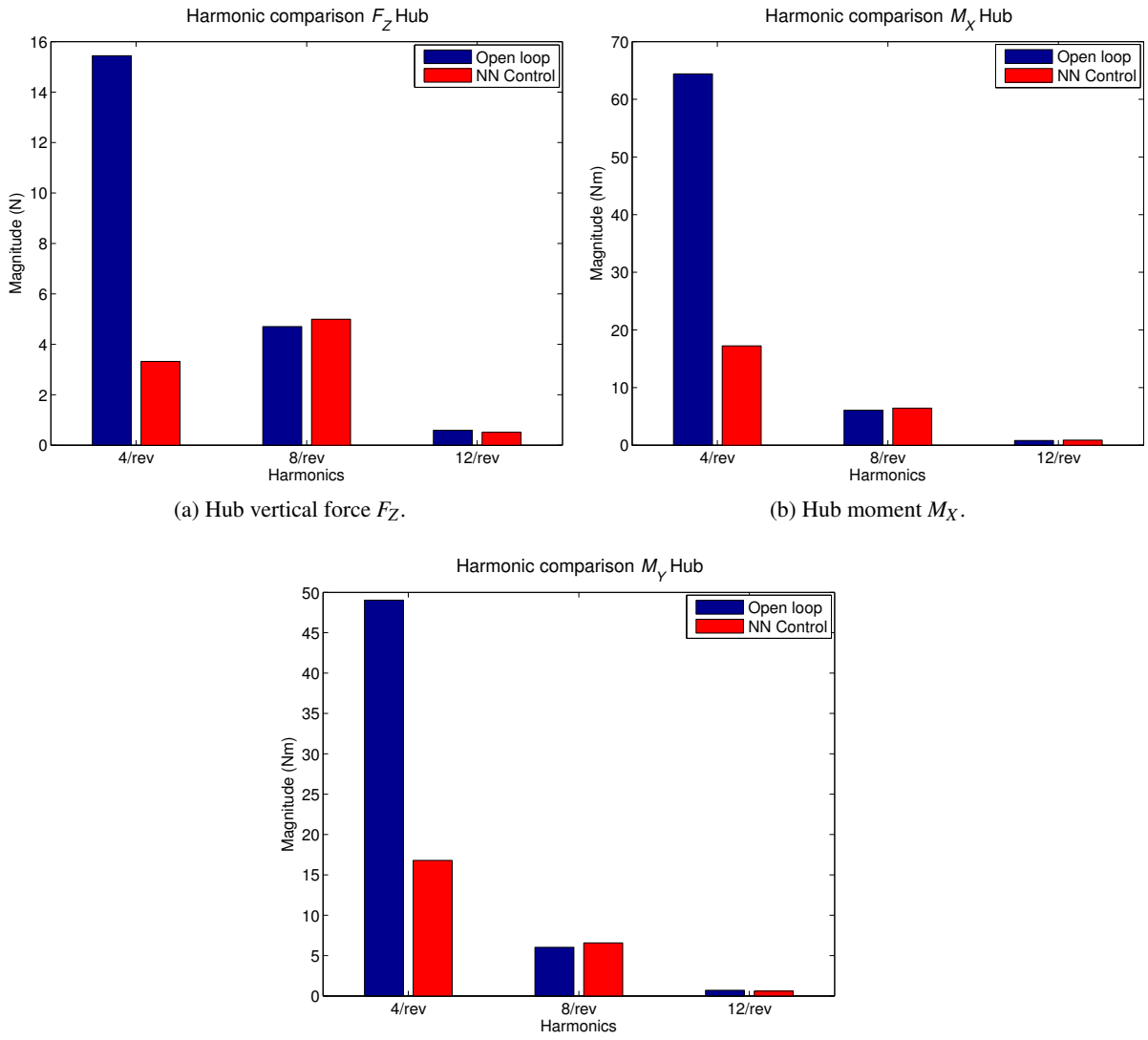

(a) Hub vertical force F_Z.

(b) Hub moment M_X.

(c) Hub moment M_Y.

Figure 4.5: NN control. Vibrations reduction for the trim condition at $\mu = 0.23$.

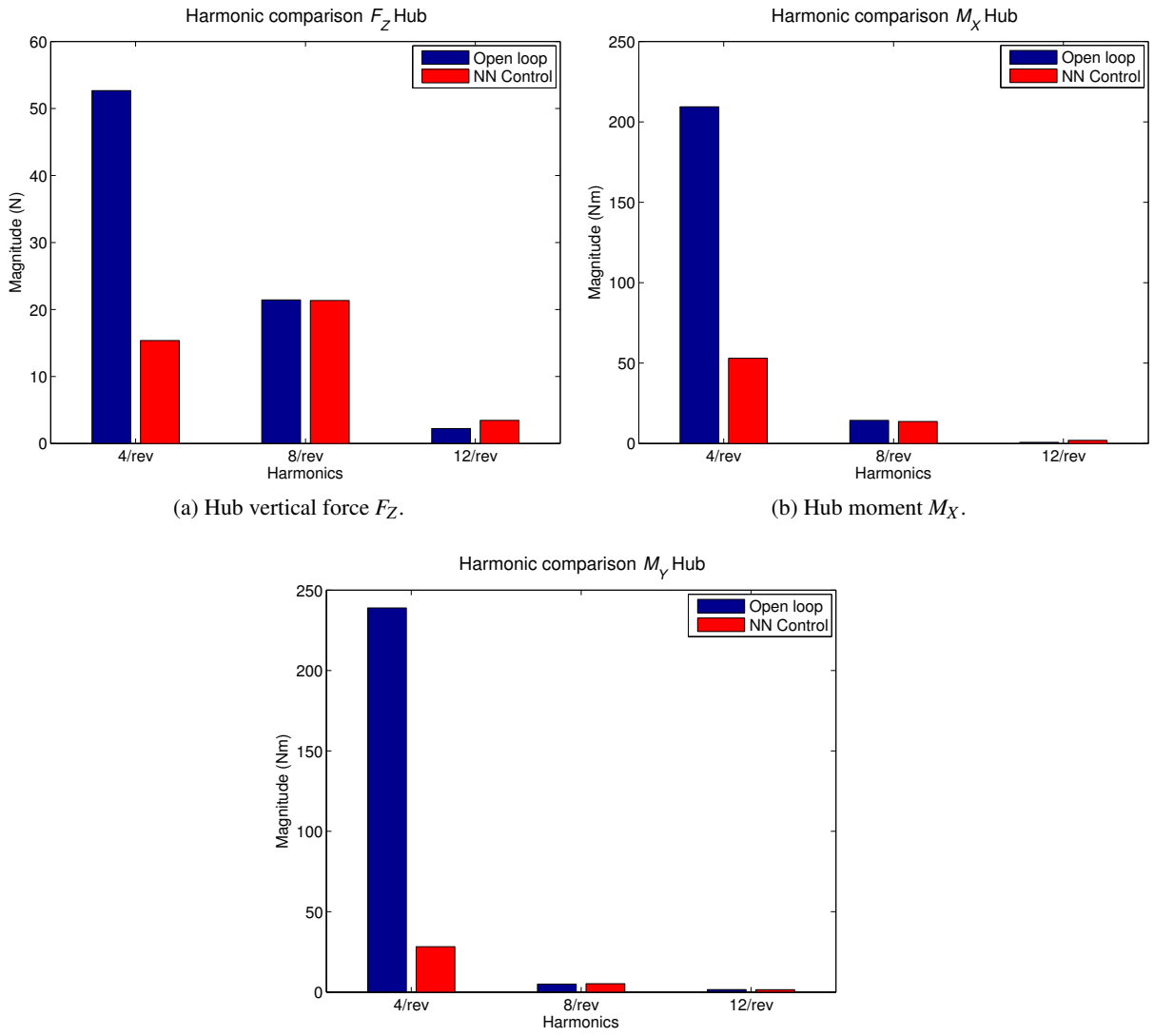

(a) Hub vertical force F_Z.

(b) Hub moment M_X.

(c) Hub moment M_Y.

Figure 4.6: NN control. Vibrations reduction for the trim condition at $\mu = 0.33$.

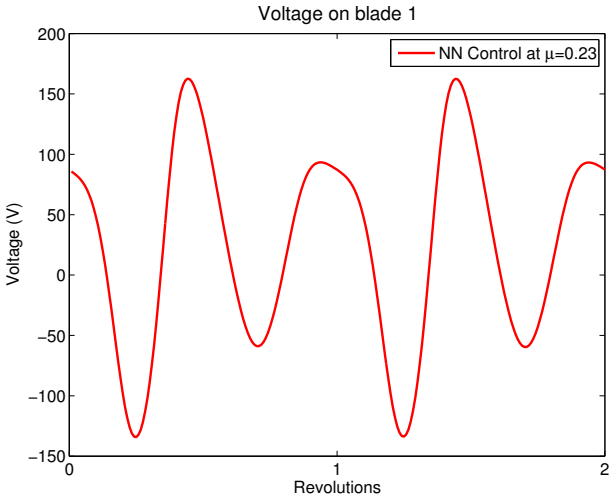

Figure 4.7: NN control. Applied voltage on blade 1 at $\mu = 0.23$.

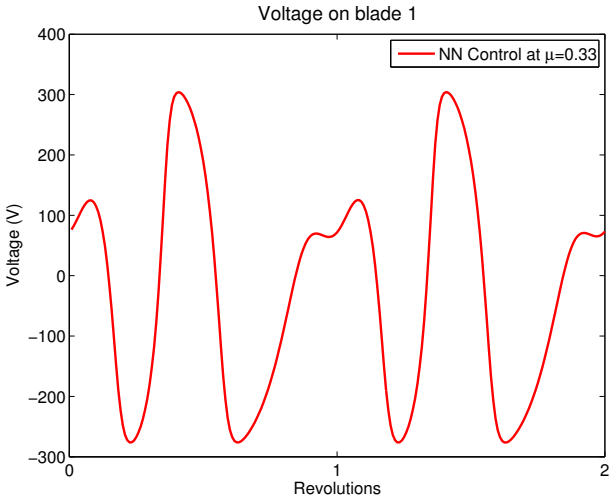

Figure 4.8: NN control. Applied voltage on blade 1 at $\mu = 0.33$.

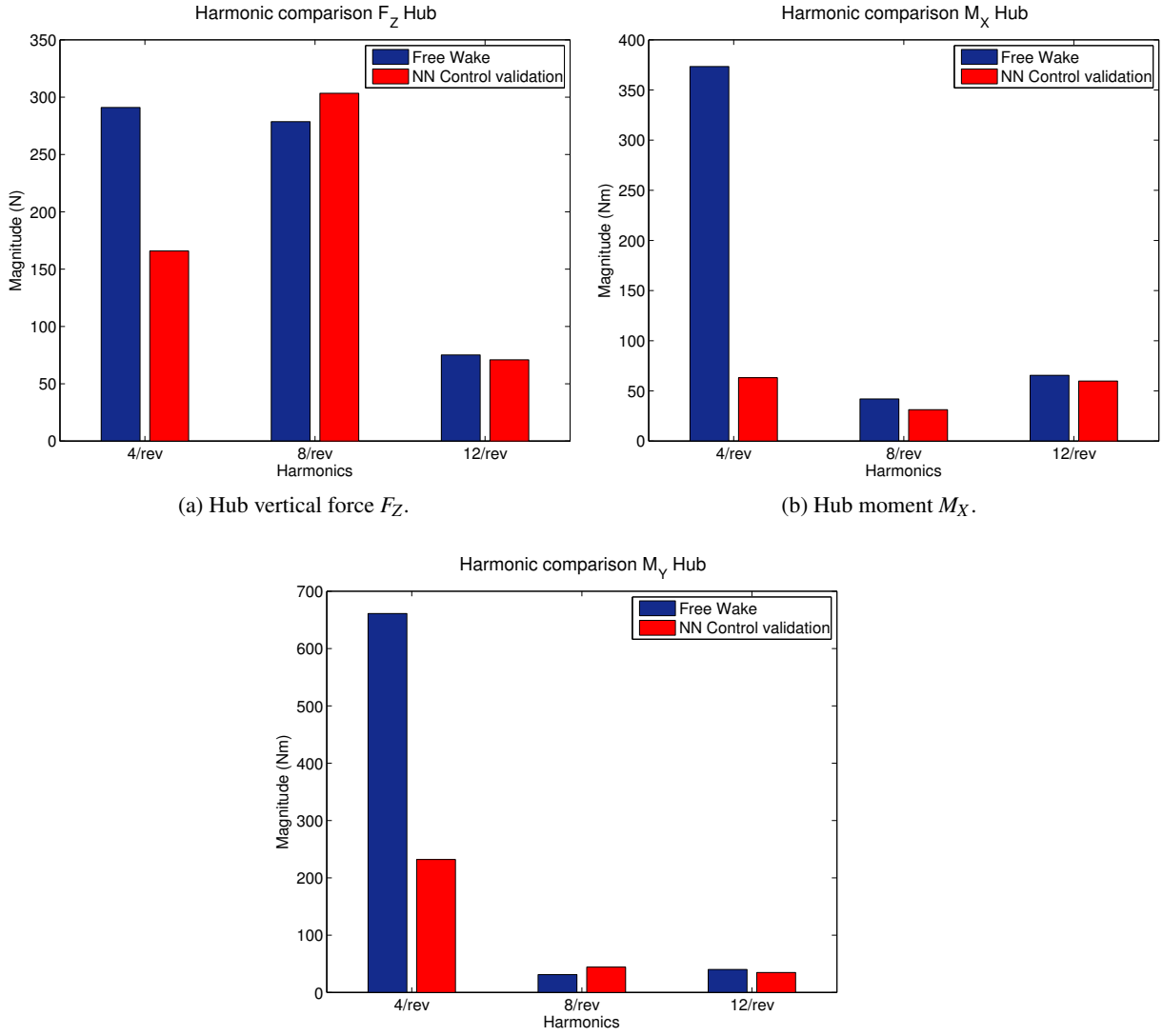

(a) Hub vertical force F_Z.

(b) Hub moment M_X.

(c) Hub moment M_Y.

Figure 4.9: NN Controller validation on the Free Wake model for the trim condition at $\mu = 0.23$.

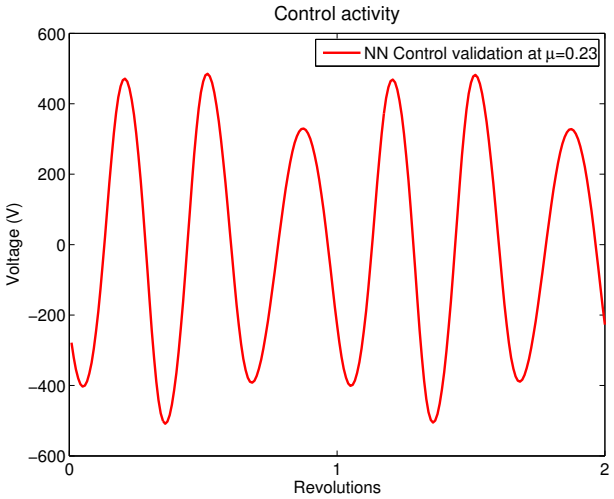

Figure 4.10: Applied voltage on blade 1 in the NN control validation on the Free Wake model at $\mu = 0.23$.

Chapter 5

Higher Harmonic Control

A widely studied control system to actively reduce vibrations in rotorcraft applications uses the actuation of the blades at higher harmonics to generate unsteady forces that counteract the vibratory loads. The control signal u_k is computed as a sum of harmonics higher than the $1/rev$

$$u_k = \sum_{n=2}^{N} \left(\gamma_{c,n} cos\left(n\Omega k dt\right) + \gamma_{s,n} sin\left(n\Omega k dt\right) \right), \tag{5.1}$$

whose coefficients, $\gamma_{c,n}$ and $\gamma_{s,n}$ are obtained through the higher harmonic control (HHC) algorithm. In the first applications, the HHC technique moves the already available swashplate to control the pitch of the blades at higher frequencies as reported in [27, 28]. However, this approach is not able to control the blades individually, so that harmonics arising from rotor dissimilarities having a frequency non multiple of the rotational one cannot be reduced. In recent years, HHC has been extensively employed in individual blade control (IBC) applications thanks to its effectiveness and simplicity; for example in [171] the vibrations are reduced by means of microflaps and HHC. The implementations of such a controller are not only limited to vibration suppression, but it is also used to mitigate other problems, e. g. noise, or to improve the efficiency of rotary wing aircraft. In [172] the HHC algorithm is employed to alleviate the blade vortex interaction related noise, while in [48] a simultaneous vibration reduction and performance enhancement is performed.

Although HHC provides very good results, it suffers from some limitations. First of all, it is based on a quasi-static and linear approximation of the rotor behavior, which cannot be very effective when strong nonlinearities occur, especially when a non adaptive version is used. Moreover, the actuator saturations is not taken into account. Several studies have been performed in the literature to solve these issues to increase HHC performance in real implementations. In order to make the controller more robust to model uncertainties, a H_∞ approach for the HHC is presented in [173, 174]. The problem of providing a suitable and realistic control effort, considering the actuator saturations is usually treated in very simple ways, which degrade controller performance [175]. The simplest method is the truncation of the signal as it reaches the saturation value. Another approach is to multiply the control signal by a scaling factor, or the weights used to design the controller can be properly tuned to limit the control action. A very effective actuator constraints handling is shown in [176], where a nonlinear constrained optimization is carried out to minimize the cost function of the HHC technique.

In this chapter an adaptive version of the HHC algorithm is presented and then the actuator constraints are included in the design process of the control signal through an elegant way, as suggested by [177], relying on the quadratic programming, which is more suitable for real time capabilities. After showing the effectiveness of the classical adaptive controller through a closed loop simulation, two verifications with different imposed constraints on the control signal are shown to assess the capability of the proposed solution.

5.1 Classic Adaptive Higher Harmonic Control

The main approximation of the HHC algorithm is the modeling of the rotor subsystem for each step k with a quasi static linear transfer function between the cosine and sine amplitudes of the blade control signal harmonics, represented in the vector γ, and the cosine and sine amplitudes of the hub loads harmonics, comprised in the vector $\mathbf{f}$

$$\mathbf{f}_{k+1} = \mathbf{f}_k + \mathbf{T}_k \left(\gamma_{k+1} - \gamma_k\right). \tag{5.2}$$

Being this equation based on a quasi static assumption of the rotor behavior, the step k is usually updated after a certain number of rotor revolutions to let the system reach the steady state condition.

The transfer matrix $\mathbf{T}_k$ has to be properly identified to achieve good results in the closed loop simulations and since the helicopter rotor exhibits a strong nonlinear behavior, depending on the swashplate orientation and the flight condition, an adaptive on-line identification algorithm is the best choice. In this work we decided to use the recursive least squares (RLS) algorithm as suggested in [178] and the matrix $\mathbf{T}_k$ can be updated at each step k following these equations

$$\begin{array}{rcl} \mathbf{K}_{k+1} &=& \left(\alpha + \triangle\gamma_k^T \mathbf{P}_k \triangle\gamma_k\right)^{-1} \triangle\gamma_k \mathbf{P}_k \\ \mathbf{T}_{k+1} &=& \mathbf{T}_k + \left(\triangle\mathbf{f}_k - \mathbf{T}_k \triangle\gamma_k\right) \mathbf{K}_{k+1}, \\ \mathbf{P}_{k+1} &=& \mathbf{P}_k \left(\frac{1}{\alpha}\mathbf{I} - \triangle\gamma_k \mathbf{K}_{k+1}\right) \end{array} \tag{5.3}$$

where the matrix $\mathbf{K}$ is the gain, $\mathbf{P}$ is the covariance error matrix, $\triangle\mathbf{f}_k = \mathbf{f}_k - \mathbf{f}_{k-1}$, $\triangle\gamma_k = \gamma_k - \gamma_{k-1}$ and α is the exponential window parameter acting as a forgetting factor varying $0 < \alpha \leq 1$.

After having obtained an accurate estimate of the transfer matrix $\mathbf{T}_k$, the classical HHC algorithm computes the harmonics of the control signal to be applied at the subsequent step γ_{k+1} through the minimization of the following quadratic cost function J

$$min_\gamma J = \frac{1}{2}\left(\mathbf{f}_{k+1}^T \mathbf{W}_z \mathbf{f}_{k+1} + \gamma_{k+1}^T \mathbf{W}_\gamma \gamma_{k+1} + \triangle\gamma_{k+1}^T \mathbf{W}_{\triangle\gamma} \triangle\gamma_{k+1}\right). \tag{5.4}$$

The weighting matrices $\mathbf{W}_z$, $\mathbf{W}_\gamma$ and $\mathbf{W}_{\triangle\gamma}$, applied to the hub loads to be reduced, the control signal harmonics and to their increment respectively, are properly tuned in the controller design phase in order to achieve the required performance. The minimization of the quadratic cost function of eq. 5.4 can be carried out analytically and the harmonics of the control signal can be computed as

$$\gamma_{k+1} = \left(\mathbf{T}_k^T \mathbf{W}_z \mathbf{T}_k + \mathbf{W}_\gamma + \mathbf{W}_{\triangle\gamma}\right)^{-1} \left[\mathbf{T}_k^T \mathbf{W}_z \left(\mathbf{f}_k - \mathbf{T}_k \gamma_k\right) - \mathbf{W}_{\triangle\gamma} \gamma_k\right]; \tag{5.5}$$

the control signal is then reconstructed as in eq. 5.1. The computation of the control signal is repeated every several k steps until the hub vibrations are sufficiently reduced and convergence is reached. The on-line identification is kept active during the control updates to ensure a reliable estimate of the rotor transfer function during the application of the control signal, since the rotor behavior is nonlinear.

5.2 Actuator Constraints Handling

The prediction of the magnitude of the computed signal is a crucial aspect of the classical approach, as the actuators may reach the saturation point or undesirably high control inputs may occur. As described before, this issue is taken into account properly by a nonlinear constrained optimization of the cost function J of eq. 5.4 as explained in [176].

Being the nonlinear optimization algorithms very expensive to be used into real time applications, a more elegant way to handle actuator constraints, as proposed by [177] , is presented in this work. The main idea is to replace the nonlinear constraints with a set of linear inequalities, so that the problem can be solved using quadratic programming. The constraints on the control signal are taken into account by imposing a limitation $\bar{V}$ on the magnitude of each harmonic n composing the signal. Being the exact nonlinear form of the constraint $\sqrt{\gamma_{c,n}^2+\gamma_{s,n}^2} \leq \bar{V}$ not suitable for a fast implementation, it is relaxed and a stricter set of linear constraints, formulated as the sum of the absolute values $|\gamma_{c,n}|$ and $|\gamma_{s,n}|$, is used, leading to the following optimization problem

$$\begin{array}{rcc} min_{\gamma} J & = & \frac{1}{2}\left(\mathbf{f}_{k+1}^T \mathbf{W}_z \mathbf{f}_{k+1} + \gamma_{k+1}^T \mathbf{W}_{\gamma} \gamma_{k+1} + \triangle\gamma_{k+1}^T \mathbf{W}_{\triangle\gamma} \triangle\gamma_{k+1}\right) \\ s.t. & & |\gamma_{c,n}| + |\gamma_{s,n}| \leq \bar{V} \end{array} \tag{5.6}$$

where n represents the index of the constrained harmonic of the signal. By substituting the quasi static approximation of the rotor model of eq. 5.2 into eq. 5.6 and ignoring all the terms independent from γ_{k+1}, since it is a minimization problem, the cost function can be written considering only the quadratic and the linear term, as shown in eq. 5.7

$$min_{\gamma_{k+1}} J = \frac{1}{2}\left(\gamma_{k+1}^T \mathbf{H}\mathbf{H} \gamma_{k+1} + \mathbf{g}\mathbf{g}^T \gamma_{k+1}\right). \tag{5.7}$$

To obtain a set of linear inequalities necessary for the implementation using the quadratic programming approach, the following change of variable is needed

$$\gamma = \mathbf{x}^+ - \mathbf{x}^-, \tag{5.8}$$

with the new introduced variables $\mathbf{x}^+$ and $\mathbf{x}^-$ always positive. Substituting the change of variable of eq. 5.8 into the constraints of eq. 5.6, they can be reformulated as:

$$\begin{array}{c} -\left(x_{c,n}^+ + x_{c,n}^-\right) - \left(x_{s,n}^+ + x_{s,n}^-\right) \geqslant -\bar{V} \\ \mathbf{x}^+ \geqslant 0 \\ \mathbf{x}^- \geqslant 0 \end{array} . \tag{5.9}$$

The change of variable of eq. 5.8 is substituted to the cost function of eq. 5.6 as well, leading to the classical quadratic optimization problem

$$\begin{array}{rcc} min_{\mathbf{x}_{k+1}} J & = & \frac{1}{2}\left(\mathbf{x}_{k+1}^T \mathbf{H} \mathbf{x}_{k+1} + \mathbf{g}^T \mathbf{x}_{k+1}\right) \\ s.t. & & \mathbf{C}\mathbf{x} \geqslant \mathbf{d} \end{array} \tag{5.10}$$

where $\mathbf{H} = \begin{bmatrix} \mathbf{HH} & -\mathbf{HH} \\ -\mathbf{HH} & \mathbf{HH} \end{bmatrix}$ and $\mathbf{g} = \begin{Bmatrix} \mathbf{gg} \\ -\mathbf{gg} \end{Bmatrix}$. This optimization problem is solved at each step of the controller k in this work through the interior point method as explained in [179, 180]. The

interior point algorithm is very fast and usually reaches the solution after few iterations, providing an optimization method capable to operate in real time applications within the controller step k, which usually comprises 3 *or* 5 *rotor revolutions. An implementation of this controller for the tracking control of an experimental rotor model using the multiple swashplate can be found in [181].*

5.3 Simulation Results

The simulations carried out in this section are aimed at showing the effectiveness of the presented HHC algorithm and the Bo105 rotor model trimmed at an advance parameter of $\mu = 0.23$ *is considered as test case. The quasi static model of eq. 5.2 in these examples maps the cosine and sine amplitudes of the applied voltage* V*, stacked in the vector* γ*, directly to the cosine and sine amplitudes of the* $4/rev$ *harmonic of the hub loads represented in the vector* $\mathbf{f}$*. We limited our study to the minimization of the hub shear force* F_Z *and the two hub moments* M_X *and* M_Y*, while the control signal is composed by harmonics ranging from the* $2/rev$ *to the* $5/rev$*, leading to a* $(6x8)$ *transfer matrix* $\mathbf{T}$*. Note that the computed harmonics of the control voltage are the same for the four blade and then the phase of the four control signals are shifted according to the azimuth position of the blades*

$$V_{k_{N_b}} = \sum_{n=2}^{5} \left(\gamma_{c,n} cos \left(n\Omega kdt + (N_b - 1)\frac{\pi}{2} \right) + \gamma_{s,n} sin \left(n\Omega kdt + (N_b - 1)\frac{\pi}{2} \right) \right),$$

where N_b *is the index of the blade.*

The identification of the transfer matrix $\mathbf{T}_k$ *is done on-line during the simulation and its estimate is updated every* 3 *rotor revolutions. The RLS algorithm requires the initialization of some parameters and while the initial gain* $\mathbf{K}_0$ *and the initial value of the transfer matrix* $\mathbf{T}_0$ *are set to the null matrix, the covariance error matrix* $\mathbf{P}_0$ *is initialized as an upper triangular unit matrix multiplied by a gain equal to* 100*. The forgetting factor* $\alpha = 0.9$ *is considered. The initial magnitude of the covariance error matrix* $\mathbf{P}$ *drives the velocity of the identification algorithm, while the forgetting factor* α *is used to emphasize more recent data with respect to the old ones; it is a parameter that governs the adaptiveness properties.*

The adaptive HHC algorithm is implemented in Simulink and the first closed loop simulation is carried out without imposing the constraints on the control signal. The multibody rotor model is coupled with the hybrid full potential CFD code with the Peters-He wake model and the reduction of the hub vibrations are analyzed. The weighting matrices of the cost function of eq. 5.4 are properly tuned through a couple of simulations to achieve the desired performance; in particular the matrix $\mathbf{W}_z$ *is a diagonal unit matrix having the first two diagonal parameters related to the hub shear force* F_Z *equal to* 10*, otherwise the controller could amplify the hub vertical vibration because its magnitude is much smaller that the one of the two moments. The control weighting matrix* $\mathbf{W}_\gamma$ *is chosen as the unit matrix and the one related to the controller update increment is set to the null matrix. Figure 5.1 shows the* $4/rev$ *harmonic of the hub loads computed with the simple aerodynamic of MBDyn, the hybrid full potential CFD aerodynamics and the vibration alleviation achieved thanks to the HHC controller. It can be seen that the HHC controller is very effective, especially if we consider the hub vertical force* F_Z *that is reduced by* 81%*, and is able to alleviate at the same time the three hub loads. The* $4/rev$ *harmonic of the two hub moments* M_X *and* M_Y *experience a reduction of* 23% *and* 24%*, respectively. The control signal applied on the first blade is shown in fig. 5.2.*

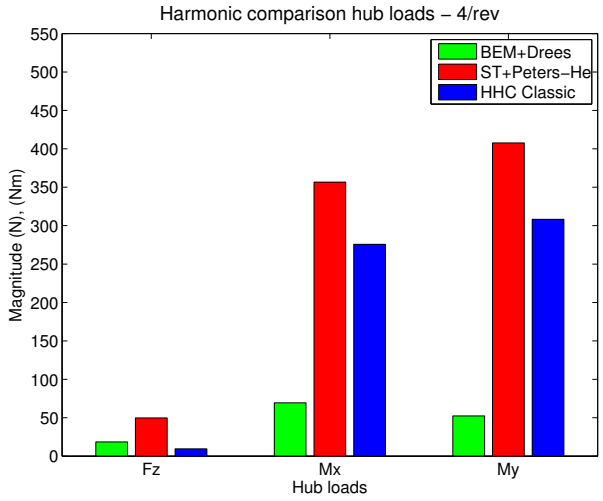

Figure 5.1: Classical adaptive HHC on the hybrid full potential CFD code.

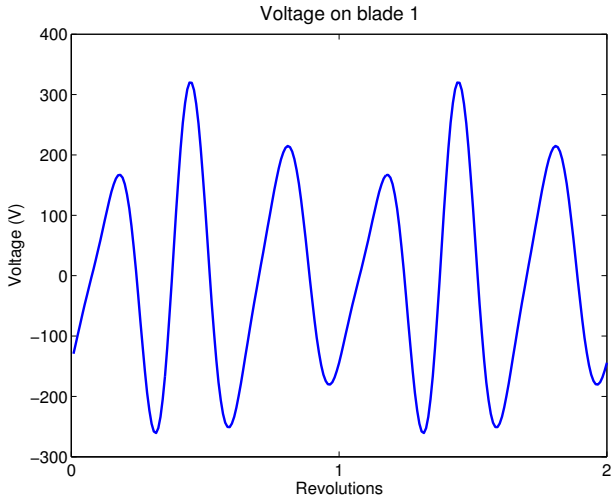

Figure 5.2: Classical adaptive HHC. Applied voltage on blade 1 on the hybrid full potential CFD code.

After having evaluated the capability of the HHC method, the multibody rotor model is coupled with the Free Wake aerodynamic code. The purpose is both to test such controller with a more complex wake modeling including the BVIs and to exploit the constrained HHC version to achieve satisfactory results even if the control signal is limited. The analyzed trim configuration is the same of the previous simulation at an advance parameter of $\mu = 0.23$ *and two different constraints on the actuator harmonic are considered. In the first simulation, the main goal is to verify the reduction capability of the developed quadratic optimization algorithm, while maintaining the applied voltage within acceptable levels; therefore each harmonic of the control signal is limited to a magnitude of* 300 *V. The second simulation is aimed at showing the performance of the proposed HHC method when a strong limit on the actuator is prescribed and each harmonic of the blade voltage is limited to* 100 *V. The alleviation of the* $4/rev$ *loads achieved by both of the simulations with respect to the baseline case is shown in fig. 5.3, while the related control signals are compared in fig. 5.4. Once again the HHC algorithm provide a simultaneous alleviation of the three hub vibrations. In the first simulation, where the control authority is high, a reduction of* 71% *is obtained for the hub shear force* F_Z *and the two hub moments* M_X *and* M_Y *are reduced by* 46% *and* 43%*, respectively. It is very interesting to observe that in the second simulation, in which the signal harmonics are strongly limited, the controller is still able to reduce all the hub loads* $4/rev$ *harmonic. This shows the effectiveness of using an optimization algorithm to handle actuator constraints. In fact while the two hub moments* M_X *and* M_Y *are only reduced by* 11% *and* 17%*, the hub force* F_Z *reduction of* 54% *is very satisfactory considering that the control signal magnitude, shown in fig. 5.4 is much smaller than the one obtained with the first simulation. It is important to notice that the optimization constraints are not violated and that the higher harmonics, the* $8/rev$ *and the* $12/rev$*, are only marginally excited by both of the controller actions. These results are very interesting for practical implementation and experimental analysis, because the actuator saturation can be avoided very safely without losing real time capabilities thanks to the quadratic programming approach and the relaxation of the nonlinear constraints.*

With respect to the other controllers analyzed in this thesis, the HHC algorithms presents some advantages, because it is very easy to be implemented and, if an adaptive version is used, the model of the system is not required. In contrast to the neural network approach, the HHC is based on a quasi-static frequency response model of the helicopter and it can not approximate nonlinear effects. Moreover the control signal is constrained to be composed by the sum of a finite number of harmonics, thus limitating the possibility to generate a more complex signal. Although the HHC has demonstrated to be very effective for this kind of problems, the on-line identification of the rotor response transfer matrix requires several rotor revolutions and the application of random control input that may increase temporarily the rotor vibrations. This issue is avoided if other controllers, for example the periodic ones that are designed after an off-line identification of the system, are used.

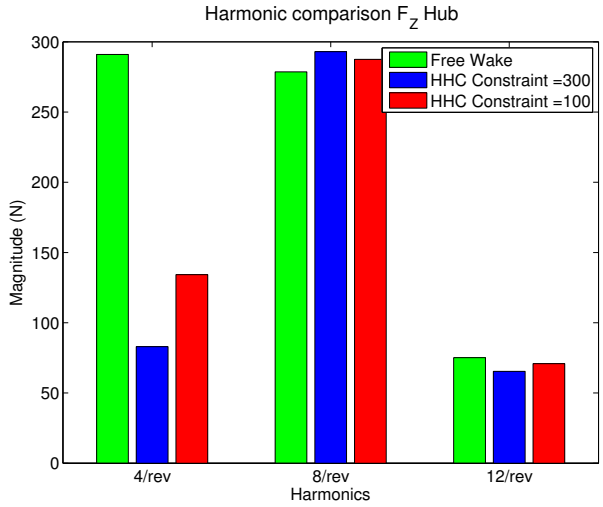

(a) Hub vertical force F_Z.

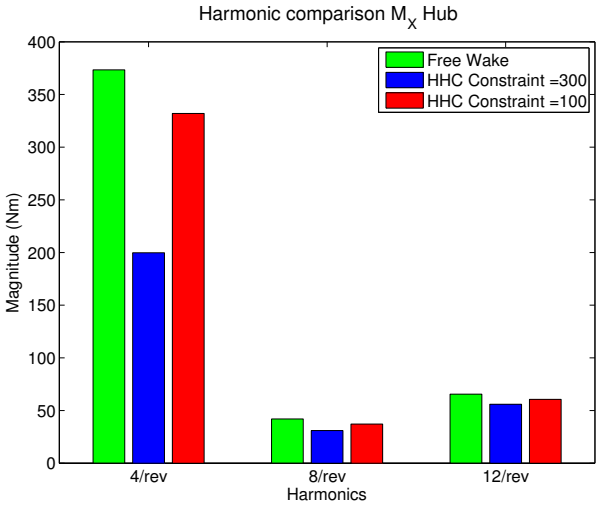

(b) Hub moment M_X.

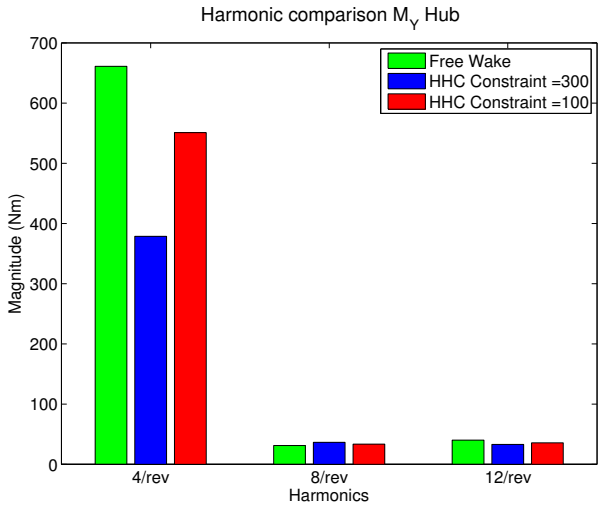

(c) Hub moment M_Y.

Figure 5.3: Adaptive HHC with actuator constraints on the Free Wake model.

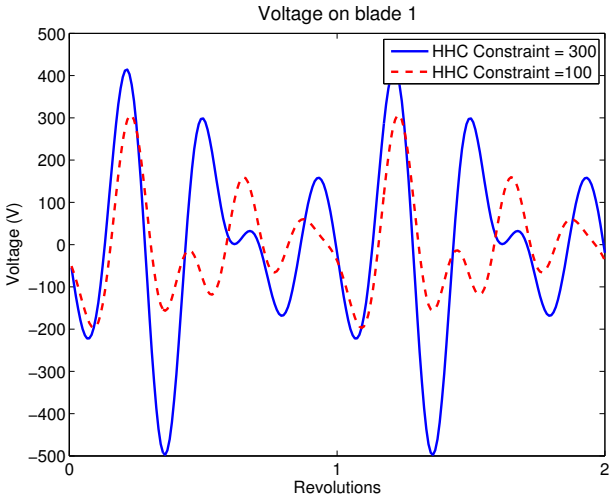

Figure 5.4: Adaptive HHC with actuator constraints. Applied voltage on blade 1 on the Free Wake model.

Part III

Comparison with Different Control Strategies

Chapter 6

Active Trailing Edge Flaps

Until now, we proposed actively twisted blades to perform individual blade control to reduce the vibrations transmitted by the rotor to the fuselage. Even if this solution has demonstrated to be very promising and effective throughout this study, it will become more and more feasible with the future advances of the technology because it involves a quite complex manufacturing of the blade and the application of a rather high electric voltage on the rotating system, which might cause safety problems. Therefore the natural evolution of the vibration reduction study is to investigate other actuation devices in order to understand what could be the most effective solution with respect to the actual technological capabilities of the rotor industry.

The actuators analyzed in this chapter are the trailing edge flaps that are very common in the aerospace field, especially for conventional aircraft, in which they are used to perform attitude flight and active aeroelastic control [160, 182, 183]. In contrast to fixed-wing aircraft, where the ailerons are actuated through hydraulic systems, the actuators of aerodynamic surfaces on rotor blades are usually piezoelectric because of their high bandwidth, crucial to properly generate aerodynamic loads that oppose the vibrations, and the reduced size, very important due to the slender nature of the blade. This approach has been widely investigated in the literature and showed to be very effective for vibrations reduction, however if great deflection angles are required, as in the case of primary rotor control, the friction forces that arise because of the high angular speed play a major role, leading to a degradation of the overall performance [44, 45].

In the present study, we decided to add a single trailing edge flap to the actively twisted blade as shown in fig. 6.1. By doing so, it is possible to build a SMART rotor blade with two actuation systems. Although in this work only the active flaps have been used to suppress helicopter vibrations, having two individual blade control mechanisms on the blade could be very profitable in meeting multiple performance requirements simultaneously, thus facilitating the control problem. For example one could use the distributed piezoelectric actuators to enhance the rotor power performance and the active flaps to suppress vibrations, or it could be possible to use the trailing edge flaps for primary rotor control, hence eliminating the heavy swashplate, and perform the vibration reduction through the actively twisted blades.

After explaining the adopted strategy to model the effects of the active flaps on the blade loads, a closed loop simulation is shown and the results are compared with those obtained by using the active twist rotor in the same trim condition.

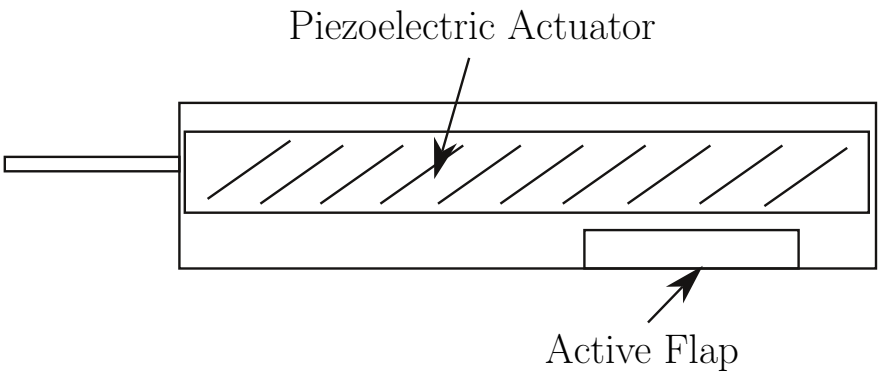

Figure 6.1: Active blade with trailing edge flap.

6.1 Flap Modeling

In this work the modeling of the trailing edge flap does not imply any modification of the structural properties of the blade, and for a preliminary study it is sufficient to consider only the effect of the flap deflection δ on the aerodynamic lift and moment. Therefore, following the blade element method approach, the loads related to the flap deflection have been computed at the airfoil level through the Kussner-Schwarz theory [184], which allows to compute the difference of pressure between the upper and the lower sides of a thin airfoil subject to an unsteady periodic motion including the possibility to modify the shape of the mean line while moving, then the resulting flap related loads are summed to the blade aerodynamic forces. Given a periodic motion of the trailing edge flap only,

$$z = \begin{cases} 0 & x < x_F \\ -(x - x_F)\delta(\omega) & x > x_F \end{cases} \tag{6.1}$$

the lift and moment produced by the airfoil with respect to 25% of the chord c can be computed as

$$\begin{cases} L(\omega) = \frac{1}{2}\rho v^2 c 2\pi \left(C(k)\left(P_0 + P_1\right) + \frac{jk}{2}\left(P_0 + P_2\right)\right)\delta(\omega) \\ M_{\frac{c}{4}}(\omega) = -\rho v^2 \left(\frac{c}{2}\right)^2 \pi \left(P_1 + P_2 + \frac{jk}{2}\left(P_0 - P_2 + \frac{P_1 - P_3}{2}\right)\right)\delta(\omega) \end{cases} = \mathbf{H}_{am}(k)\ \delta(\omega) \tag{6.2}$$

where

$$\begin{gathered} P_0 = \frac{jk}{\pi}\sqrt{1-\widetilde{x}_F^2} + (1 - jk\widetilde{x}_F)\frac{\arccos(\widetilde{x}_F)}{\pi} \\ P_n = \frac{jk}{\pi(n^2-1)}\left(n\widetilde{x}_F sin\left(n\arccos(\widetilde{x}_F)\right) - \sqrt{1-\widetilde{x}_F^2}cos\left(n\arccos(\widetilde{x}_F)\right)\right) + \\ + \frac{1}{n\pi}\left(1 - jk\widetilde{x}_F\right) sin(n\arccos(\widetilde{x}_F)) \end{gathered} \tag{6.3}$$

$C(k)$ is the Theodorsen's lift deficiency function, k is the reduced frequency and $\widetilde{x}_F$ is the position of the aileron hinge divided by the semichord. The adopted notation of the signs of the aerodynamic forces and the flap deflection is shown in fig. 6.2.

Being the aerodynamic transfer function $\mathbf{H}_{am}(k)$ expressed in the frequency domain, the next step is to reformulate the problem into a time domain state form, in order to ease the implementation

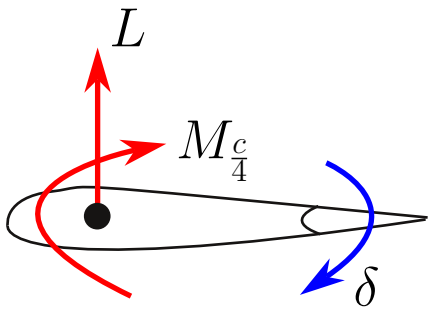

Figure 6.2: Airfoil force notation.

within the aeroelastic rotor simulation toolbox. One of the possible method is to parametrize the transfer function of eq. 6.2 in a Rogers-like formulation

$$\mathbf{H}_{am}(k) \cong \mathbf{D}_{0am} + jk\mathbf{D}_{1am} + (jk)^2\mathbf{D}_{2am} + \sum_{i=1}^{6} \frac{\mathbf{A}_{iam}}{jk + p_i} \tag{6.4}$$

whose unknown matrices $\mathbf{D}_{0am}$, $\mathbf{D}_{1am}$, $\mathbf{D}_{2am}$, $\mathbf{A}_{iam}$ *and poles* p_i *have been identified through a nonlinear least squares optimization, using either the Gauss-Newton or the Levenberg-Marquardt algorithm. Knowing the definition of the reduced frequency* $k = \frac{\omega l_a}{V_\infty}$, *where the reference length* l_a *is the semichord of the airfoil, this formulation can be easily converted into a time dependent state space representation*

$$\begin{aligned} \dot{\mathbf{x}}_a &= -\tfrac{V_\infty}{l_a}\mathbf{A}_a\mathbf{x}_a + \tfrac{V_\infty}{l_a}\mathbf{B}_a\delta(t) \\ \mathbf{f}_a &= \mathbf{D}_{0am}\delta(t) + \tfrac{l_a}{V_\infty}\mathbf{D}_{1am}\dot{\delta}(t) + \left(\tfrac{l_a}{V_\infty}\right)^2\mathbf{D}_{2am}\ddot{\delta}(t) + \mathbf{C}_a\mathbf{x}_a \end{aligned} \tag{6.5}$$

where $\mathbf{f}_a$ *is the vector containing the airfoil lift L and moment* $M_{\frac{c}{4}}$ *and the state space matrices* $\mathbf{A}_a$, $\mathbf{B}_a$ *and* $\mathbf{C}_a$ *are defined as follows*

$$\mathbf{A}_a = \begin{bmatrix} \mathbf{I}p_1 & \mathbf{0} & \cdots \\ \mathbf{0} & \ddots & \mathbf{0} \\ \vdots & \mathbf{0} & \mathbf{I}p_6 \end{bmatrix} \qquad \mathbf{B}_a = \begin{bmatrix} \mathbf{A}_{1am} \\ \vdots \\ \mathbf{A}_{6am} \end{bmatrix}$$

$$\mathbf{C}_a = \begin{bmatrix} \mathbf{I} & \cdots & \mathbf{I} \end{bmatrix}.$$

It is then straightforward to integrate this formulation for the flap loads computation inside the free wake code. The Prandtl-Glauert correction is added to take into account compressibility effects.

6.2 Simulation Results

Starting from the numeric rotor model of the Bo105 with actively twisted blades, a trailing edge flap is added to each blade within the free wake aerodynamic simulation code. The center of the flap is

located at 78.9% *of the blade span and it is* 1.166 *m wide, with the hinge of the flap supposed to be at* 75% *of the blade chord. After having computed the correct aerodynamic transfer function with respect to the flap geometry, the state space model of eq. 6.5 that relates the flap deflection to the generated lift and moment on the airfoil is built and integrated in the rotor simulation toolbox. The trim configuration analyzed by the present simulation is the one at the advance parameter* $\mu = 0.23$.

The rotor vibrations are suppressed using the revised version of the adaptive HHC algorithm including actuator constraints explained in the previous chapter. The objective of the controller is to reduce the $4/rev$ *harmonics of the hub loads* F_Z, M_X *and* M_Y *by applying a control signal with harmonics ranging from the* $2/rev$ *to the* $5/rev$. *In order to avoid an unfeasible great control effort, because of the elevated friction forces, the control inputs have been constrained and each flap deflection harmonic is limited up to* 1°. *The controller weighting matrices* $\mathbf{W}_z$ *and* $\mathbf{W}_\gamma$ *are identity matrices and* $\mathbf{W}_{\triangle\gamma}$ *is the null matrix. The results of the closed loop simulation are shown in fig. 6.3 and they are compared with the vibration reduction study performed using the active twist rotor, in which each harmonic of the control voltage has been constrained below* 300 *V. The solution achieved by the active twist blade design is good, if compared to the baseline loads; the vertical force's* $4/rev$ *harmonic is reduced by* 72% *and the one of the two hub moments* M_X *and* M_Y *is reduced by* 47% *and* 43% *respectively. Even if such a result is quite promising, it can be seen that the trailing edge flap is much more effective in this condition and suppresses almost the* 100% *of the* $4/rev$ *loads. It is interesting to notice that the higher harmonics are only marginally excited by both individual blade control techniques. The required flap deflection is shown in fig. 6.4. As prescribed through the constrained HHC algorithm, the flap angle over the rotor revolution remains very low and it does not exceed* 0.6°.

This analysis has demonstrated the capabilities of the active trailing edge flap system to reduce rotor vibrations as reported in the literature and set the basis for further investigations. In this work we considered only one trim condition and it would be very interesting to see if the flaps are able to suppress the vibrations better than the actively twisted blades throughout the flight envelope. Moreover, the position of the piezoelectric patches for the active twist rotor could be revised and optimized to improve vibration reduction capabilities, since in the present thesis the optimization has been performed on the beam section considering only static requirements.

The study of the vibration reduction capabilities of the actuating mechanism has to be completed by analyzing another important load path that has not been considered in the current simulations. Since the swashplate is represented using two rigid nodes set in motion through file drivers, the loads of the pitch links are not transmitted to the rotor hub and therefore they have not been introduced in the control cost function for vibrations reduction. Although such an approximation does not invalidate the work of this thesis, whose purpose is to analyze the capability to reduce vibrations of both advanced contol systems and different actuators, it is still interesting to investigate at least the effect that the two individual blade control solutions proposed have on the pitch link loads. Figure 6.5 shows the harmonics of the pitch link load for the first blade and a comparison is made among the baseline loads and the modified loads after employing the HHC control, at first using actively twisted blades and then the trailing edge flaps. It can be noticed that, if not properly included in the control cost function, there is the risk that the pitch link related load is increased and this could cause undesirable stresses and fatigue problems for this primary component. Therefore it is very important to consider these loads during the design of a rotor and of a vibration control system. It can be noticed from the harmonic comparison that both the active twist and the active flaps increase the harmonic content of the pitch link load. In paticular, even if the flaps are much more effective for vibration suppression in this flight

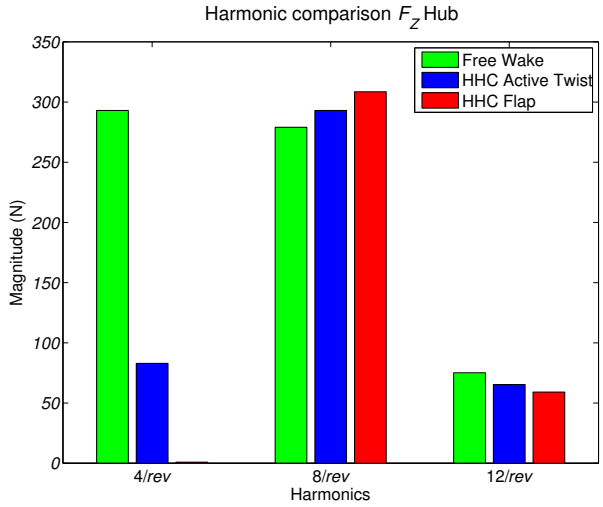

(a) Hub vertical force F_Z.

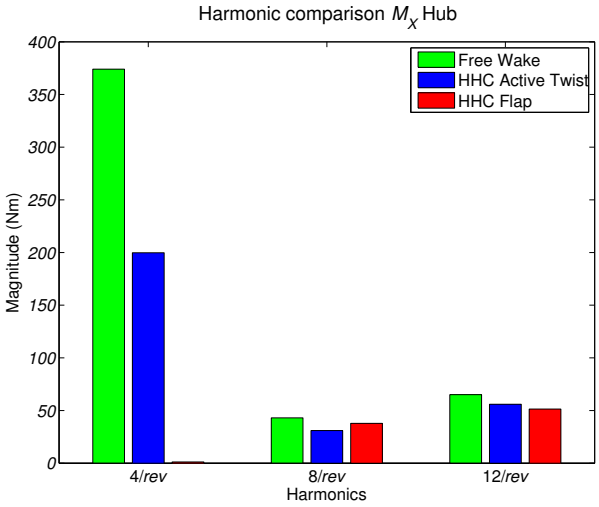

(b) Hub moment M_X.

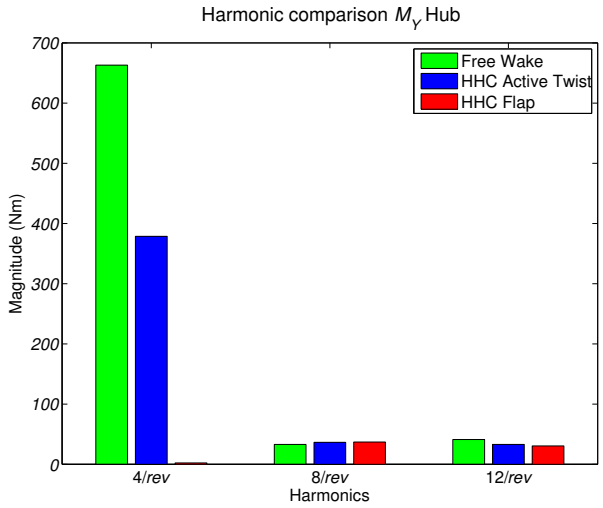

(c) Hub moment M_Y.

Figure 6.3: Vibration suppression using active flaps for the trim condition at $\mu = 0.23$.

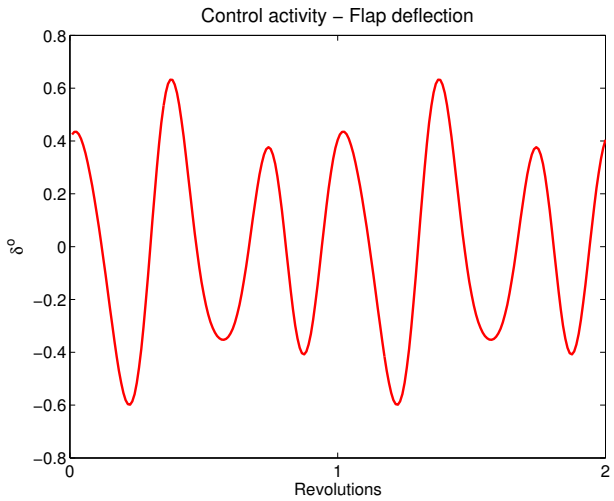

Figure 6.4: Flap deflection signal.

condition, it is not as good for the pitch link. In fact, while the $4/rev$ *harmonic is greatly amplified by both approaches, the trailing edge flaps cause an additional huge increase of the* $2/rev$ *and the* $3/rev$ *harmonics. This investigation about the pitch link loads points out that it is an important load path to be considered in further steps of the rotor design. We are well aware that after this preliminary study of the possible control system architecture, the next step is to consolidate the procedure and validate the vibration controllers including the pitch link loads.*

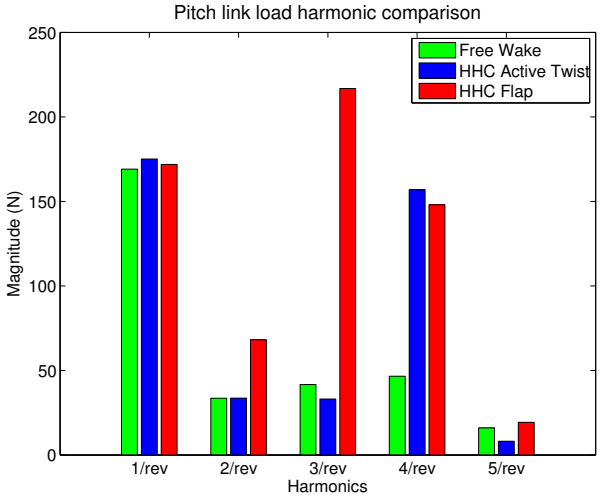

Figure 6.5: Pitch link load analysis for blade 1.

Chapter 7

Multiple Swashplate

The purpose of the following chapter is to present an alternative solution differing from the other ones previously presented. The main characteristics of the individual blade control is the availability of actuators in the rotating frame, thus leading to a more complex manufacture of the blades and to certification problems due to an unconventional rotor design. The strategy reported in this chapter exploits actuators in the nonrotating frame, by enhancing the rotor command chain to allow the possibility of controlling the pitch of each blade independently by using two swashplates.

The multiple swashplate, Mehrfachtaumelscheibe (META) in German, system has been developed and patented in 2008 by the German Aerospace Center (DLR) [185, 186, 187] and exploits the well known and consolidated technology of the swashplate to develop an IBC capable mechanism. The main advantage of using such a device is that only minor modifications are required to the design of the conventional rotor, hence working not far from the standards of the helicopter industry. Therefore the certification of this system for modern helicopters should be easier, since it is possible to ensure a higher level of safety if compared to other IBC mechanisms.

After explaining the basic operating principles and the method to control the multiple swashplate, this chapter presents an experimental activity performed at the DLR during my PhD leave abroad aimed at testing the IBC capabilities of the META system for the blade tracking control problem.

7.1 Operating Principles

The multiple swashplate system is aimed at overcoming the limitations of the classical HHC performed with a single swashplate. It achieves full individual blade control capabilities without using actuators in the rotating frame. The basic idea of this control mechanism derives from the assumption that a single swashplate is able to control up to 3 *blades independently. Therefore for helicopters with four to six blades, a second swashplate is sufficient in providing a full IBC capable system. The META concept has the advantage that the rotor can still be designed conventionally and being the swashplate a well known system, the costs for maintenance do not increase significantly compared to conventional rotors without IBC capability. An example of the META control system for a 6 blades rotor is shown in fig. 7.1. It can be clearly seen that three blades are connected to the inner swashplate and three blades to the outer one. As in conventional rotors, the architecture of the single swashplate is not modified and the collective and cyclic control is performed through three electro-hydraulic actuators*

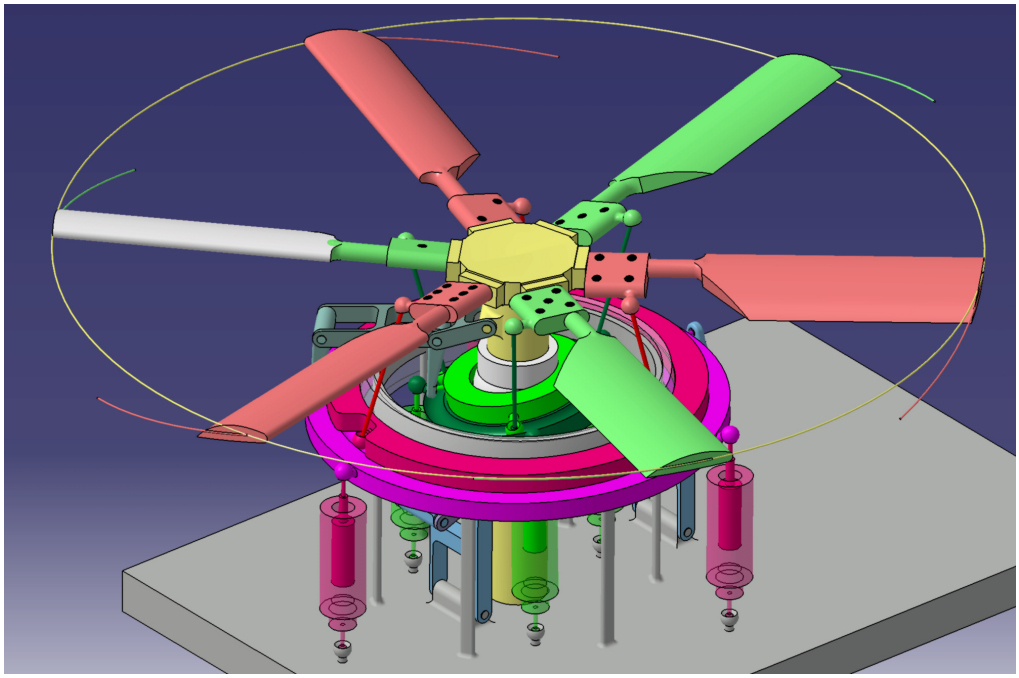

Figure 7.1: Multiple swashplate mechanism.

in the nonrotating frame.

In contrast to IBC approaches using actuator in the rotating frame, all control signals with the META system are generated in the nonrotating frame and then transmitted to the blades through the swashplate. Therefore, the determination of a relationship among the electro-hydraulic actuators and the blade pitch is necessary. Starting from the definition of the blade pitch as a Fourier series with a certain number of harmonic N_{harm} in the rotating frame

$$\vartheta_p(t) = \vartheta_0 + \sum_{n=1}^{N_{harm}} (\vartheta_{nc} cos(n\psi_p) + \vartheta_{ns} sin(n\psi_p)) \tag{7.1}$$

where p is the blade index and ψ_p is the blade azimuthal angle, it is possible to write a generalized control law for the swashplate in the nonrotating frame by using the multiblade coordinate transformation, as described in [188]

$$\theta = \theta_0 + \sum_{n=1}^{N_{harm}} (\theta_{nc} cos(\psi) + \theta_{ns} sin(\psi)) + \theta_2 \tag{7.2}$$

where the coefficients of the Fourier series are computed by the pitch angles in the rotating frame as follows

$$\theta_0 = \frac{1}{N} \sum_{p=1}^{N_p} \vartheta_p(t) \tag{7.3}$$

$$\theta_{nc} = \frac{2}{N} \sum_{p=1}^{N_p} \vartheta_p(t) cos(n\psi_p) \tag{7.4}$$

$$\theta_{ns} = \frac{2}{N}\sum_{p=1}^{N_p} \vartheta_p(t)\, sin(n\psi_p) \tag{7.5}$$

$$\theta_{\frac{N}{2}} = \frac{1}{N}\sum_{p=1}^{N_p} \vartheta_p(t)\,(-1)^p\,. \tag{7.6}$$

The so called reactionless mode $\theta_{\frac{N}{2}}$ occurs only on rotors with more than 3 blades and an even number of blades. Therefore, having up to 3 blades per swashplate, it is possible to transmit all rotor harmonics to the rotating frame. Moreover, the full IBC capability is given by the fact that the number of the blades is equal to the three degree of freedom of the swashplate.

The rotor control law of eq. 7.2 can not be directly employed to individually command the blades and a further step is needed to connect the values of the Fourier coefficients to the length of the actuators that is required for a proper motion of the swashplate. Supposing that a maximum of three blades can be connected to a single swashplate, the following discussion has to be repeated for the second swashplate as well. A first method could be to solve the kinematic path between the time dependent blade pitch angle and the position of the swashplate. Since the analytical formulation is quite complex to be solved, it would be rather time consuming for real time implementation, therefore an approximate method is preferred. For this reason it is necessary to simplify the computation of the required actuators lengths and use a transformation matrix $\mathbf{M}$ that relates the control input vector θ with the actuators position $\mathbf{l}_S$, thus developing a suitable control law for the swashplate

$$\mathbf{l}_S = \mathbf{M}\theta + \mathbf{l}_{S_{ref}}. \tag{7.7}$$

The vector θ comprises the rotor control coefficients θ_0, θ_c and θ_s and the vector $\mathbf{l}_{S_{ref}}$ contains the reference lengths of the three actuators in the neutral position. In order to compute this matrix, several measures of the rotor trim state are needed. The constant Fourier coefficients θ_0, θ_c and θ_s of the primary rotor control are then related to the corresponding constant actuator lengths. By doing so it is possible to approximate the kinematic path either through a linear expression, leading to a constant 3x3 matrix for each swashplate, or by using a polynomial expression for the matrix $\mathbf{M}$ up to the 5th order of the control coefficients as shown in [185, 186]. Once the swashplate control law of eq. 7.7 has been determined from the rotor primary control, it is possible to superimpose the higher harmonic content of the IBC commands. Following eqs. 7.3-7.5 it is possible to transform the higher harmonics of the blade pitch into time dependent Fourier coefficients in the nonrotating frame and then they are added to those of the primary control

$$\theta = \theta_{Primary} + \theta_{IBC}$$

leading to time variant actuator lengths through eq. 7.7.

Thanks to the IBC capability, the applications of this actuating system are many. One of the goal of the META project was to investigate the feasibility of splitting the tip path plane of the rotor through IBC control [186]. This would be very important for reducing the effects of the BVIs because it is possible to generate vertically spaced blade tip vortices with a consequent reduction of the BVI noise. The individual blade pitch control can also be used to perform vibration reduction studies as well as blade tracking control. This last application will be described in the following section.

7.2 Tracking Control in Hover

In this section, the problem of blade tracking control in hover is analyzed. In the numerical models of helicopter rotors, the loads transmitted by the blades to the hub are composed only by harmonics that are multiple of the number of the rotor blades multiplied by the rotor rotational frequency. Due to the manufacturing technology, it is obvious that the blades, as well as the connections such as the pitch links and the pitch horns, are designed to be as similar as possible, but they still present some differences. Therefore in real applications the rotor hub is subjected to loads that contains all harmonics multiples of the $1/rev$*, because the blade dissimilarities do not cancel the periodic loads as expected in the ideal numerical world. The basic idea of the blade tracking control is to actively control the blade pitch in order to eliminate the effects of these dissimilarities by artificially making the blades behave in the same manner.*

The work reported here is based on an experimental activity performed at the DLR during my PhD study, more details on this study can be found in [181]. An experimental rotor model of the Hart II rotor is equipped with the META actuating mechanism, shown in fig. 7.2, to carry out IBC tests and verify the capabilities of this system. Since the Hart II is a 4 blades rotor, two swashplates are needed and each swashplate is connected to two blades. During May 2015 the META system has been tested to perform tracking control in the DLR's rotor testing hall in hovering condition. The idea of this study is to independently modify the mean value of the blade pitch ϑ_0 *to reduce the* $1/rev$ *hub loads due to the rotor imbalances through the HHC algorithm modified to include actuator constraints described in the previous chapter.*

The primary rotor controls (collective and dynamic pitch) of META are set by the test operator at the piloting rack for both swashplates simultaneously using comparatively slow, but highly accurate electric motors controlled by Easy to use Positioning System (EPOS) -modules, which are part of the META actuation system. The second, hydraulic part of the actuation system, which has less control authority but is capable of moving with frequencies up to 100 Hz, is needed to realize the dynamic blade control signals for HHC, IBC and in-flight blade tracking. The control software for these hydraulic actuators runs independently on a dedicated dSPACE real-time processor (RTP) and can be accessed through a graphical user interface (GUI), running on a separate display PC. Signal measurement and recording is handled by the DLR's own second generation Transputer-based extendible data acquisition system (TEDAS II), which is capable of recording up to 250 channels at sampling rates of $2048/rev$*. The control software for the META system is compiled from a Simulink model using the Matlab/Simulink compiler and then distributed among the four individual cores of the processor used in the RTP-unit. The cores are assigned the following dedicated tasks:*

- ***core 1****: calculation of IBC signals and conversion to actuator strokes;*
- ***core 2****: hydraulic actuator piston position control, measurement and signal routing;*
- ***core 3****: dedicated (otherwise inaccessible) core for network communications;*
- ***core 4****: miscellaneous.*

Since they are directly tied into the rotor control system, cores no. 1 and 2 have to run at a frequency equal to $256/rev$ *(*4.48 *kHz) synchronously to the model rotor in order to ensure correct phase settings for the control signals. This is achieved via an external trigger signal from the RTR's azimuthal pulse*

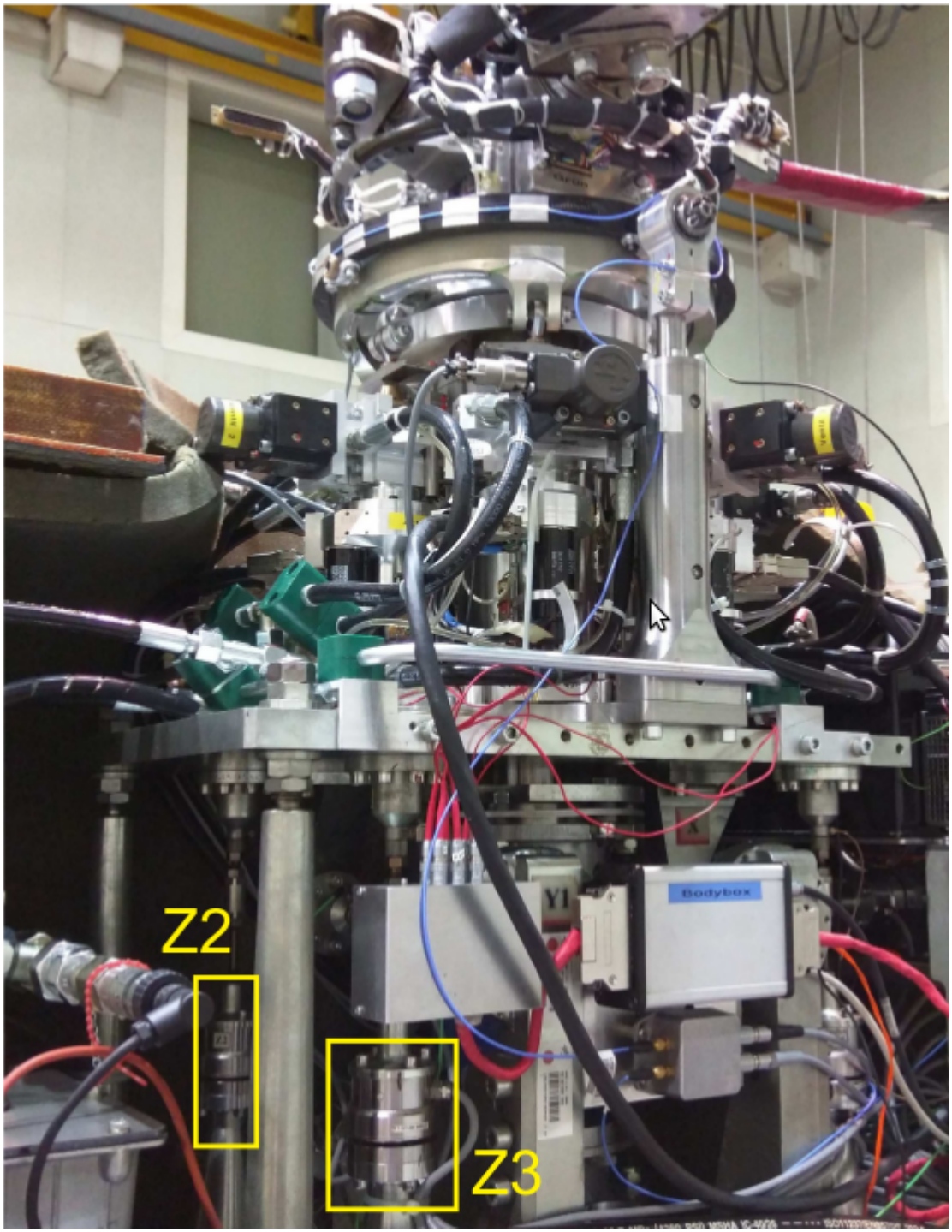

Figure 7.2: Tracking control experiment. Measure points.

synchronizer (APS). Due to the relatively high sampling rate and the complexity of the tasks, those two cores have little margin with regards to task execution time, and were thus deemed unsuitable for the addition of more functionality. Cores no. 3 and 4 run largely independently and can be set to any arbitrary sampling rate best suited for the assigned task. In order to decouple the task of vibration control from the most computationally demanding functions and to avoid issues with synchronization or task execution times the HHC control algorithm was integrated to run solely on core no. 4 with a base sampling rate of $400\ \mu s$ *(*$2500\ Hz$*).*

To allow enough time for transients to settle down after changing the control signals, an identification step is only triggered if at least one second (or 17.5 *rotor revolutions) has passed and the dynamic response of the rotor system has stabilized. The identification cycle is programmed to operate automatically, as soon as an identification step is finished, a new set of randomly generated control signals is calculated and realized by the META system. Once the transients have died out, a new identification step is triggered and the cycle continues until stopped manually. Once the transfer matrix* $\mathbf{T}$ *is fully identified, it can then be stored on hard disk and, if necessary, reloaded into the control software. For controller operation, the identified transfer matrix is then passed, along with the current control inputs, to the HHC algorithm. The amplitude limits for HHC operation or maximum collective offsets can be set by the user prior to each controller run. Since the HHC algorithm itself includes optimization loops and thus can differ in execution time, an internal rate transition was introduced into the Simulink model in order to allow enough time for the full and successful execution of the algorithm. First simulations showed that a maximum execution time of five seconds (*≈ 90 *rotor revolutions) is suitable for controller operation and offers a large execution time margin in case of possible deviations. When an optimization run is finished, the calculated control coefficients are manually adopted by the user and passed on to the META control task, which then synthesizes the corresponding blade control signals and drives the hydraulic actuators accordingly. This semi-closed loop approach was selected to ensure the safe operation of the experimental model.*

7.2.1 Experimental Results

The test is carried out at a reduced thrust of $1500\ N$ *in hover and 4 vertical Z force transducer are used at the bottom of the rotor test rig, as shown in fig. 7.2. For the* $\mathbf{T}$ *matrix identification, random blade offsets (within the predetermined controller limits of* 0.3^o*) were automatically introduced into the system to produce and measure a corresponding change in rotor imbalance necessary for the identification process. The transfer* $\mathbf{T}$ *is a* 8×4 *matrix (four blade offsets, eight 1/rev coefficients for four Z-force transducers). After 10 consecutive random identification steps, the only partly populated transfer matrix was assumed to be identified with sufficient accuracy and saved to hard disk. In the next step, all dynamic actuator input were set so zero and the HHC algorithm was activated. After each completion of the algorithm the proposed individual blade offsets were displayed in the GUI and then manually adopted and applied to the META system. While a total elimination of the rotor imbalance was impossible due to recirculation occurring in the closed space of the test hall, a reduction of the* $1/rev$ *Z-forces measured by the rotor balance to* 8.66% *of the baseline level was achieved after four consecutive controller runs. Figure 7.3 shows both part of the identification process as well as the four controller steps leading to the final control solution. Each point in the plot represents the average* $1/rev$ *vibration component of Z-forces measured by the four sensors on the rotor balance for one set of individual blade offsets. The final blade pitch offsets that allow the minimization of* $1/rev$ *vibratory*

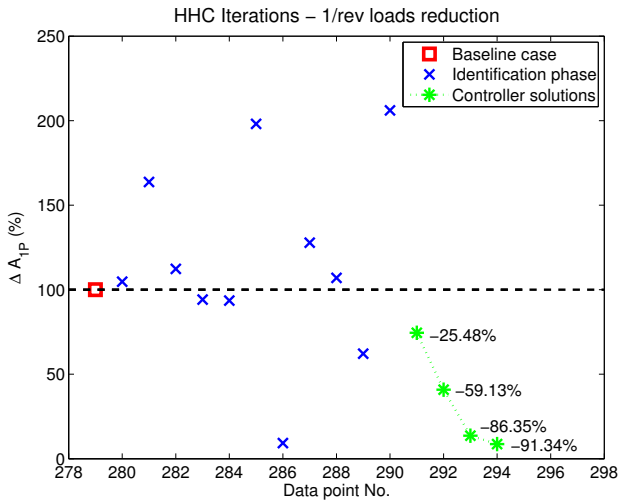

Figure 7.3: Minimization of the $1/rev$ hub loads through the blade tracking control.

Table 7.1: Pitch control offsets.

Blade	$\triangle\vartheta_0$deg
1	$+0.31^o$
2	$+0.03^o$
3	-0.07^o
4	$+0.33^o$

Z-forces are summarized in tab. 7.1.

Although the vibratory loads have been minimized, the individual blade offsets led to a net increase in rotor thrust of 115 *N (7.7%). The severity of the rotor imbalances partly depends on rotor thrust and this effect can bias the results in either direction. To prevent, or at least mitigate this effect in the future, a feed-forward thrust compensation has been added within the control software, automatically lowering the collective pitch setting by the mean value of the individual blade offsets. With the thrust compensation enabled, a second test was performed, again at a reduced thrust setting of* 1500 *N and with blade offsets limited to a maximum of* 0.3^o*. After the initial identification phase using random inputs, the controller algorithm was able to reduce* $1/rev$ *Z-forces by* 87.4% *after the first step, with a final reduction of* 94.2% *after three controller runs. The individual blade offsets measured during the third controller run are listed in tab. 7.2. The sum of all individual blade offsets in this case equals zero, thus keeping the thrust substantially constant during the test without need for further manual inputs by the operator. Accordingly the maximum thrust offset during the application of the last controller solution was measured at* -11.8 *N, equaling less than* 1% *of baseline thrust.*

The next step of this study will be to carry out vibration reduction in forward flight and to investigate various different flight conditions. Based on the simulation results and also the successful test of the in-flight tracking mode of the controller, the algorithm is expected to perform as planned in HHC-tests during the upcoming windtunnel campaign.

Table 7.2: Pitch control offsets with equalized thrust.

Blade	$\triangle\vartheta_0$deg
1	$+0.15^o$
2	-0.18^o
3	-0.18^o
4	$+0.21^o$

Concluding Remarks and Future Works

Helicopter rotor blades in forward flight experience a highly complex aerodynamic environment, which can be the source of many problems, such as dangerous vibrations and noise for structural integrity and passengers comfort. These complicated aerodynamic phenomena, which are mainly related to dynamic stall, shock waves and blade vortex interactions, couple with the elastic motion of the blades, causing fluctuating aeroelastic loads that are very difficult to predict through numerical softwares in the preliminary design phase. Therefore one of the contribution of this thesis is the development of an aeroservoelastic rotor simulation toolbox that allows to carry out accurate simulations with a limited computational effort at an early stage of rotor design. Therefore the work aims at studying vibratory loads reduction, one of the main issue for helicopters in forward flight, by employing several advanced active control strategies that are usually implemented for simple and academic problems. The study has focused on the main rotor only because it is the prime source of vibrations. Since the purpose of this work is to study advanced active control systems, almost the entire thesis exploits an active twist rotor as test case, leaving to the last two chapters the comparison with different devices associated to individual blade control, such as the active trailing edge flaps and the multiple swashplate. The concluding remarks and the main findings of this thesis are detailed below.

In the first chapter an improved general new method for modeling anisotropic, straight and linear beam sections with embedded piezoelectric devices is presented. The stiffness matrix per unit length of the beam is correctly evaluated by accounting for a completely coupled three-dimensional piezoelectric constitutive law. To do so, the solutions related to the the so-called de Saint-Venant's concept are considered along with a set of particular solutions obtained by independently loading the beam piezoelectric patches with an electric potential. The new formulation does not require any redundant assumption, thus allowing to straightforwardly develop the related model and to compute the generalized constitutive law of a beam section. No asymptotic expansion is required, so that the obtained results remain valid independently from the beam slenderness. The proposed approach is validated through three-dimensional finite element models and similar semi-analytical methods showing a high level of accuracy. This formulation is then extended to include the modeling of piezomagnetic beams and the code is validated with a simple example and a two-dimensional boundary element method presented in the literature. This approach limits the application of the finite element method to the beam section only for the section properties computation and the resulting stiffness matrix can then be used within more complex structural codes, without the need of a complex full three-dimensional finite element model. Further validation analysis with experimental data or three-dimensional models are needed for the piezomagnetic beam model formulation. After that, a multibody active twist rotor model is built as test case for the vibration control study, starting from a numeric model of the Bo105.

The study of the helicopter vibrations is a very demanding task and requires an accurate model-

ing of the aerodynamic phenomena, which can not be represented properly if considering the simple aerodynamic theories provided by the multibody software. Since the use of CFD codes for the whole rotor is prohibitive in terms of computational time for the iterative design of active vibration control systems, there is the need of a new strategy that provides an intermediate level of fidelity to model the main effects of the rotor behavior in forward flight. In the second chapter of the thesis, the hybrid modeling approach is exploited, in which the blade aerodynamics and the rotor wake are modeled using different techniques, and two aerodynamic codes have been developed in this work and validated with the experimental data of the Hart II rotor:

- *Full potential CFD and Peters-He wake model. In the related first trial, more attention is given to the blade aerodynamics and a full potential CFD code is used to approximate the unsteady and compressibility effects of the blade loads. The Peters-He generalized wake model is coupled to such a CFD code to enhance the harmonic content of the rotor inflow without physically simulating the wake, thus being beneficial for the overall computational time. Even if this approach is very accurate for the advancing blade aerodynamics and can also reproduce shock waves, it has some limitations. First of all, the reverse flow condition cannot be simulated, because of the fixed wake structure of the potential approach. Moreover, blade vortex interactions are not taken into account, since the wake is not directly modeled. This leads to an underestimation of the blade loads, especially for the* $4/rev$ *harmonic.*

- *Unsteady blade element method and free wake of the tip vortices. After evaluating the limitations of the previous hybrid CFD code, a deeper consideration is given to the modeling of the wake, while relaxing the near field aerodynamic approximation. In this hybrid code, the blade aerodynamics is approximated with an unsteady blade element theory and the free wake geometry of the tip vortices only, the most relevant ones, is computed. Having modeled the rotor wake, the advantage of this code is the possibility to simulate blade vortex interactions, hence leading to a more realistic loads estimate. Although the unsteady blade element method combined with the coefficient data of the airfoil and the tip loss correction provides a good approximation of the blade loads, shock waves and dynamic stall can not be taken into account by this formulation. Although increasing the simulation time, this code can be enhanced by introducing the free wake of the root vortices.*

Being available an adequate low fidelity model of the rotor, based on the multibody approximation with integrated simple aerodynamics, and an intermediate fidelity one, obtained by coupling the multibody software to one of the two hybrid aerodynamic codes above, from the third to the fifth chapter this work proceeds with the study and design of vibration controllers. The purpose is to analyze advanced active control strategies and to adapt them to the problem of vibrations suppression. The contribution of this work is the application of different control systems to very complex and nonlinear examples, aiming at reproducing actual flight situations. It is also very important to consider that all the controllers considered in this thesis possess real time capabilities, thus being employable into real tests. The main findings of the studied controllers are listed below.

- *Periodic controllers. The main advantage of the periodic controllers is the possibility to take into account the periodicity of the rotor during the design phase. Two different periodic controllers have been analyzed, at first a dynamic compensator full information* H_2 *controller is*

designed and then it has been compared to the solution obtained through the static output feedback one. The design model shows a significant vibratory loads reduction with a small control effort. Furthermore, the performance of the two periodic controllers seem to be similar. This means that the direct periodic output feedback, which involves fewer design parameters, has a faster design algorithm and is easier to be realized, can be a valid substitute of the optimal H_2 approach. Moreover, using only an algebraic gain matrix in the control law would allow to cover all the flight envelope by simply interpolating, with a gain scheduling technique, the gain matrices, avoiding the problems that could arise when interpolating state space models [154, 155]. The validation model, with the free wake aerodynamic code, shows that taking into account the periodicity of the rotor in forward flight leads to robust controllers, even if model uncertainties are not considered in the design phase. In fact, there is no spillover, and both controllers manage a vibratory loads reduction with satisfactory performance, a promising result for a practical implementation. The disadvantage of using periodic controllers is that their design is carried out off-line on linearized identified periodic models that have to correctly represent the real system.

- *Recurrent neural networks controller. A recurrent neural network based nonlinear adaptive controller has been investigated for complex aeroelastic problems and adapted to the problem of rotor vibrations reduction. Thanks to its general formulation and to the black-box approach, it can be easily employed in a large class of problems. The examples in this work show the RNN control capability to improve helicopter performance. Very good results are obtained in the vibration study and, due to the on-line learning feature of this controller, the validation based on the high fidelity free wake model exhibits good performance. Despite the potential of using a neural network approach, the choice of the controller parameters, such as the number of neurons and the learning rate, is not trivial and the search for a general rule remains an open problem. When considering a practical implementation of such a well performing controller, these issues should be carefully addressed as well as network saturation problems.*

- *Improved higher harmonic control with actuator constraints. The last control system studied is already used in helicopter applications, because of its simplicity and robustness. It is here improved to avoid actuator saturations, which is one of the main problems for its practical adoption. Therefore, the control effort limitations are included through an optimization, constraining each harmonic of the signal, in such a way to be easily amenable to an efficient quadratic programming approach. As the neural network approach, the HHC algorithm is adaptive and does not require the previous knowledge of the system to be controlled. Thanks to the actuator constraints, it is possible to safely guarantee that the control signals remain within desired and acceptable levels. The application of this controller to the aeroelastic rotor model shows its potential and effectiveness in vibrations reduction, nevertheless this approach has some limitations. First of all, even if the model is identified on-line, it is based on a quasi-static linear response of the rotor. Second, the computed control signal has a limited and imposed harmonic content, therefore it is not possible to generate an arbitrary, more versatile, signal. Another disadvantage of this approach is that the first time steps of the controllers run are used to identify the transfer matrix of the rotor response through random control input that could temporarily increase the vibratory loads. An alternative, to avoid this issue, could be the off-line identification of the rotor transfer matrix for a set of operating conditions and then the application of a*

gain scheduling technique to interpolate the rotor transfer matrix.

Once the control design study has been concluded, the thesis moves into the investigation of different architectures apt to individual blade control and in the sixth chapter the active twist solution is compared with active trailing edge flaps. Since they are already used in fixed-wing aircraft, active flaps are more conventional than distributed piezoelectric actuators. Therefore they are widely presented in the literature because of their effectiveness. Such a comparison shows that active flaps are able to totally suppress the hub vibrations. We are aware that only static constraints have been used to optimize the active twist blade in order to maximize the actuation power, therefore a deeper study and a new optimization has to be carried out to investigate whether the active blade twist can achieve the same results as the active flaps and if the active flaps are very effective in all flight conditions.

The final chapter is related to the experimental activity performed at the German Aerospace Center, in which the multiple swashplate system is studied. The analysis focused on the IBC capabilities of the META system. This work is very important because the HHC control with actuator constraints has been implemented and tested within the real time environment on an experimental rotor model, showing very good results for the blade tracking control in hover. The next steps of this work have to be developed in the wind tunnel, to test the vibration reduction capabilities of the META system in forward flight.

To conclude, this thesis spans a wide range of topics from the aeroservoelastic rotor modeling to advanced control systems design. The main objective of this work is to set the basis for a more accurate analysis aimed at investigating and validating the obtained results. Since the pitch link loads have not been considered into the control cost function, the first step to improve this work could be to repeat the controllers design including these loads. Afterward, it would be interesting to focus on a single IBC approach and to perform a vibration reduction analysis for the whole flight envelope, either through a gain scheduling technique or through an adaptive controller, to further investigate which controller can achieve the best performance over a significant flight envelope.

Bibliography

[1] J. Leishman. Principles of Helicopter Aerodynamics. *Cambridge Aerospace Series, 2001.*

[2] A. R. S. Bramwell, G. Done, and D. Balmford. Bramwell's Helicopter Dynamics. *Elsevier, 2000.*

[3] A. C. Veca. Vibration nalysis of the sa349/2 helicopter. NASA, Technical Memorandum 102794*, 1991.*

[4] A. C. Veca. Vibration effects on helicopter reliability and maintainability. Sikorsky Aircraft Division, AD-766 307*, April 1973.*

[5] Nagarajan Hariharan and J. Gordon Leishman. Unsteady aerodynamics of a flapped airfoil in subsonic flow by indicial concepts. Amerian Institute of Aeronautics and Astronautics*, 1995.*

[6] C. Venkatesan and P. Friedmann. New approach to finite-state modeling of unsteady aerodynamics. AIAA Journal*, 24(12):1889–1897, 1996.*

[7] David A. Peters, Mong che A. Hsieh, and Almudena Torrero. A state-space airloads theory for flexible airfoils. American Helicopter Society 62th Annual Forum, Phoenix, AZ*, May 9-11 2006.*

[8] Timothy F. Myrtle and Peretz P. Friedmann. Unsteady compressible aerodynamics of a flapped airfoil with application to helicopter vibration reduction. Amerian Institute of Aeronautics and Astronautics*, 1997.*

[9] Timothy F. Myrtle and Peretz P. Friedmann. Application of a new compressible time domain aerodynamic model to vibration reduction in helicopters using an actively controlled flap. 24th European Rotorcraft Forum, Marseilles, France*, September 15-17 1998.*

[10] M. de Terlizzi and Peretz P. Friedmann. Active control of bvi induced vibrations using a refined aerodynamic model and experimental correlation. American Helicopter Society 55th Annual Forum, Montreal, Canada*, May 25-27 1999.*

[11] Dale M. Pitt and David A. Peters. Theoretical prediction of dynamic-inflow derivatives. 6th European Rotorcraft and Powered Lift Aircraft Forum, Bristol, England, 16-19 September*, 1980.*

[12] David A. Peters and Chen Jian He. Correlation of measured induced velocities with a finite-state wake model. 45th Annual National Forum of the American Helicopter Society, Boston, Mass.*, May 1989.*

[13] Carlos A. Malpica. Contributions to the dynamics of helicopters with active rotor controls. PhD Thesis, Department of Aerospace Engineering, University of Maryland*, 2008.*

[14] Judah Milgram Inderjit Chopra. Helicopter vibration reduction with trailing edge flaps. 36th AIAA/ASME/ASCE/AHS/ASC Structures, Structural Dynamics, and Materials Conference, New Orleans, LA*, April 10-12, 1995.*

[15] Michael G. Spencer, Robert M. Sanner, and Inderjit Chopra. Adaptive neurocontrol of simulated rotor vibrations using trailing edge flaps. Journal of Intelligent material Systems and Structures*, 10, November 1999.*

[16] Jun-Sik Kim. Design and analysis of rotor systems with multiple trailing edge flaps and resonant actuators. PhD Thesis, The Pennsylvania State University*, 2005.*

[17] T. A. Millott and P. P. Friedmann. Vibration reduction in helicopter rotors using an actively controlled partial span trailing edge flap located on the blade. NASA Technical Report 4611*, June 1994.*

[18] Judah Milgram, Inderjit Chopra, and Friedrich Straub. Rotors with trailing edge flaps: Analysis and comparison with experimental data. Journal of the American Helicopter Society*, 43(4):319–332, October 1998.*

[19] Shrinvas R. Bhat and Ranjan Ganguli. Validation of comprehensive helicopter aeroelastic analysis with experimental data. Defence Science Journal*, 54(4):419–427, October 2004.*

[20] Inderjit Chopra. Review of state of art of smart structures and integrated systems. AIAA Journal*, 40(11), November 2002.*

[21] G. Alvin Pierce, M-Nabil, and H. Hamouda. Helicopter vibration suppression using simple pendulum absorbers on the rotor blade. NASA, Technical Report 3619*, 1982.*

[22] Richard Bielawa. Analytic investigation of helicopter rotor blade appended aeroelastic devices. NASA, Technical Report 166525*, 1984.*

[23] R. G. Loewy. Helicopter vibrations: A technological perspective. Journal of American Helicopter Society*, 29(4):4–30, 1984.*

[24] Judah Milgram, Inderjit Chopra, and Sesi Kottapalli. Dynamically tuned blade pitch links for vibration reduction. American Helicopter Society 50th Annual Forum, Washington, DC*, May 11-13 1994.*

[25] P. P. Friedmann. Helicopter vibration reduction using structural optimization with aeroelastic/multidisciplinary constraints. Journal of Aircraft*, 28(1):8–21, 1991.*

[26] Ranjan Ganguli. Survey of recent developments in rotorcraft design optimization. Journal of Aircraft*, 41(3), May-June 2004.*

[27] Khanh Q. Nguyen. Higher harmonic control analysis for vibration reduction of helicopter rotor systems. NASA Technical Memorandum 103855*, 1994.*

[28] Khanh Nguyen and Inderjit Chopra. Application f higher harmonic control to hingeless rotor system. NASA Technical Memorandum 103846*, 1991.*

[29] P. P. Friedmann and T. A. Millot. Vibration reduction in rotorcraft using active control: A comparison of various approaches. Journal of Guidance, Control and Dynamics*, 18(4):664–673, 1995.*

[30] Ch. Kessler. Active rotor control for helicopters: motivation and survey on higher harmonic control. CEAS Aeronautical Journal*, 1:3–22, 2011.*

[31] Ch. Kessler. Active rotor control for helicopters: individual blade control and swashplateless rotor designs. CAES Aeronautical Journal*, 1:23–54, 2011.*

[32] A. Mander, D. Feszty, and F. Nitzsche. Active pitch link actuator for impedance control of helicopter vibration. American Helicopter Society 64th Annual Forum*, 2008.*

[33] Prashant M Pawar and Sung Nam Jung. Active twist control methodology for vibration reduction of a hhelicopter with dissimilar rotor system. Smart Materials and Structures*, 18, 2009.*

[34] Matthias Althoff, Mayuresh J. Patil, and Johannes P. Traugott. Nonlinear modeling and control design of active helicopter blades. Journal of the American Helicopter Society*, 57, 2012.*

[35] Matthew L. Wilbur and W. Keats Wilkie. Active-twist rotor control applications for uavs. 24th US Army Science Conference*, 2004.*

[36] Hans Peter Monner, Johannes Riemenschneider, Steffen Opitz, and Martin Schulz. Development of active twist rotors at the german aerospace center (dlr). American Institute of Aeronautics and Astronautics*, 2011.*

[37] Johannes Riemenschneider and Steffen Opitz. Measurement of twist deflection in active twist rotor. Aerospace Science and Technology*, 15:216–223, 2011.*

[38] Matthew L. Wilbur, Paul H. Mirick, William T. Yeager Jr., Chester W. Langston, Carlos E. S. Censik, and SangJoon Shin. Vibratory loads reduction testing of the nasa/army/mit active twist rotor. American Helicopter Society 57th Annual Forum, Washington, DC*, May 9-11 2001.*

[39] Earl R. Booth Jr. and Matthew L. Wilbur. Acoustic aspects of active-twist rotor control. American Helicopter Society 58th Annual Forum, Montreal, Canada*, June 11-13 2002.*

[40] Nikhil A. Koratkar and Inderjit Chopra. Wind tunnel testing of a mach-scaled rotor model with trailing-edge flaps. Smart Materials and Structures*, 10:1–14, 2001.*

[41] In-Gyu Lim and In Lee. Aeroelastic analysis of rotor systems using trailing edge flaps. Journal of Sound and Vibration*, 321:525–536, 2009.*

[42] *Sathyamangalam Ramanarayanan Viswamurthy and Ranjan Ganguli. An optimization approach to vibration reduction in helicopter rotors with multiple active trailing edge flaps.* Aerospace Science and Technology*, 8:185–194, 2004.*

[43] *P. P. Friedmann, M. De Terlizzi, and T. F. Myrtle. New developments in vibration reduction with actively controlled trailing edge flaps.* Mathematical and Computer Modeling*, 33:1055–1083, 2001.*

[44] *Jinwei Shen and Inderjit Chopra. Swashplateless helicopter rotor with trailing-edge flaps.* Journal of Aircraft*, 41(2), March-April 2004.*

[45] *Martin K. Sekula and Mattew L. Wilbur. Analysis of a multiflap control system for a swashplateless rotor.* Journal of the American Helicopter Society*, 57, 2012.*

[46] *Anand Saxena and Inderjit Chopra. Continued work on hover testing of a swashplateless rotor with compact brushless motor actuated flaps for primary control.* American Helicopter Society Annual Forum, Phenix, AZ*, May 21-23 2013.*

[47] *J-S. Kim, K. W. Wang, and E. C. Smith. Development of a resonant trailing-edge flap actuation system for helicopter rotor vibration control.* Smart Materials and Structures*, 16:2275–2285, 2007.*

[48] *Li Liu, Peretz P. Friedmann, Insung Kim, and Dennis S. Bernstein. Simultaneous vibration reduction and performance enhancement in rotorcraft using actively controlled flaps.* American Helicopter Society 62th Annual Forum, Phoenix, Arizona*, 9-11 May 2006.*

[49] *Yung H. Yu, Bernd Gmelin, Wolf Splettstoesser, Jean J. Philippe, Jean Prieur, and Thomas F. Brooks. Reduction of helicopter blade-vortex interaction noise by active rotor control technology.* Progress in Aerospace Sciences*, 33:647–687, 1997.*

[50] *Manish K. Singh, K. Dhanalakshmi, and S. K. Chakrabartty. Navier-stokes analysis of airfoils with gurney flap.* Journal of Aircraft*, 44(5), September-October 2007.*

[51] *Michael R. Thiel, George A. Lesieutre, Mark D. Maughmer, and Gary H. Koopmann. Actuation of an active gurney flap for rotorcraft applications.* 47th AIAA/ASME/ASCE/AHS/ASC Structures, Structural Dynamics, and Materials Conference, Newport, Rhode Island*, 1-4 May 2006.*

[52] *Kwanjung Yee, Wandon Joo, and Dong-Ho Lee. Aerodynamic performance analysis of a gurney flap for rotorcraft application.* Journal of Aircraft*, 44(3), May-June 2007.*

[53] *Mark D. Maughmer and Götz Bramesfeld. Experimental investigation of gurney flaps.* Journal of Aircraft*, 45(6), November-December 2008.*

[54] *J. J. Wang, Y. C. Li, and K.-S. Choi. Gurney flap-lift enhancement, mechanisms and applications.* Progress in Aerospace Sciences*, 44:22–47, 2008.*

[55] *Li Liu, Ashwani K. Padthe, and Peretz P. Friedmann. Computational study of microflaps with application to vibration reduction in helicopter rotors.* AIAA Journal*, 49(7), July 2011.*

[56] *Brian C. Kuo and Nesrin Sarigul-Klijn. Conceptual study of micro-tab device in airframe noise reduction: (i) 2d computation.* Aerospace Science and Technology*, 14:307–315, 2010.*

[57] *Ashwani K. Padthe and Peretz P. Friedmann. Simultaneous bvi noise and vibration reduction in rotorcraft using microflaps including the effect of actuator saturation.* American Helicopter Society 68th Annual Forum*, 2012.*

[58] *S. Lee, K. W. McAlister, and C. Tung. Characteristics of deformable leading edge for high performance rotor.* AIAA 11th Applied Aerodynamics Conference*, August 9-11 1993.*

[59] *P. B. Martin, K. W. McAlister, M. S. Chandrasekhara, and W. Geissler. Dynamic stall measurements and computations for a vr-12 airfoil with a variable droop leading edge.* American Helicopter Society 59th Annual Forum , Phoenix, Arizona*, May 6-8 2003.*

[60] *M. S Chandrasekhara. Compressible dynamic stall vorticity flux control using a dynamic camber airfoil.* Sadhana*, 32:93–102, February-April 2007.*

[61] *E. Breitbach and A. Büter. The main sources of helicopter vibration and noise emissions and adaptive concepts to reduce them.* Journal of Structural Control*, 3(1), June 1996.*

[62] *Farhan Gandhi, Mary Frecker, and Andrew Nissly. Design optimization of a controllable camber rotor airfoil.* AIAA Journal*, 46(1), January 2008.*

[63] *Alessandro Spandoni and Massimo Ruzzene. Numerical and experimental analysis of the static compliance of chiral truss-core airfoils.* Journal of Mechanics of Materials and Structures*, 2(5), 2007.*

[64] *Tianshu Liu, J. Montefort, W. Liou, and S. R. Pantula. Lift enhancement by static extended trailing edge.* Journal of Aircraft*, 44(6), November-December 2007.*

[65] *J. T. Pearson, R. M. Goodall, and I. Lyndon. Active control of helicopter vibration.* Computing and Control Engineering Journal*, 1994.*

[66] *Richard C. Cribbs, Peretz P. Friedmann, and Thiem Chiu. Coupled helicopter rotor/flexible fuselage aeroelastic model for control of structural response.* AIAA Journal*, 38(10), October 2000.*

[67] *Claudio Brillante, Marco Morandini, and Paolo Mantegazza. Characterization of beam stiffness matrix with embedded piezoelectric devices via generalized eigenvectors.* International Journal of Solids and Structures*, 59:37–45, 2015.*

[68] *B Bandyopadhyay T C Manjunath. Multivariable control of smart timoshenko beam structures using pof technique.* International Journal of Signal Processing*, 2006.*

[69] *Najeeb ur Rahman and M. Naushad Alam. Active vibration control of a piezoelectric beam using pid controller: Experimental study.* Latin American Journal of Solids and Structures*, 9:657–673, 2012.*

[70] *Sang Joon Shin and Carlos E.S. Censik. Helicopter vibration reduction in forward flight using blade integral twist actuation.* Journal of Mechanical Science and Technology*, 21(2), 2007.*

[71] *Gian Luca Ghiringhelli, Pierangelo Masarati, Marco Morandini, and Davide Muffo. Integrated aeroservoelastic analysis of induced strain rotor blades.* Mechanics of Advanced Materials and Structures*, 15:291–306, 2008.*

[72] *A. Benjeddou. Advances in piezoelectric finite element modeling of adaptive structural elements: a survey.* Computers and Structures*, 76:347–363, 2000.*

[73] *K. Srinivasa Rao, G. Srinivas, M. S. Prasad, Y. Srinivas, B. Shudheer, and A. Venkateswar Rao. Design and simulation of mems based piezoelectric shear actuated beam.* American Journal of Materials Science*, 2:179–184, 2012.*

[74] *Michael J. Carpenter. Using energy methods to derive beam finite elements incorporating piezoelectric materials.* Journal of Intelligent Material Systems and Structures*, 8, 1997.*

[75] *P. Sadilek R. Zemcik. Modal analysis of beam with piezoelectric sensors a actuators.* Applied and Computational Mechanics*, 1:381–386, 2007.*

[76] *A. Benjeddou, M. A. Trindade, and R. Ohayon. A unified beam finite element model for extension and shear piezoelectric actuation mechanisms.* Journal of Intelligent Material Systems and Structures*, 8:1012–1025, 1997.*

[77] *M Adnan Elshafei and Fuzy Alraiess. Modeling and analysis of smart piezoelectric beams using simple higher order shear deformation theory.* Smart Materials and Structures*, 22, 2013.*

[78] *Corrado Maurini, Joel Pouget, and Francesco dell'Isola. On a model of layered piezoelectric beams including transverse stress effect.* International Journal of Solids and Structures*, 20, 2004.*

[79] *Uttam Kumar Chakravarty. On the modeling of composite beam cross-sections.* Composites Part B: Engineering*, 42(4):982–991, June 2011.*

[80] *Vittorio Giavotto, Marco Borri, Paolo Mantegazza, Gian Luca Ghiringhelli, V. Carmaschi, G. C. Maffioli, and F. Mussi. Anisotropic beam theory and applications.* Computers & Structures*, 16:403–413, 1983.*

[81] *Dewey H. Hodges.* Nonlinear composite beam theory. *Number 213 in Progress in Astronautics and Aeronautics. American Institute of Aeronautics and Astronautics, 1801 Alexander Bell Drive, Suite 500, Reston, VA, 20191-4344, USA, 2006.*

[82] *Gian Luca Ghiringhelli, Pierangelo Masarati, and Paolo Mantegazza. Characterization of anisotropic non-homogeneous beam section with embedded piezo-electric materials.* Journal of Intelligent Material Systems and Structures*, 8(10):842–858, 1997.*

[83] *Carlos E. S. Censik and Miguel Ortega-Morales. Active beam cross-sectional modeling.* Journal of Intelligent Material Systems and Structures*, 12, 2001.*

[84] *Sitikantha Roy, Wenbin Yu, and Dong Han. An asymptotically correct classical model for smart beams.* International Journal of Solids and Structures*, 44:8424–8439, 2007.*

[85] Marco Morandini, Maria Chierichetti, and Paolo Mantegazza. Characteristic behavior of prismatic anisotropic beam via generalized eigenvectors. International Journal of Solids and Structures*, 47(10):1327–1337, May 2010.*

[86] Alexander Mielke. Hamiltonian and Lagrangian Flows on Center Manifolds with Applications to Elliptic Variational Problems*, volume 1489 of* Lecture Notes in Mathematics*. Springer Berlin / Heidelberg, 1991.*

[87] Zhong Wanxie, Xu Xinsheng, and Zhang Hongwu. Hamiltonian system and the saint venant problem in elasticity. Applied Mathematics and Mechanics*, 17(9):827–836, 1996.*

[88] Weian Yao, Wanxie Zhong, and Chee Wah Lim. Symplectic Elasticity*. WORLD SCIENTIFIC, February 2009.*

[89] Olivier A. Bauchau and Shilei Han. Three-dimensional beam theory for flexible multibody dynamics. Journal of Computational and Nonlinear Dynamics*, in press.*

[90] A.Y.T. Leung, J.J. Zheng, C.W. Lim, Xiaochun Zhang, Xin-Sheng Xu, and Qian Gu. A new symplectic approach for piezoelectric cantilever composite plates. Computers & Structures*, 86(19–20):1865–1874, October 2008.*

[91] Osama J. Aldraihem and Ahmed A Khdeir. Smart beams with extension and thickness-shear piezoelectric actuators. Smart Materials and Structures*, 9, 2000.*

[92] Gian Luca Ghiringhelli, Pierangelo Masarati, Marco Morandini, and Davide Muffo. Integrated aeroservoelastic analysis of induced strain rotor blades. Mechanics of Advanced Materials and Structures*, 15:291–306, 2008.*

[93] J.S. Kumar, N. Ganesan, and S. Swarnamani. Active control of beam with magnetostrictive layer. Computers and Structures*, 81(13):1375–1382, 2003.*

[94] T. Zhang, C. Jiang, H. Zhang, and H. Xu. Giant magnetostrictive actuators for active vibration control. Smart Materials and Structures*, 13(3):473–477, 2004.*

[95] Giuseppe Davi, Alberto Milazzo, and Calogero Orlando. Magneto-electro-elastic bimorph analysis by the boundary element method. Mechanics of Advanced Materials and Structures*, 15:220–227, 2008.*

[96] A. Milazzo, C. Orlando, and A. Alaimo. An analytical solution for the magneto-electro-elastic bimorph beam forced vibrations problem. Smart Materials and Structures*, 18, 2009.*

[97] Giuseppe Davi and Alberto Milazzo. A regular variational boundary model for free vibrations of magneto-electro-elastic structures. Engineering Analysis with Boundary Elements*, 35:303–312, 2011.*

[98] Alberto Milazzo. A one-dimensional model for dynamic analysis of generally layered magneto-electro-elastic beams. Journal of Sound and Vibration*, 332:465–483, 2013.*

[99] *Oliver Dieterich, Joachim Götz, Binh DangVu, Henk Haverdings, Pierangelo Masarati, Marilena Pavel, Michael Jump, and Genaretti Massimiliano. Adverse rotorcraft-pilot coupling: Recent research activities in europe.* 34th European Rotorcraft Forum (ERF)*, September 2008.*

[100] *P. Masarati, M. Morandini, and P. Mantegazza. An efficient formulation for general-purpose multibody/multiphysics analysis.* ASME J. Comput. Nonlinear Dyn.*, 2013.*

[101] *https://www.mbdyn.org.*

[102] *Gian Luca Ghiringhelli, Pierangelo Masarati, and Paolo Mantegazza. Multibody implementation of finite volume c0 beams.* AIAA Journal*, 38(1), 2000.*

[103] *G. L. Ghiringhelli, P. Masarati, and P. Mantegazza. Characterisation of anisotropic, non-homogeneous beam sections with embedded piezo-electric materials.* Journal of Intelligent Material Systems and Structures*, 8:842–858, 1997.*

[104] *Marco Morandini, Maria Chierichetti, and Paolo Mantegazza. Characteristic behavior of prismatic anisotropic beam via generalized eigenvectors.* International Journal of Solids and Structures*, 47:1327–1337, 2010.*

[105] *Claudio Brillante, Marco Morandini, and Paolo Mantegazza. Characterization of beam stiffness matrix with embedded piezoelectric devices via generalized eigenvectors.* International Journal of Solids and Structures*, 59:37–45, 2015.*

[106] *David E. Fogarty, Mattew L. Wilbur, Martin K. Sekula, and D. Douglas Boyd Jr. Prediction of bvi noise for an active twist rotor using a loosely coupled cfd/csd method and comparison to experimental data.* American Helicopter Society 68th Annual Forum, Fort Worth, Texas*, May 1-3 2012.*

[107] *Mark Potsdam, Mark V. Fulton, and Arsenio Dimanlig. Multidisciplinary cfd/csd analysis of the smart active flap rotor.* American Helicopter Society 66th Annual Forum, Phoenix, Arizona*, May 11-13 2010.*

[108] *Jeremy Bain, Mark Potsdam, Lakshmi Sankar, and Kenneth S. Brentner. Aeromechanic and aeroacoustic predictions of the boeing smart rotor using coupled cfd/csd analysis.* American Helicopter Society 66th Annual Forum, Phoenix, Arizona*, May 11-13 2010.*

[109] *C. Sheng, Q. Zhao, N. Rajmohan, L. Sankar, J. O. Bridgeman, and J. C. Narramore. An unstructured hybrid cfd approach for computing rotor wake flows.* 49th AIAA Aerospace Sciences Meeting including the New Horizons Forum and Aerospace Exposition, Orlando, Florida*, January 2011.*

[110] *Shi Yongjie, Zhao Qijun, Fan Feng, and Xu Guohua. A new single-blade based hybrid cfd method for hovering and forward-flight rotor computation.* Chinese Journal of Aeronautics*, 24:127–135, 2011.*

[111] *Yang Z., Sankar L. N., Smith M., and Bauchau O. Recent improvements to a hybrid method for rotors in forward flight.* Journal of Aircraft*, 39(5):804–812, 2002.*

[112] Nischint Rajmohan, Lakshmi Sankar, Oliver Bauchau, Bruce Charles, Stephen M. Makinen, and T. Alan Egolf. Application of hybrid methodology to rotors in steady and manuveuring flight. American Helicopter Society 64th Annual Forum, Montreal, Canada*, April 29 - May 1, 2008.*

[113] M. Biava, A. Pisoni, A. Saporiti, and L. Vigevano. Efficient rotor aerodynamics predictions with an euler method. 29th European Rotorcraft Forum, Friedrichshafen, Germany*, September 2003.*

[114] M. Amiraux. Numerical simulation and validation of helicopter blade-vortex interaction using coupled cfd/csd and three levels of aerodynamic modeling. PhD Thesis, University of Maryland, Department of Aerospace Engineering*, 2014.*

[115] Byung Young Min, Lakshmi Sankar, and Oliver A. Bauchau. A cfd-csd coupled-analysis of hart-ii rotor vibration reduction using gurney flaps. American Helicopter Society 66th Annual Forum, Phoenix, Arizona*, May 11-13 2010.*

[116] Shreyas Ananthan, James D. Baeder, and Jayanarayanan Sitaraman. Hybrid unsteady simulation of helicopters: Hush. 26th AIAA Applied Aerodynamics Conference, Honolulu, Hawaii*, August 18-21 2008.*

[117] Ashwani K. Padthe, Li Liu, and Peretz P. Friedmann. A comprehensive study of active microflaps for vibration reduction in rotorcraft. American Helicopter Society 66th Annual Forum, Phoenix, Arizona*, May 11-13 2010.*

[118] Li Liu, Ashwani K. Padthe, Peretz P. Friedmann, Eliot Quon, and Marilyn J. Smith. Unsteady aerodynamics of an airfoil/flap combination on a helicopter rotor using computational fluid dynamics and approximate methods. American Helicopter Society 65th Annual Forum, Grapevine, TX*, May 27-29 2009.*

[119] https://bitbucket.org/MarcoMorandini/st/downloads.

[120] A. Parrinello and P. Mantegazza. Independent two-fields solution for full-potential unsteady transonic flows. AIAA Journal*, 48:1391–1402, 2010.*

[121] A. Parrinello and P. Mantegazza. Improvements and extensions to a full-potential formulation based on independent fields. AIAA Journal*, 50:571–580, 2012.*

[122] A. Parrinello, M. Morandini, and P. Mantegazza. Automatic embedding of potential flow wake surfaces in generic monolithic unstructured meshes. Journal of Aircraft*, 50:1179–1188, 2013.*

[123] Chad L. File. Optimizaion of induced-power from dynamic inflow theory with realistic constraints. PhD Thesis, Department of Mechanical Engineering and Materials Science, Washington University in St. Louis*, May 2013.*

[124] http://algoholic.eu/matpy/.

[125] Giuseppe Quaranta, Pierangelo Masarati, and paolo Mantegazza. A conservative mesh-free approach for fluid-structure interface problems. International Conference for Coupled Problems in Science and Engineering. Santorini, Greece*, May 23-29, 2005.*

[126] M. Biava. RANS computations of rotor/fuselage unsteady interactional aerodynamics. *PhD thesis, Dipartimento di Ingegneria Aerospaziale, Politecnico di Milano, 2007.*

[127] M. Biava, W. Khier, and L. Vigevano. CFD prediction of air flow past a full helicopter configuration. Aerospace Science and Technology*, 19:3–18, 2012.*

[128] G. Chesshire and W. D. Henshaw. Composite overlapping meshes for the solution of partial differential equations. Journal of Computational Physics*, 90:1–64, 1990.*

[129] P.L. Roe. Approximate Riemann Solvers, Parameter Vectors and Difference Schemes. Journal of Computational Physics*, 43:357–372, 1981.*

[130] A. Jameson. Time dependent calculations using multigrid with applications to unsteady flows past airfoils and wings. In 10^{th} AIAA Computational Fluid Dynamics Conference, Honolulu, HI. AIAA 91-1596*, 1991.*

[131] Jeong Hwan Sa, Jee Woong Kim, Soo Hyung Park, Young Hyum You, Jae Sang Park, Sung Nam Jung, and Yung Hoon Yu. Prediction of hart ii airloads considering fuselage effect and elastic blade deformation. Heli Japan, Sitama, Japan*, November 1-3, 2010.*

[132] Raymond L. Bisplinghoff, Holt Ashley, and Robert L. Halfman. Aeroelasticity. *Dover Publications, 1955.*

[133] Morten Hartvig Hansen, Mac Gaunaa, and Helge Aagaard Madsen. A beddoes-leishman type dynamic stall model in state-dpace and indicial formulations. Riso National Laboratory, Roskilde, Denmark*, June 2004.*

[134] L. J. Vermeer. A review of wind turbine wake research at tudelft. American Institute of Aeronautics and Astronautics, Inc.and The American Society of Mechanical Engineers*, 2001.*

[135] Wayne Johnson. Influence of wake models on calculated tiltrotor aerodynamics. American Helicopter Society Aerodynamics, Acoustics, and Test and Evaluation Technical Specialists Meeting, San Francisco, CA*, January 23-25, 2002.*

[136] Joon W. Lim, Yung H. Yu, and Wayne Johnson. Calculation of rotor blade-vortex interaction airloads using a multiple-trailer free wake model. Journal of Aircraft*, 40(6), November-December 2003.*

[137] Wayne Johnson. A general free wake geometry calculation for wings and rotors. American Helicopter Society 51st Annual Forum, Fort Worth, Texas*, 9-11 May 1995.*

[138] J. Gordon Leishman, Mahendra J. Bhagwat, and Shreyas Ananthan. Free-vortex wake predictions of the vortex ring state for single-rotor and multi-rotor configurations. 58th Annual Forum and echnology Display of the American Helicopter Society International, Montral, Canada*, June 11-13, 2002.*

[139] A. Bagai and J.G. Leishman. Flow visualization of compressible vortex structures using density gradient techniques. Experiments in Fluids*, 15:431–442, 1993.*

[140] R. Vaghi. Studio Numerico del Controllo Ottimo di un Rotore Articolato di Elicottero con Applicazione alle Instabilitá di Flappeggio e Ritardo. *Master Thesis, Politecnico di Milano, Dipartimento di Ingegneria Aerospaziale, 1991.*

[141] Paolo Arcara, Sergio Bittanti, and Marco Lovera. Periodic control of helicopter rotors for attenuation of vibrations in forward flight. IEEE Transaction on Control Systems Technology*, 8(6), 2000.*

[142] Sergio Bittanti and Francesco A. Cuzzola. Periodic active control of vibrations in helicopters: a gain-scheduled multi-objective approach. Control Engineering Practice*, 10:1043–1057, 2002.*

[143] Fatma Demet Ulker. A New Framework For Helicopter Vibration Suppression; Time-Periodic System Identification and Controller Design. *PhD Thesis, Ottawa-Carleton Institute for Mechanical and Aerospace Engineering, April, 2011.*

[144] Claudio Brillante, Marco Morandini, and Paolo Mantegazza. H_2 periodic control on active twist rotor for vibration reduction. AHS 70th Annual Forum and Technology Display, Montreal, Canada*, May 20-22, 2014.*

[145] Claudio Brillante, Marco Morandini, and Paolo Mantegazza. Periodic output feedback control for helicopter vibration reduction. International Forum on Aeroelasticity and Structural Dynamics, Saint Petersburg, Russia*, June 28- July 2, 2015.*

[146] Michel Verhaegen and Xiaode Yu. A class of subspace model identification algorithms to identify periodically and arbitrarily time-varying systems. Automatica*, 31:201–216, 1995.*

[147] Sergio Bittanti and Patrizio Colaneri. Periodic Systems Filtering and Control*. Springer, 2009.*

[148] J. J. Hench and A. J. Laub. Numerical solution of the discrete-time periodic riccati equation. IEEE Transaction on Automatic Control*, 39(6), 1994.*

[149] A. Varga. On solving periodic riccati equations. Numerical Linear Algebra with Applications*, 2008.*

[150] Kemin Zhou and John C. Doyle. Essentials of Robust Control*. Prentice Hall, 1997.*

[151] A. Varga and S. Pieters. A coputational approach for optimal periodic output feedback control. IEEE International Symposium on Computer Aided Control System Design - CACSD*, 1996.*

[152] A. Varga. Periodic lyapounov equations: Some applications and new algorithms. international Journal of Control*, 67:69–88, 1997.*

[153] Martin Schulz and Johannes Riemenschneider. Investigation of active twist rotor for blade deicing. American Helicopter Society 69th Annual Forum, Phoenix, Arizona, USA*, May 21-23, 2013.*

[154] David Amsallem. Interpolation on manifolds of cfd-based fluid and finite element-based structural reduced-order models for on-line aeroelastic predictions. PhD Thesis, Stanford University, Department of Aeronautics and Astronautics*, 2010.*

[155] Jan De Caigny, Juan F. Camino, and Jan Swevers. Interpolation-based modeling of mimo lpv systems. IEEE Transactions on Control Systems Technology*, 19(1), 2011.*

[156] J. Ko, T. W.. Strganac, and A. J. Kurdila. Adaptive feedback linearization for the control of a typical wing section with structural nonlinearity. Nonlinear Dynamics*, 18(3):289–301, 1999.*

[157] C.-L. Chen, C.-W. Chang, , and H.-T. Yau. Terminal sliding mode control for aeroelastic systems. Nonlinear Dynamics*, 70(3):2015–2026, 1999.*

[158] K. W. Lee and S. N. Singh. Immersion- and invariancebased adaptive control of a nonlinear aeroelastic system. Journal of Guidance, Control and Dynamics*, 32(4):1100–1110, 2009.*

[159] R.C. Scott and L.E. Pado. Active Control of Wind Tunnel Model Aeroelastic Response Using Neural Networks. Journal of Guidance, Control and Dynamics*, 23:1100–1108, 2001.*

[160] F. Bernelli-Zazzera, P. Mantegazza, G. Mazzoni, and M. Rendina. Active Flutter Suppression Using Recurrent Neural Networks. Journal of Guidance, Control and Dynamics*, 23:1030–1037, 2000.*

[161] M. Mattaboni, G. Quaranta, and P. Mantegazza. Active flutter suppression for a three surface transport aircraft by recurrent neural networks. In 48th AIAA/ASME/ASCE/AHS/ASC Structures, Structural Dynamics and Materials Conference, Honolulu, HI*, 2007.*

[162] Li Liu, Peretz P. Friedmann, Insung Kim, and Dennis S. Bernstein. Simultaneous vibration reduction and performance enhancement in rotorcraft using actively controlled flaps. American Helicopter Society 62nd Annual Forum, Pheonix, AZ*, May 9-11 2006.*

[163] Matthias Althof, Mayuresh J. Patil, and Johannes P. Traugott. Nonlinear modeling and control design of active helicopter blades. Journal of the American Helicopter Society*, 57, 2012.*

[164] T. John Koo, Yi Ma, and S. Shankar Sastry. Nonlinear control of a helicopter based unmanned aerial vehicle model. 2001.

[165] Bing Zhu. Nonlinear adaptive neural network control for a model-scaled unmanned helicopter. Nonlinear Dynamics*, 78:1695–1708, 2014.*

[166] Jose I. Canelon, Heidar A. Malki, Stephen A. Jacklin, and Leang S. Shieh. An adaptive neural network model for vibration control in a blackhawk helicopter. Journal of the American Helicopter Society*, 50(4):349–353, 2005.*

[167] Michael G. Spencer, Robert M. Sanner, and Inderjit Chopra. Closed-loop neurocontoller tests on piezoactuated smart rotor blades in hover. AIAA Journal*, 40(8), August 2002.*

[168] S. Haykin. Neural Networks and Learning Machines*. Prentice Hall, Upper Saddle River, NJ; 3 edition, 2008.*

[169] R. J. Williams and D. Zipser. A learning algorithm for continually running fully recurrent neural networks. Neural Comput.*, 1(2):270–280, June 1989.*

[170] S. Haykin. Neural Networks and Learning Machines: A Comprehensive Foundation. *Prentice Hall, 2008.*

[171] Ashwani K. Padthe, Li Liu, and Peretz P. Friedmann. A comprehensive study of active microflaps for vibration reduction in rotorcraft. American Helicopter Society 66th Annual Forum, Phoenix, Arizona*, 11-13 May 2010.*

[172] Alessandro Anobile and Giovanni Bernardini. Synthesis of rotor BVI noise active controller through efficient aerodynamics/aeroacoustics solver. AIAA Aviation, 20th AIAA/CEAS Aeroacustics Conference, Alanta, GA*, 16-20 June 2014.*

[173] Frank H. Fan and Steven R. Hall. An H_∞ technique for improved higher harmonic control. American Helicopter Society 68th Annual Forum, Fort Worth, Texas*, 1-3 May 2012.*

[174] Roberto Mura and Marco Lovera. Baseline vibration attenuation in helicopters: robust MIMO-HHC control. Proceedings of the 19th World Congress. The International Federation of Automatic Control, Cape Town, South Africa*, August 24-29 2014.*

[175] Ashwani K. Padthe, Peretz P. Friedmann, and Dennis S. Bernstein. Actuator saturation in individual blade control of rotorcraft. Proceedings of the 40th European Rotorcraft Forum, Southampton, UK*, April 22-26 2012.*

[176] Beatrice Roget and Inderjit Chopra. Closed-loop test of a rotor with individually controlled trailing-edge flaps for vibration reduction. American Helicopter Society 61th Annual Forum, Grapevine, TX*, June 1-3 2005.*

[177] R. Morales, M. C. Turner, P. Court, and C. Hutchin. Actuator constraints handling in higher harmonic control algorithms for vibration reduction. Proceedings of the 40th European Rotorcraft Forum, Southampton, UK*, September 2-5 2014.*

[178] D. Patt, L. Liu, J. Chandrasekar, D. S. Bernstein, and P. P. Friedmann. Higher-harmonic-control algorithm for helicopter vibration reduction revisited. Journal of Guidance, Control and Dynamics*, 28(5), September-October 2005.*

[179] Stephen J. Wright Jeorge Nocedal. Numerical Optimization*. Springer, 1999.*

[180] Thomas Reslow Kruth. Interior-point algorithms for quadratic programming. Master Thesis, Technical University of Denmark*, 2008.*

[181] Philip Küfmann and Claudio Brillante. Implementation and test of a semi-closed loop hhc-algorithm with the DLR's multiple swashplate system. Proceedings of the 41th European Rotorcraft Forum, Munich, Germany*, September 1-4 2015.*

[182] Mayuresh J. Patil and Robert L. Clark. Aeroelastic control using multiple control surfaces. 43rd AIAA/ASME/ASCE/AHS/ASC Structures, Structural Dynamics, and Materials Control, Denver, Colorado*, 22-25 April 2002.*

[183] Emil V. Ardelean, Mark A. McEver, Daniel G. Cole, and Robert L. Clark. Active flutter control with v-stack piezoelectric flap actuator. Journal of Aircraft*, 43(2), March-April 2006.*

[184] Y. C. Fung. An Introduction to the Theory of Aeroelasticity. *Dover Publications, 1993.*

[185] Rainer Bartels, Philip Küfmann, and Christoph Keßler. Novel concept for realizing individual blade control (ibc) for helicopters. 36th European Rotorcraft Forum, Paris, France*, 7-9 September, 2010.*

[186] P. Küfmann, R. Bartels, C. Keßler, and B.G. van der Wall. On the design and development of a multiple-swashplate control system for the realization of individual blade control (IBC) for helicopters. American Helicopter Society 67th Annual Forum, Virginia Beach, VA*, 3-5 May, 2011.*

[187] Philip Küfmann, Rainer Bartels, and Oliver Schneider. DLR's multiple swashplate control system: Operation and preliminary testing. 37th European Rotorcraft Forum, Amsterdam, Netherlands*, September 4-7, 2012.*

[188] W. Johnson. Helicopter Theory. *Princeton university Press, New Jersey, 1980.*